

NAIC-ID(RS)T-0502-96

# NATIONAL AIR INTELLIGENCE CENTER



SELECTED ARTICLES

EDUCATIONAL QUALITY INSPECTED 2



19970206 089

Approved for public release:  
distribution unlimited



**HUMAN TRANSLATION**

NAIC-ID(RS)T-0502-96      6 January 1997

MICROFICHE NR:

SELECTED ARTICLES

English pages: 134

Source: Daodan Yu Hangtian Yunzai Jishu; pp. 1-8; 18-63;  
74-80.

Country of origin: China

Translated by: Leo Kanner Associates  
F33657-88-D-2188

Requester: NAIC/TABS/Jeffrey Gossel

Approved for public release: distribution unlimited.

THIS TRANSLATION IS A RENDITION OF THE ORIGINAL  
FOREIGN TEXT WITHOUT ANY ANALYTICAL OR EDITO-  
RIAL COMMENT STATEMENTS OR THEORIES ADVO-  
CATED OR IMPLIED ARE THOSE OF THE SOURCE AND  
DO NOT NECESSARILY REFLECT THE POSITION OR  
OPINION OF THE NATIONAL AIR INTELLIGENCE CENTER.

PREPARED BY:

TRANSLATION SERVICES  
NATIONAL AIR INTELLIGENCE CENTER  
WPAFB, OHIO

## TABLE OF CONTENTS

GRAPHICS DISCLAIMER .....	ii
REENTRY FLIGHT USING NEGATIVE LIFT OF SPACE VEHICLE, by Nan Ying, Wang Zhigang, Chen Shilu .....	1
FOUR PREVENTIVE MEASURES AND GROUNDING OF LAUNCH VEHICLES, by Gao Zhi .....	17
PROGRAM DESIGN OF DEFORMATION OF BALL BEARINGS UNDER PRELOADS, by Zhu Jianghong .....	43
PLATFORM GIMBAL DESIGN AND MACHINING TECHNOLOGY, by Liu Yiwei, Chen Xiaozhong .....	70
DESIGN STUDY OF RADAR ABSORBENT MATERIAL COMPOSITES, by Zhang Lizhong .....	86
BPSK CARRIER AND BIT SYNCHRONIZATION TECHNOLOGY IN PRESENCE OF DYNAMIC DOPPLER, Sun Dongzhi .....	101
NEWS BRIEF: PROTON M ROCKET WILL BE BROUGHT INTO COMMERCIAL LAUNCH MARKET .....	117

**GRAPHICS DISCLAIMER**

**All figures, graphics, tables, equations, etc. merged into this  
translation were extracted from the best quality copy available.**

REENTRY FLIGHT USING NEGATIVE LIFT OF SPACE VEHICLE

Nan Ying, Wang Zhigang, and Chen Shilu

Aerospace Engineering College  
Northwestern Polytechnical University

**ABSTRACT:** The corridor and trajectories of space vehicles during reentry flight using negative lift are studied. Numerical results are obtained for the corridors and trajectories using negative and positive lift, respectively. The following conclusions are obtained: in the case of a larger lift-drag ratio, the first one-third reentry corridor using negative lift is wider than that using positive lift; the total mass cost (TMC) by negative lift is smaller than that for positive lift, where TMC is the total mass of fuel consumed for the vehicle to deorbit from the mission orbit and the mass of the thermal protection system of the vehicle, in the case of a smaller lift-drag ratio. The two kinds of reentry trajectories produced by positive lift and negative lift are approximately the same. Therefore, the concept of return flight using negative lift is superior to that using positive lift.

**KEY WORDS:** space vehicle, reentry trajectory, optimal control.

## 1. Introduction

The basic principle in designing the optimal return trajectories of launch vehicles is to obtain a minimum return cost. Basically, the return cost is the sum of the mass of propellant consumed for the vehicle to deorbit from the mission orbit and the mass of the thermal protection system (TPS) of the vehicle.

During a return reentry flight of a space lift vehicle (such as a spacecraft orbiter), a large positive attack angle (in order to generate positive lift coefficients and drag coefficients) is generally adopted to realize a normal return flight[1]. Since London proposed using a negative lift to realize an aerodynamically assisted orbital transfer of space vehicles in 1962[2], tremendous achievements were attained in the study of aerodynamic orbital transfer using negative lift.

The term "negative lift" as utilized in aerodynamic orbital transfers in some foreign countries refers to an aerodynamically lift force directed at geocenter, while positive lift signifies that this force is directed away from geocenter. Negative lift is obtained by using a positive attack angle and a roll angle larger than  $90^{\circ}$ . Such a concept of "negative lift" differs from its traditional definition (the lift force is obtained by using a negative attack angle). Reentry using negative lift signifies that negative lift is used during the period of time when a space vehicle has just entered the atmosphere, and then positive lift is employed instead for the remainder of the reentry flight after the vehicle is captured by the atmosphere; reentry using positive lift means that positive lift is used during the whole flight of the space vehicle from reentry point to landing point. It is unfortunate, however, that almost all available domestic and foreign references unanimously describe return reentry flight

using positive lift[1, 3].

Given the initial parameters of the reentry point, A. Miele, X. Vinh, K. P. Zondervan, G. Ley Brauer, Garcia, and Fowler et al. accomplished much in optimizing reentry trajectories, in which more than 10 indexes were involved[3]. Yet few of these references studied the optimal reentry trajectories in which the sum of the mass of propellant consumed at the deorbiting point and the TPS mass was minimized.

This paper studies optimal trajectories of space vehicles in realizing return reentry using negative lift under different lift-to-drag ratios, in which the performance index is the minimum return cost. Based on a numerical simulation of reentry flight using negative and positive lift under different lift-to-drag ratios as well as a comparative analysis of the simulation results, this paper reached some useful conclusions.

## 2. Methods of Optimizing Return Trajectories of Space Vehicles

No matter whether positive or negative lift is used in reentry flight, the methods of optimizing the return trajectories of space vehicles are much the same. The only difference lies in the evaluation range of the roll angle as a control variable.

The optimization of the return trajectories of space vehicles involves reentry corridor, estimation of the mass of TPS, optimization of reentry trajectories, etc.

### 2.1. Reentry Corridor

The definition of reentry corridor[4]: The upper boundary of reentry corridor refers to the most gentle trajectory of the space vehicle under various constraints. The first one-third of the reentry corridor is exclusively determined by the initial

parameters of the reentry point, while its last two-thirds is determined by the maximum lift-to-drag ratio of the space vehicle. The lower boundary of the reentry corridor is the steepest flight trajectory of the space vehicle under various constraints, which is determined by the maximum temperature, overload and dynamic pressure.

By using the method of computing reentry corridor boundaries in reference 4, the upper and lower boundaries of reentry corridor under positive lift and negative lift are calculated, respectively, using the United States Space Shuttles as examples. The calculations are shown in Figs. 1-4, where the imaginary and solid lines, respectively, are reentry using positive lift and reentry using negative lift.

## 2.2. Approximation Computational Method for TPS Mass of Space Vehicles

This paper discusses only the approximation computational method of TPS mass of space vehicles with complex shapes (such as the spacecraft orbiter). In reference 5, the TPS of the spacecraft orbiter is divided into 22 segments. In this case, the total mass of the TPS is

$$W_{\text{TPS}} = W_{\text{RSI}} + W_M \quad (1)$$

where subscripts RSI and M are, respectively, the reusable heat-insulation material and metal (or glass) material.

$$W_{\text{RSI}} = \sum_{i=1}^n A_i (\bar{Q}_i) + A_{\text{un}} f(\bar{Q}_{\text{un}}) \quad (2)$$

$$W_M = \sum_{i=1}^n A_i [L_i(T_{\text{max}}) + f(\bar{Q}_i)] \quad (3)$$

where  $A_i$  and  $\bar{Q}_i$ , respectively, are the area and thermal load of the i-th segment.  $f(\bar{Q}_i)$  and  $L_i(T_{\text{max}})$ , respectively, are the mass of TPS unit area when the i-th segment is reusable heat-insulation material and metal;  $T_{\text{max}}$  is the maximum temperature in temperature history. Reference 6 presents  $f(\bar{Q}_i)$  and  $L_i(T_{\text{max}})$  curves, based on which reference 7 proposes the approximate accommodation formulas.

$_{_1}$  and  $T$  can be calculated from the following formulas:

$$\bar{Q}_i = \int_{t_0}^{t_f} k \frac{\dot{q}}{\dot{q}_s} \dot{q}_s dt \quad (4)$$

$$\dot{q} / \dot{q}_s = m_i a + b_i \quad (i = 1, 2, \dots, 22) \quad (5)$$

$$\dot{q}_s = \frac{C}{\sqrt{R}} \sqrt{\frac{\rho}{\rho_0}} \left( \frac{V}{V_c} \right)^{3.15}, \quad \rho_0 = 1.25, \quad V_c = 7800 \text{ m/s} \quad (6)$$

$$T = \dot{q}^{\frac{1}{4}} / (c\sigma) \quad (7)$$

where  $k_i = k(\rho, V, \dot{q}_s)$  is the effective factor of Reynolds number.  $\rho$ ,  $V$ ,  $\alpha$  and  $\dot{q}_s$ , respectively, are atmospheric density, flight speed, attack angle and the aerodynamically heating rate of the nose cone stagnation point zone.  $C, m_i, b_i, \epsilon, \sigma$  are all constants, which are given in reference 7.  $t_0$  and  $t_f$  are the starting point and terminating time of reentry flight;  $R$  is radius of the nose cone stagnation point zone.

### 2.3. Method of Optimizing Reentry Trajectories of Space Vehicles[6]

Let the kinematic differential equation of the space vehicle be

$$\dot{X} = f(X, U, t) \quad (8)$$

where  $X = \{V, \gamma, \psi, h, \theta, \phi\}$ ; the components of  $X$ , respectively, are: flight velocity, trajectory dip, drift angle, flight altitude, longitude and latitude. The function of  $f$  is given in reference 7. For spacecraft,  $U = \{\alpha, \sigma\}$ ,  $\sigma$  is roll angle; for spaceship,  $U = \{\sigma\}$ .

$$X(t_0) = X_0, \quad U \in \Omega \quad (9)$$

where  $X_0$  is the terminal state in the transitional period of deorbiting, i.e. the initial parameters of reentry point;  $\Omega$  is bounded closure. The terminal constraint is

$$M[X(t_f), t_f] = 0 \quad (10)$$

where  $M$  is function of  $q$ -dimensional vector. The performance index of optimal reentry trajectory is to minimize

$$J_1 = W_{T_{PS}} \quad (11)$$

To minimize  $J$ , it is necessary to obtain optimal permitted control  $U^*(t)$ . The following differential coupled equations can be derived from the principle of the minimum:

$$\dot{X} = f(X, U, t) \\ U = \arg \sup H, H = \lambda^T f \quad U \in \Omega \quad (12)$$

$$\lambda = -\frac{\partial H}{\partial X} \quad (13)$$

$$\lambda(t_f) = \frac{\partial W_{TPS}}{\partial X} \quad (14)$$

where  $\lambda$  is the six-dimensional auxiliary variable.

The boundary values of the two points can be solved using the conjugate gradient method. The concrete steps of solution are shown in references 6 and 7.

#### 2.4. Method of Optimizing Return Trajectories of Space Vehicles

The performance index of the optimal return trajectories of space vehicles is to minimize

$$J = W_{TPS} + m_{\infty} \quad (15)$$

where  $m_{\infty}$  is the mass of retro fuel consumed at the deorbiting point.

$$m_{\infty} = \int_{t_0}^{t_{01}} |\dot{m}_{\infty}| dt \quad (16)$$

where  $\dot{m}_{\infty}$  is mass flow rate of the retro-engines;  $t_{00}$  and  $t_{01}$ , respectively, are the starting time and terminating time of retro-engine operations.

In this paper, several groups of  $m_{\infty}$ ,  $\min(W_{TPS})$  are calculated for plotting the  $W_{TPS}$ - $m_{\infty}$  curves, which are used to solve the minimum value of  $J$ .

#### 3. Numerical Simulation and Analysis of Simulation Results

##### 3.1 Computational Conditions

The numerical simulation conditions for reentry using positive and for reentry using negative lift are fundamentally the same except for the evaluation range of the control variables. The thrust of the retro-engines is 9806.6N; the mass

flow rate is  $m_{00} = -3.22 \text{ kg/s}_0$ .

### 3.1.1. Conditions of Spacecraft

Its lift and drag coefficients, respectively, are

$$\begin{aligned} C_L &= C_{L0} + C_{L1}\alpha \\ C_D &= C_{D0} + C_{D1}\alpha + C_{D2}\alpha^2 \end{aligned} \quad (17)$$

(18)

where  $C_{L0} = -2.0704 \times 10^{-1}$ ,  $C_{L1} = 2.9224 \times 10^{-2}$ ,  $C_{D0} = 7.854 \times 10^{-2}$

$C_{D1} = 6.159 \times 10^{-3}$ ,  $C_{D2} = 6.2141 \times 10^{-4}$ .

The reference area  $S = 95 \text{ m}^2$ ; the mass of the space vehicle  $M(t_{00}) = 22000 \text{ kg}$ , while the starting and terminating constraints are as follows:  $X(t_{00}) = [7555 \text{ m/s}, 0^\circ, 0^\circ, 600 \text{ km}, 0, 0]$

$X(t_f) = [760 \text{ m/s}, -5^\circ, \text{Freedom}, 25 \text{ km}, \text{Freedom}, \text{Freedom}]$

In reentry using positive lift, the bounded closure  $U$  is

$$20^\circ \leq \alpha \leq 40^\circ \quad -50^\circ \leq \sigma \leq 50^\circ$$

In reentry using negative lift, the bounded closure  $U$  is

$$20^\circ \leq \alpha \leq 42^\circ \quad 0^\circ \leq \sigma \leq 180^\circ$$

### 3.1.2. Conditions of Spaceship

The aerodynamic parameters are

$$\frac{C_n S}{m} = 0.0017; \quad \frac{L}{D} = 0.35$$

The end point conditions are

$X(t_{00}) = [7500 \text{ m/s}, 0^\circ, 0^\circ, 600 \text{ km}, 0^\circ, 0^\circ]$

$X(t_f) = [211 \text{ m/s}, -65^\circ, \text{Freedom}, 10 \text{ km}, \text{Freedom}, \text{Freedom}]$

The constraint of control volume  $\sigma$  is

$0^\circ < \sigma < 180^\circ$  (in negative lift)

$-50^\circ < \sigma < 50^\circ$  (in positive lift)

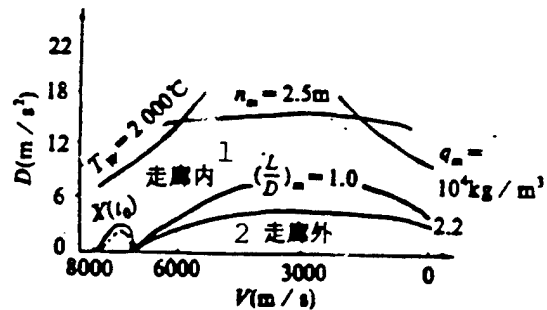


Fig. 1. Reentry corridor of spacecraft

KEY: (1) inside corridor  
(2) outside corridor

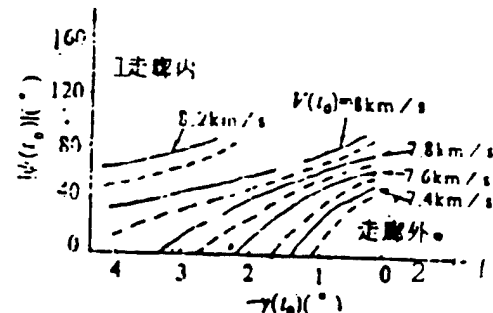


Fig. 2. Effect of velocity of reentry point on width of reentry corridor

KEY: (1) inside corridor  
(2) outside corridor

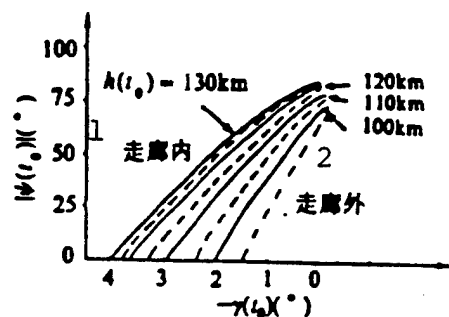


Fig. 3 Effect of altitude of reentry point on width of reentry corridor

KEY: (1) inside corridor  
(2) outside corridor

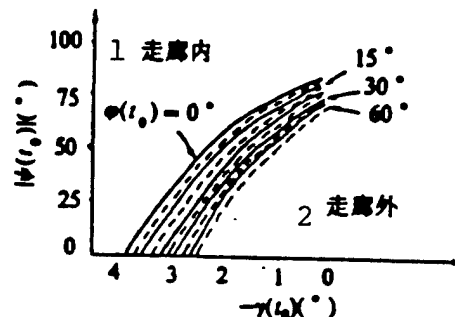


Fig. 4. Effect of latitude of reentry point on width of reentry corridor

KEY: (1) inside corridor  
(2) outside corridor

### 3.2. Calculations and Their Comparative Analysis

#### 3.2.1 Reentry Corridor

Fig. 1-4 suggest that the first one-third of the reentry corridor using negative lift is much wider than the one using positive lift. This is because in the initial period of reentry flight, the space vehicle is affected by aerodynamic force, G force, centrifugal force, gravitational force, and pulling (acceleration) force. During a reentry flight using positive lift, the aerodynamic force acts upward (away from geocenter), under which the space vehicle can possibly be "thrown out" of the

atmosphere due to the aerodynamic force, and the width of corridor is narrower. While during a reentry flight using negative lift, the aerodynamic force acts downward (pointing at geocenter) and greatly increase the ability of the space vehicle to be "captured" by the atmosphere, and the width of corridor is much larger than during the reentry flight using positive lift.

In addition, the last two-thirds of reentry corridor using negative lift is as wide as using positive lift.

### 3.2.2. Properties of Reentry Trajectories (of Spacecraft)

A group of reentry trajectories with minimum  $W_{TPS}$  were solved in this paper with regard to reentry flight using positive lift (given  $m_{00}$  or  $t_{01}-t_{00}$ ) and as a result, the curve  $_{TPS-m_{00}}$  was derived as shown in Fig. 5 with an imaginary line. The trajectory that corresponds to point A in the figure is a reentry trajectory with a minimum ( $_{TPS-m_{00}}$ ). The curve i in Figs. 6-11 represents the reentry trajectory process curve in the atmospheric flight period. Similarly, simulation was made of the reentry flight using negative lift, the simulation results being shown in Fig. 5 with a solid line. The trajectory that corresponds to point B is the reentry trajectory with the minimum ( $W_{TPS}+m_{00}$ ). The curve 2 in Fig. 6-11 stands for the curve signifying the process of reentry trajectory in the atmospheric flight period.

a. Comparison of return cost ( $W_{TPS}+m_{00}$ ). It is known from Fig. 5 that when the mass of  $W_{TPS}$  is uncertain (TPS is at the design stage), the return cost with negative lift is approximately 7% lower than with positive lift, and while  $W_{TPS}$  is certain (space vehicle with TPS already designed), the return cost ( $m_{00}$ ) with negative lift is around 5% lower than with positive lift. This suggests that the effective load of space vehicle during return reentry using negative lift is 5-7% higher

than while using positive lift.

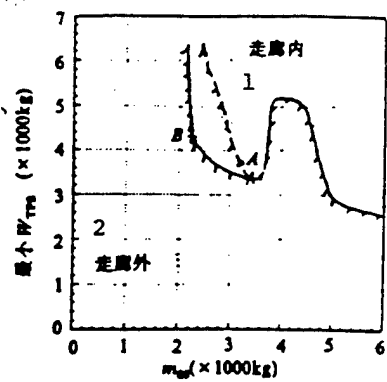


Fig. 5.  $m_{00}$  minimum  $W_{TPS}$  curve  
KEY: (1) inside corridor  
(2) outside Corridor

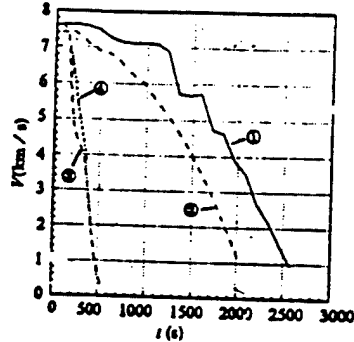


Fig. 6.  $V(t)$ - $t$  curve of optimal reentry trajectory of spacecraft and manned spaceship

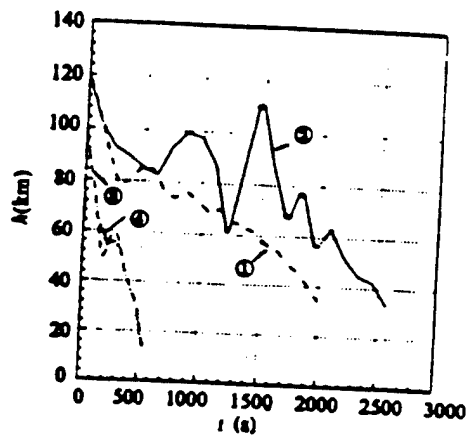


Fig. 7.  $h(t)$ - $t$  curve of optimal reentry trajectory of spacecraft and manned spaceship

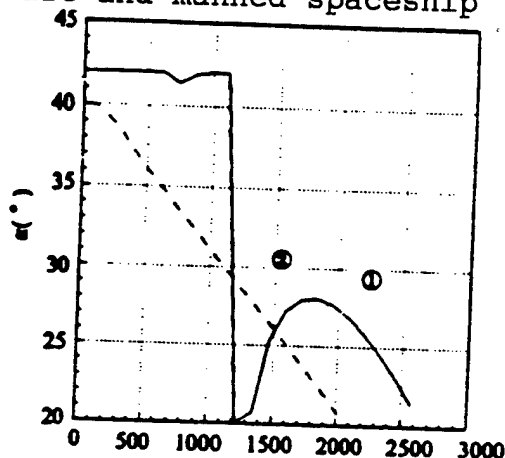


Fig. 8.  $\alpha(t)$ - $t$  curve of optimal reentry control law of spacecraft and manned spaceship

b. During reentry flight using either negative or positive lift, the lower surface and both sides of the space vehicle are windward, while its upper surface is under the wind. Therefore, during reentry using either positive or negative lift, the material mass distribution of TPS of the spacecraft is identical.

b. During reentry flight using either negative or positive lift, the lower surface and both sides of the space vehicle are windward, while its upper surface is under the wind. Therefore,

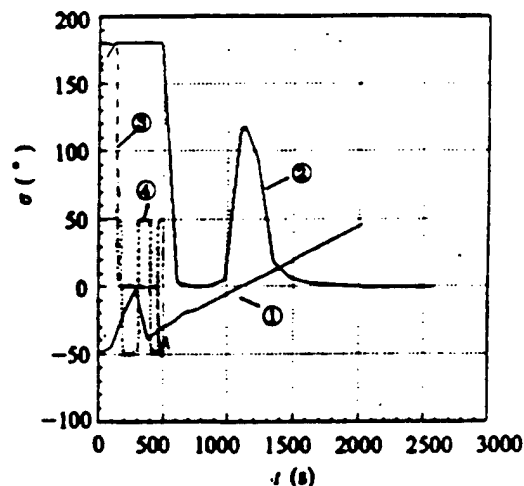


Fig. 9.  $\sigma(t)$ -t curve of optimal reentry control law of spacecraft and manned spaceship

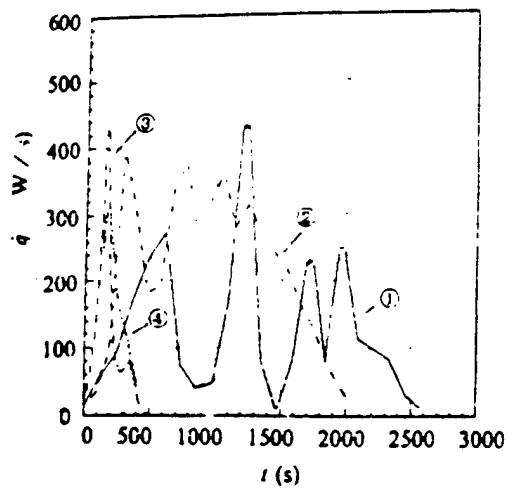


Fig. 10.  $q^\sim t$  curve of aero-dynamically heating rate of optimal reentry trajectory spacecraft and manned spaceship

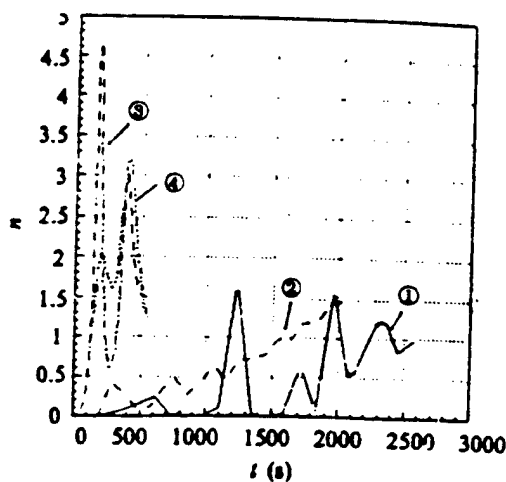


Fig. 11. n-t curve of overload of optimal reentry trajectory of spacecraft and manned spaceship

during reentry using either positive or negative lift, the material mass distribution of TPS of the spacecraft is identical.

c. It is known from Figs. 6-11 that during return reentry using positive lift, a large attack angle ( $40^\circ$ ) is adopted first so as to obtain an extremely large drag and to dissipate huge

amounts of kinetic energy. However, a large attack angle responds to a large lift. To avoid being "bounced out" of the atmosphere, the space vehicle has to fly at a fairly large roll angle (larger than  $-50^{\circ}$  or smaller than  $50^{\circ}$ ) to reduce the projection of the lift within the plumb plane. Next, when the space vehicle is "captured" by the atmosphere, it flies along a trajectory with minimum aerodynamic heating and overload, etc. In addition, the roll angle of the vehicle rolls from  $50^{\circ}$  to  $-50^{\circ}$  so that both sides and the lower surface of the vehicle are subject to uniform heating, favorable for TPS design.

During the return reentry using negative lift, a large attack angle (around  $40^{\circ}$ ) is adopted first for two purposes: one is to obtain a large drag so as to dissipate huge amounts of kinematic energy, while the other purpose is to acquire the maximum negative lift (at a roll angle of  $180^{\circ}$ ) so as to greatly increase the ability of the atmosphere to "capture" the space vehicle. Next, once the vehicle is "captured" by the atmosphere, it flies along a trajectory with minimum aerodynamic heating and overload, etc. Similarly, when the vehicle rolls from  $180^{\circ}$  to  $0^{\circ}$ , one side (or the other side) and the lower surface of the vehicle are subject to uniform heating, which is also in favor of the TPS design.

d. Compared with reentry using positive lift, during reentry using negative lift, the astronaut will be sitting upside down, which is a disadvantage. However, such a sitting position is endurable for the astronaut, just as in a regular jet fighter.

e. Just as for reentry using positive lift, reentry using negative lift is also technically feasible.

### 3.2.3 Effect of Lift-to-Drag Ratio on Reentry Trajectories

Fig. 6-11 list the simulation results of spaceship return reentry using positive and negative lift (where curves 3 and 4, respectively, are reentry using negative lift and reentry using positive lift), including curves showing variation of reentry trajectories, optimal control, and the thermodynamic environment with time. The comparison of trajectory properties between spaceship and spacecraft indicates that during reentry using either positive or negative lift, the space vehicle with a larger lift-to-drag ratio always possesses a larger mobile ability in horizontal and vertical directions, and a smaller aerodynamic heating rate and instantaneous overload. Fig. 1 indicates that the reentry corridor is also much wider.

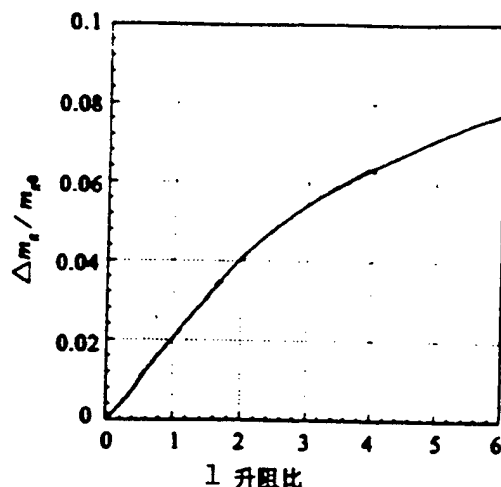


Fig. 12. Curve showing effect of lift-to-drag ratio on effective load of space vehicle during reentry using negative lift

Fig. 12 suggests that compared with reentry using positive lift, the effective load of the space vehicle with a larger lift-to-drag ratio can greatly increase during reentry using negative lift, while the effective load of the space vehicle with a smaller lift-to-drag ratio increases very little. This is because during a reentry using negative lift, space vehicles with a larger lift-to-drag ratio possess an extremely strong ability

to be "captured" by the atmosphere and thereby, the mass of fuel consumed of retro-engines greatly decreases at the deorbiting point.

#### 4. Conclusions

This paper studied the concept of return reentry using negative lift under different lift-to-drag ratios. Also, it calculated reentry corridor, optimal reentry trajectories, etc. during return flight using negative lift, and the calculations were compared with those using positive lift. In addition, the effect of lift-to-drag ratio on reentry trajectories was also analyzed. Since space vehicles with a large lift-to-drag ratio can have an increased effective load, and is feasible technically, it is then believed that the return flight using negative lift is superior to the one using positive lift.

## REFERENCES

1. Nan Ying, Chen Shilu, "Advances in research of reentry trajectories and control of space vehicles, Missile and Launch Vehicle Technology, 1994 (5): 1-10.
2. London, H. S., "Change of satellite orbit plane by aerodynamic maneuvering, Journal of the Aero/space Sciences, 1962, 29(3): 323-332.
3. Mease, K. D., "Optimization of aeroassisted orbital transfer: current status," The Journal of the Astronautical Sciences, 1988, 36(1,2):7-33.
4. Nan Ying, Lu Xuefu, and Chen Shilu, "Reentry corridor of space vehicles and its computational methods," Flight Dynamics, 1993 (3): 34-43.
5. Garcia, F., Jr. and W. T. Fowler, "Thermal protection system weight minimization for the space shuttle through trajectory optimization," Journal of Spacecraft and Rockets, 1974, 11(4):241-245.
6. Lu Xuefu and Nan Ying, "The optimal return trajectory design of space vehicle," AAS93-384, AAS/GSFC International Symposium on Space Flight Dynamics, Greenbelt, Maryland, USA, 1993.4.26-30.
7. Nan Ying, "Reentry trajectory and control of space vehicles" [Degree Thesis], Xi'an, Northwest University of Technology, 1993.
8. Lu Xuefu and Wang Zhigang, "Optimal trajectory and guidance law of manned spacecraft in reentry atmosphere," Proceedings of Third China-Russia-Ukraine Symposium on Astronautical Science and Technology, Xi'an China, 1994:476-480.
9. Nan Ying and Chen Shilu, "The analysis of reentry trajectory of manned space vehicle," Proceedings of Third China-Russia-Ukraine Symposium on Astronautical Science and Technology, Xi'an China, 1994:472-475.
10. Nan Ying, Lu Xuefu, and Chen Shilu, "Research on concept of return reentry using negative lift," Proceedings of Return and Reentry Symposium, 1994.10.

This paper is a research project funded by the Aerospace Foundation and National Postdoctoral Foundation.

This paper was received in November, 1994.

## FOUR PREVENTIVE MEASURES AND GROUNDING OF LAUNCH VEHICLES

Gao Zhi

Beijing Aerospace Automatic Control Institute

**ABSTRACT:** The damage inflicted on launch vehicles that may be caused by thunder and lightning is introduced. The measures of lightning protection, electrostatic-proofing, moisture-proofing, and protection against rainwater when synchronous communications satellites are launched during thunderstorms and rainy weather are summarized, and the grounding is described.

**KEY WORDS:** launch vehicle, lightning protection, antistatic technique, moisture-proofing, protection against rainwater, grounding (electric).

### 1. "Four Preventive Measures" Required in Thunderstorm Season

Occasionally, satellites are required to be launched in thunderstorm season and especially in July, a month with the most lightning storms. For this reason, sufficient attention should be paid to the four preventive measures, namely: lightning protection, electrostatic protection, moisture protection, and protection against rainwater.

In the world history of aerospace, there have been several records of severe lightning damage to launch vehicles. In

November, 1969, the American Saturn-mounted Apollo 12 was launched. At first, it was on a normal flight, yet 36.5s after take-off when it was traveling at an altitude of approximately 1920m, a lightning stroke occurred running from the cloud layer down to the ground via this rocket. Then, 52s after take-off when the rocket was at approximately 4300m high, another lightning strike followed, which extended from the upper cloud layer to the lower cloud layer by way of the same rocket.

On March 26, 1987, the United States launched a U.S. Navy fleet communications satellite-6 by using the Cosmos-Centaurus-6 launch vehicle at the Kennedy Space Center at Cape Canaveral. Shortly after takeoff, the rocket exploded. In investigations of this accident, it was shown, by means of recovered rocket fragments, that the rocket was hit by lightning, i.e., it either disintegrated or failed in many functions because of lightning.

Similarly, static electricity can also frequently cause erroneous blasting of electric blast tubes in rocket industry products. These kinds of accidents may also result from electromagnetic radiation generated by radio or radar transmitters, which can interfere with equipment and instruments. Even more accidents may originate from electromagnetic induction, leakage, cross electricity, poor grounding, or operations contrary to regulations.

According to statistics kept at meteorology departments in China, the strongest lightning current ever recorded in this country was 330kA. The probability of lightning stronger than 30kA is 0.52, which is intermediate level lightning. During Thunderstorm H that covered 40km, lightning with a maximum intensity of 300kA was detected, in which the electric field intensity was 30kV/m. Sometimes lightning currents are 120kV with an electric field intensity of 13.2kV/m. And there are even more lightning currents of intermediate intensity.

## 2. Lightning Protection Measures for Launch Vehicles

### 2.1. Lightning Mechanism

To adopt lightning protection measures for launch vehicles, it is needed to first understand the formation, performance, and destructive mechanism of lightning.

It is 245 years since Franklin started to study lightning phenomena in nature in 1749. Relative to this date, there has been only somewhat more than 40 years of research on lightning protection for launch vehicles. In addition, only a few publications specialize on this subject abroad.

Much research was done in foreign countries with regard to the lightning process and performance and a number of papers were published in this area. Lightning can be defined as instantaneous arc discharges from heavy currents along paths measured in kilometers. When the capacity of the electric charge and the corresponding electric field intensity in space or clouds are high enough to cause air breakdown, lightning occurs. Lightning can take place inside a cloud, between clouds, between a cloud and the ground, or between a cloud and the surrounding atmosphere. Prior to lightning, the atmospheric electric field  $E_y$  can be expressed in Eq. (1):

$$E_y = \frac{1.789 \times 10^{10} H Q_0}{(H^2 + d^2)^{3/2}} \quad (1)$$

where  $E_y$  is the vertical component of the electric field (V/m);  $H$  is the height of the electric charge from the ground (m);  $Q_0$  is the charge capacity at the center of the lightning cloud (C);  $d$  is the distance from the projection point of the charge on the ground (m).

The geodetic electric field  $E_r$  can be expressed in Eq. (2):

$$Er = \frac{2}{\pi} \cdot \frac{I_0}{r_0} \cdot \frac{V}{V_0} \cdot \sqrt{\frac{PZ_0}{V_0 T}} \cdot \sqrt{\frac{t}{T}} \quad (2)$$

where  $I_0$  is the maximum current of the leader (kA);  $r_0$  is the distance from the leader (m);  $V$  is the velocity of the leader (m/s);  $V_0$  is the speed of light  $3 \times 10^8$  m/s;  $P$  is geodetic resistance ( $\Omega \cdot m$ );  $Z_0$  is characteristic impedance ( $30\Omega$ );  $t$  is time (s);  $T$  is the return streamer time (s).

The magnetic field produced by the leader current  $B$  can be expressed in Eq. (3):

$$B = \frac{2Z_0 I_0 V}{V_0^2 \tau r_0} \quad (3)$$

where  $\tau$  is the time measured from the arrival of the leading edge of the magnetic field.

Generally speaking, each flash of lightning includes three or four strokes. A lightning process is usually completed in several stages, such as stepped guide, return stroke, continuous current, javelin guide, and secondary shock.

As for the performance of lightning, general lightning performance data between the clouds and the ground, the statistical distribution characteristics of lightning parameters, and the discharge performance of natural lightning have been reported from foreign sources. Here, we briefly introduce various possible damaging effects of direct lightning and indirect lightning on launch vehicles as well as the equipment of ground test system, engine control system, and fuel system, etc.

#### 2.1.1. Effect of High Voltage

High-voltage and intensive electric fields (including electrostatic fields and dynamic electric fields) can cause

perforation, fracture, and deformation of insulating materials and overlapping structures. Generally speaking, the high-voltage electron currents proper cause little damage, yet the follow-up heavy stroke currents, flowing along the paths of electron currents, may generate high temperatures, high pressures, and shock waves, which are highly damaging. In addition, sparks as a result of high-voltage and intensive electric fields are a major threat to fuel systems and electric blasting devices as rocket industry products. Further, the large voltage drop caused by heavy currents can also damage insulation of internal wires.

#### 2.1.2. Effect of Intensive Currents

Under direct lightning, the strong shock currents that pass through the surface of the case may reach 200kA. These currents themselves will not generate large thermal effects and corrosion in large conducting structures, but the electromagnetic force originating from the interaction between the strong pulsed magnetic field (dynamic magnetic field) caused by these currents and the intensive electric currents can lead to ripping or bending of materials. If there is no enough current capacity in the wire through which the lightning currents pass, the wire will explode and produce great damage. As for the great induction voltage caused by  $L(di/dt)$ , it can give rise to breakdown or ignition.

#### 2.1.3. Effect of Induction Cross-coupling

Most lightning-related accidents result from the strong induction voltage (as strong as thousands of watts) occurring in cable networks and electronic circuits. The intensive magnetic field and leakage currents generated by lightning shock currents can produce electromagnetic cross-coupling. Electric fields have a weak ability to penetrate launch vehicles, while magnetic fields can strongly penetrate them. The electromagnetic cross-

coupling is associated with the growth rate of lightning strike currents and may reach  $100\text{kA}/\mu\text{s}$ . Since large numbers of solid circuits and digital control circuits are being employed, which have easy access to interference, it is vitally important to reduce the destructive effects of induction voltage (through rational wiring, and proper grounding and shielding).

#### 2.1.4. Effect of Heavy Electric Charge

Like an electric welding machine, direct currents of hundreds of amperes can produce ablation, melt metallic wires, and ignite combustibles in hundreds of milliseconds. Also, they can damage organic synthetic materials.

#### 2.1.5. Effect of Electromagnetic Waves

Within 100km from a launch complex, lightning can generate electromagnetic waves under 30kHz (with a lightning frequency approximately 1MHz generally), which can produce interference to electrical measurement and electrical control systems, such as the control system and telemetry system of launch vehicles.

In summary, lightning has effects on launch vehicles in basically three patterns: a. electric field penetration; b. electromagnetic cross-coupling; and c. direct cross-coupling. All the three patterns can affect launch vehicles, but the most significant one is electromagnetic cross-coupling. Actually, most of the lightning-induced launch vehicle accidents are caused by lightning-related cross-coupling.

It is a rather complex problem to protect launch vehicles and their ground equipment including test system, launch control system and fueling system against lightning. The following is a summary of lightning protection measures intended for launch vehicles.

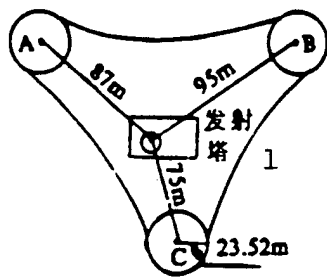


Fig. 1. Lightning protection tower around launching tower  
 KEY: (1) launching tower

## 2.2. Lightning Protection Measures Required for Launch Sites

To protect launch sites from lightning, it is required to consider lightning protection, lightning arresting, lightning guard, and grounding in their design and construction.

- a. Three lightning protection towers should be built around a launch site. Each tower should have an independent grounding setup, whose grounding resistance should not be smaller than 10 as shown in Fig. 1. The height of the lightning rod must be 1.5-2 times that of the launch tower.
- b. In the main direction of the lightning strike, a lightning arrester rod should be mounted much higher than the launch tower as well as the lightning rod. The lightning arrester rod should be able to effectively arrest lightning with currents under 30kA.
- c. Under each lightning protection tower, several grounding piles made of stainless steel should be buried below the lightning arrester rod, which are connected to one another with flat steel as shown in Fig. 2.

As indicated in Fig. 2, there is a total of 13 grounding piles buried under tower A, while nine grounding piles are buried under towers B and C, respectively. Each pile is 2.5m in length and  $\Phi 65\text{mm}$  in diameter. The connecting flat steel is  $40 \times 4\text{mm}^2$ .

d. There is a unified grounding network of uniform pressure set up on the launch site, whose grounding resistance is no more than  $1\Omega$ . This network should be separated from the lightning protection grounding network belonging to the lightning protection tower at a distance of more than 15m.

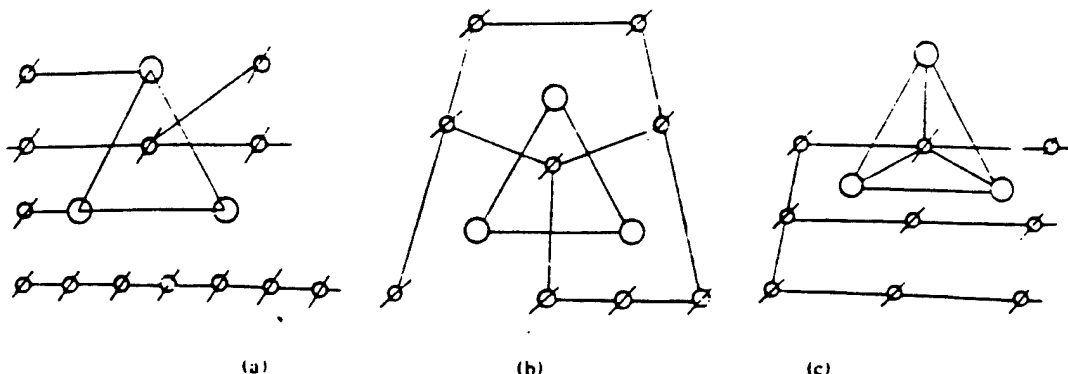


Fig. 2. Arrangement of grounding piles under lightning protection towers

e. Once enclosed, the mobile working platform of the frame around the launch tower is equivalent to a Faraday shield cage and the platform is securely connected with the grounding network of uniform pressure at the launch site. On the working platform there are 16 soft equipotential cables with a cross section no less than  $35\text{mm}^2$  and resistance no more than  $20\text{m}\Omega$ , which, connected to the cases of individual structural sections of the rocket, form an equipotential body. This can ensure that when lightning strikes the launch tower, over 70% of the lightning current would be carried away through its frame, thus diminishing the shock and damage to the equipment and instruments in the rocket.

## 2.3 Lightning Protection Measures Taken for Launch Vehicles

### 2.3.1 Lightning Protection Design

The major lightning protection measure taken for launch vehicles is to make the rocket structure an ideal shield and securely grounded.

a. When lightning currents pass through the outside of the rocket casing, over 500V induction voltage and sparks will occur inside the rocket, which may damage its electrical measurement and electrical control systems, such as the control system. To avoid this threat, excellent equipotential connections between various sections of the rocket and its overall resistance no more than  $100\text{m}\Omega$  are required in the overall rocket design. While in designing the rocket body, connection between its various structures is required to be in an overlapping form so as to protect it from lightning, the cross section of overlapping wires being no less than  $20\text{mm}^2$ , and the overlapping resistance being no more than  $10\text{m}\Omega$ . It is also required that the lightning current can safely pass through in the case when sealing measure is taken to prevent corrosion.

b. To ensure the integrity of the rocket casing as well as the symmetry and uniformity of the lightning current, metallic parts including fairings, hatchways, hatches, etc., that are mounted on the rocket body should be securely connected to the body through the main overlapping wire ( $<200\text{mm}$ ). The overlapping resistance of each overlapping surface should not exceed  $1\text{m}\Omega$ , and the overlapping resistance of the movable metallic surface should not exceed  $5\text{m}\Omega$ .

c. The overlapping resistance between the instruments of various systems mounted inside the rocket and its structures should not exceed  $20\text{m}\Omega$ . Appropriate measures should be taken for

those mounted in a floating way. Spark-extinguishing damping circuits should be adopted for inductance loads, such as power-driven air valves of hydrogen-oxygen engines, attitude control electromagnetic valves, relay circuits, etc.

d. Each engine should overlap the launch rocket body at least in two places, and its resistance value should not exceed  $10m\Omega$ .

e. Short-circuit plugs (sockets) are designed for the plugging pieces of rocket industry products including electrical blasting tubes and explosive bolts. When the rocket industry products are connected to the circuits of the system, the short-circuit plugs (sockets) protection, grounding and shields should be employed. These are used to prevent lightning currents from producing sparks when they flow through rocket casing covers, and to prevent possible threats brought to the electrical blasting tubes by electromagnetic cross-coupling occurring when lightning currents pass through hatches as well as the high frequency electromagnetic pulses.

f. On the four tail fins of the first stage of the launch vehicle, respectively are mounted three electrostatic discharge devices (12 in total). The distance between the discharge devices is no less than 300mm. The overlapping resistance between the mounting base of the discharge device and the rocket body should not exceed  $10m\Omega$ .

g. The launch vehicle connects with the machinery of the satellite through its support. This connection must be of equal potential with a contact resistance at the joint surface no more than  $10m\Omega$ . The electrical systems of the rocket and the satellite adopt single-point grounding mode.

h. The rear of the launch vehicle connects to the fastener

(pile) in the equal pressure grounding network at the launch site through a grounding line with a cross section no less than  $35\text{mm}^2$  and a resistance no more than  $25\text{m}\Omega$ . The contact resistance of the fastener is no more than  $10\text{m}\Omega$ . When the rocket takes off, the fastener automatically comes off. The contact resistance between the rocket and fastener is no more than  $5\text{m}\Omega$ .

### 2.3.2. Lightning Protection Measures for the Launching Site

a. The rod system between the first and second rocket stages is shielded with tinfoil cloth to protect it from being penetrated by lightning electromagnetic waves in a thunderstorm.

b. Lightning protection shields and grounding measures are adopted for all ground test cables, control cables, fueling pipes and gas supply pipes that are connected with the rocket. The shielding covers of these cables, pipes, and wires are connected, with a grounding pile erected every 10-20m, to the equal pressure grounding mesh, their contact resistance being no more than  $5\text{m}\Omega$ .

c. Through a special treatment, the dropping and deplugging of plugs of the ground test cables and the dropping and deplugging sockets of the rocket casing are in a reliable and coaxial connection.

d. All the test and control cables that connect to the launch vehicle should be unplugged as long as an over  $30\text{kA}$  lightning is forecast.

e. Some of the instruments and equipment installed in the launch vehicle are floating, such as the digital control computer of the control system, the power supply of the computer, and the rate gyroscope (insulated from the rocket). The first-stage pitch and yaw gyroscope is mounted in the interbay section of the

second stage, which is already safe owing to the shield of the rocket casing. The first-stage roll-rate gyroscope is installed below the rod system of the first and second stages and is wrapped up with a metal fairing connected to the rocket body, and therefore, it is also safe. The second-stage pitch- and yaw-rate gyroscopes are mounted on the external side of the third-stage skirt casing, next to the telemetry antenna. In this case, it is required that the fairing of the rate gyroscope should be made of glass-reinforced steel materials that allow waves to penetrate, and they should not be made of reflecting metal materials. With such a scenario, it is decided that the fairing of glass-reinforced steel be covered with a copper mesh and is connected with the rocket casing so as to protect it from lightning damage. But prior to launch, the copper mesh should be taken off so as not to affect the transmission and reception of telemetry signals.

The digital computer and its power supply installed in the instrument bay are made insulated from the rocket casing, because the instrument bay itself is the logical ground. Before the fairing of the satellite is mounted, the rocket should be erected on the launch tower frame for a long time. In this case, the following three lightning protection arrangements must be made for the foregoing two instruments in July when lightning is frequent:

The first arrangement: the whole equipment should be covered with a shield mesh that allows heavy currents to pass to simulate a Faraday cage. Actually, this copper mesh serves as a shield cover for the instruments, which is composed of three insulating cotton cloth layers with the copper mesh in between. Two grounding lines are welded to the copper mesh that are connected to one another with a shield casing pipe.

The second arrangement: two more grounding lines are

respectively connected to the case (i.e., logical ground) of these two instruments. All the four grounding lines are connected with the rocket casing as soon as a test is over, while prior to the test, they must be disconnected. Otherwise, the logical ground of the rocket machinery will be connected with the rocket case and cause a hyper-difference in the test results, and hyper-difference marks will appear on the screen.

The third arrangement: the dust-protecting support of the instrument bay is covered with a cylindrical cover made from the copper mesh, which is securely connected to the rocket casing with a grounding wire which allows heavy currents to pass. In this case, all the instruments in the instrument bay can be protected, including the control system instruments, such as digital computer and platform, as well as telemetry and outer space measurement instruments and all the control and liquid level instruments.

### 3. Measures for Electrostatic Protection

a. Liquid hydrogen and liquid oxygen are high-energy propellants. Liquid hydrogen, a colorless, tasteless and transparent liquid with a low boiling point (-253°C), can frostbite human beings and make materials bristle. Liquid hydrogen has an extremely high ability to leak and can vaporize quickly. The velocity of its leakage (volume flow rate) is approximately 100 times that of gasoline. When temperature rises to 0°C, its volume increases by around 800 times. Hydrogen is inflammable, easy to explode, colorless, tasteless and without smell, difficult to distinguish. Further, hydrogen has very low ignition energy. A slight strike, friction, discharge among different potentials, ignition of various bursters, open fire, hot gas flow, smoke, lightning induction or electromagnetic radiation, etc.--all these can ignite the mixture of liquid

hydrogen with air.

In an open environment, the mixture of liquid hydrogen with air usually self-explodes and burns, and the hot gas thus generated can rapidly expand and form a pressure wave which can damage the buildings around. When the concentration of liquid hydrogen increases to the detonation limits, it will explode as long as there is any ignition source nearby. When deflagration converts to detonation, flame and shock waves can transmit at supersonic speeds, producing local pressure intensities 300 times as high as the initial pressure intensity. Thus, detonation can provide an extremely strong destructive force. The shock waves can damage human bodies, mainly causing blood vessel rupturing and further, hypodermic bleeding or internal organ bleeding and particularly, liver, spleen and lung rupture. With an excess pressure of 0.021MPa, shock waves can twist people up and eject them. When the overpressure reaches 0.035MPa, it can lead to eardrum rupture; when it is even stronger, it can directly damage human internal organs or cause death.

Liquid hydrogen possesses electrostatic cumulative properties. With a resistance between  $10^{11}$  and  $10^{19}$   $\Omega/\text{cm}$ , liquid hydrogen can easily accumulate high insulation substances of electrostatic charge and easily produce extremely high electrostatic potentials during high speed flow, leakage spray, or friction separation. If there is solid dust in liquid hydrogen, its electrostatic potential may reach 7.2kV; if it contains moisture, its electrostatic potential can rise to 5.4kV; when the saturated vapor in the liquid hydrogen is totally discharged at a high speed, its electrostatic potential may reach 12kV. Since liquid hydrogen has an intensity of breakdown electrical field of 15.5kV/cm while its ignition ability is extremely low, it is truly a great danger with accumulated static electricity. Since cryogenic liquid hydrogen has a density

larger than that of constant-temperature liquid hydrogen, it is even more dangerous with accumulated static electricity.

b. Launch vehicles are equipped with many kinds of rocket industry products, such as electrical blasting tubes, thrust rockets, and retro-rockets, and igniters. Before launch, after takeoff and in flight, the launch vehicles can be electrified due to charges generated by induction of atmospheric potential gradients or by electrostatic charges caused by occasional friction, which can give rise to potential differences. When the potential difference grows to a certain value, the vehicles can produce spark discharge and result in erroneous explosion of rocket industry products including electrical blasting tubes.

c. In operation, operators not wearing electrostatic protection clothes, shoes, socks, hats, gloves, and particularly, those wearing manmade-fiber clothing and shoes with plastic soles will carry static electricity (evidenced by sparks and crackling sounds in the dark when operators take off their chemical fiber or fiber-blended clothes). And when operators with static electricity touch well-grounded equipment or shake hands with other people, sparks may be evoked, which can serve as a potential source for an accident.

d. Among the electrostatic protection measures taken for launch vehicles are:

1) Railway liquid hydrogen-transporting or carrying tanks and carriages should be connected through wires to form equal potentials and properly grounded;

2) The metallic pipes and cables of the hydrogen charge and discharge systems should be armed with lightning arresters; a grounding pile should be buried every 10-20m between cable shield covers with a grounding resistance no more than  $10m\Omega$ ;

3) To prevent spark discharge generated by electrostatic induction, the circuits of rocket industry products including electrical blasting tubes and explosive bolts should all be grounded with short-circuit plugs (sockets) to protect them from erroneous explosion. After evaluation of the loop resistance before launch, the short-circuit plugs (sockets) should be unplugged, and the equipment should be connected to the system;

4) All materials on site are required (regular fuel, oxidizer, liquid hydrogen, liquid oxygen, going to the tower, etc.) to wear combustion-resistant and electrostatic protection clothes to GB1204 standard, and electrostatic protection plastic-sole shoes, electricity-conducting plastic-soled shoes, electrostatic-protective socks, hats or pure cotton clothing and hats to GB4385 standard. The clothes should be separate for the upper and lower parts of the body so that they are easily removed in emergencies;

5) The body of an operator is a static electrification device and also a capacitor. Therefore, each operator must wear a grounding bracelet on his arm while operating and particularly installing rocket industry products, such as electrical blasting tubes, explosive bolts, or igniters.

6) The following articles are prohibited on site: any fire source, smoking, chemical fiber, nylon or fur clothes and spiked heel shoes.

7) To discharge the static electricity carried by human bodies, well-grounded static electricity-removing copper clubs are placed at the door, elevators, and staircases. Operators must touch the clubs with their hands before entering the site or going to the launch tower near the launch vehicle so as to ensure the safety of rocket, equipment, satellite, and personnel.

8) To prevent static electricity, lightning and interference, the instruments and cables belonging to different systems of the rocket should be shielded (with copper meshes, shielded clothing, shielded wires, copper-coated wires, etc.). Some key sections of the control system should even be double-shielded.

e. Grounding is vitally important and fairly complicated. It is extremely significant and efficient for preventing lightning, static electricity, electromagnetic radiation produced by radio telemetry transmitters and outer space measurement transponders, and electromagnetic induction generated through distribution parameters L, C, R, and other sources.

Grounding can prevent charge buildup. Capacitors can be formed between ungrounded conductors and ground or between ungrounded conductors, and capacity can lead to charge buildup. To destroy the conditions for charge buildup, various items on the operation site (including the rocket itself, frame of launch tower, working platform; support; testing, control and transmission equipment; regular and hydrogen-oxygen fueling equipment, rarefying equipment; telemetry and outer space measurement equipment; ventilation and air conditioning; gas supply and gas discharge equipment and cable shield covers, etc.) must be appropriately grounded.

1) Special grounding devices must be buried, respectively, for the control system, telemetry/outer space measurement system, satellite system, power system, regular fueling system and hydrogen-oxygen charge and discharge system, electronic computer, precision electronic instruments and equipment, general electronic apparatus, shield body, electrostatic and electromagnetic protection facilities. Grounding wires and neutral wires of power equipment, water supply pipes and sewers or central heating pipes are strictly prohibited from being used

in place of grounding devices. This kind of grounding is schematically shown in Fig. 3.

The special grounding devices are required to be installed far away from the lightning protection grounding devices and the grounding devices of the power equipment. Usually, these grounding devices should be buried no less than 15m in depth at an interval of no less than 5m.

2) Since the special grounding wires for control, telemetry and outer space measurement and satellite are connected with one another in the cable ditch under the launch tower and then connected to the equal pressure grounding mesh at the launch site with a thick and soft shielded cable, mutual interference between them is fairly severe. When the main computer of the measurement and control system is closed, the collection machine bay placed in the operating room on the frame of the tower still receives a set of coded signals, which are believed to come from the single line system of the outside system through a common grounding wire. This is rather a grounding chaos, i.e., mutual effect and mutual interference among technological grounding, operating grounding, protection zeroing, and protection grounding. To control the system, we installed an independent grounding device, which is thoroughly cut off from other grounding devices. Besides, the grounding wires of the voltage-stabilized source of the collection machine bay are also completely cut off from other grounding devices so that interference can be eliminated.

4) All the instruments of the measurement and control equipment are grounded. To prevent low frequency (including tone frequency) interference, the principle of single-point grounding must be obeyed.

5) To prevent high-frequency interference, the shield covers of the shield cables are grounded at two ends. To prevent

lightning destruction, multiple grounding is adopted for cable shield covers to reduce the lightning currents that pass through the cable and decrease the effect of lightning on the ground equipment that connects to the cable.

6) All neutral wires for protection zeroing and ground wires for grounding protection must be securely connected. They are not allowed to be cross-connected to any switches and fuses.

7) The operating room in the launch tower is required to be protected from electromagnetic interference. Its doors and windows should be grounded with copper mesh shields to reduce the foregoing electromagnetic interference.

8) Grounding wire fasteners (piles) must be properly set up for the equal-pressure ground mesh, the frame of the launch tower, cable well, cable trend, and rocket casing. The length of the grounding wires should be within 200mm and also, they should be thick. Attention should be paid to minimizing the inductance of the grounding wires. Otherwise, excessively long grounding wires (with large inductance) may introduce outer interference or noise, unfavorable for lightning protection.

The resistance of technological grounding items including electrical measurement and electrical control system, precision electronic instruments and equipment, electronic computers, etc. is required not to exceed  $1\Omega$ ; the resistance of other operation grounding is required not to exceed  $4\Omega$ ; the grounding resistance of the lightning protection tower is required not to exceed  $10\Omega$ .

#### 4. Moisture-Protective Measures

Occasionally, satellites are launched in the thunderstorm season when the weather is changeable and extremely wet. Due to the moisture as well as the corrosion effect of harmful gases,

the insulation resistance will decrease or even short. As a result, direct or alternate current leakage or cross

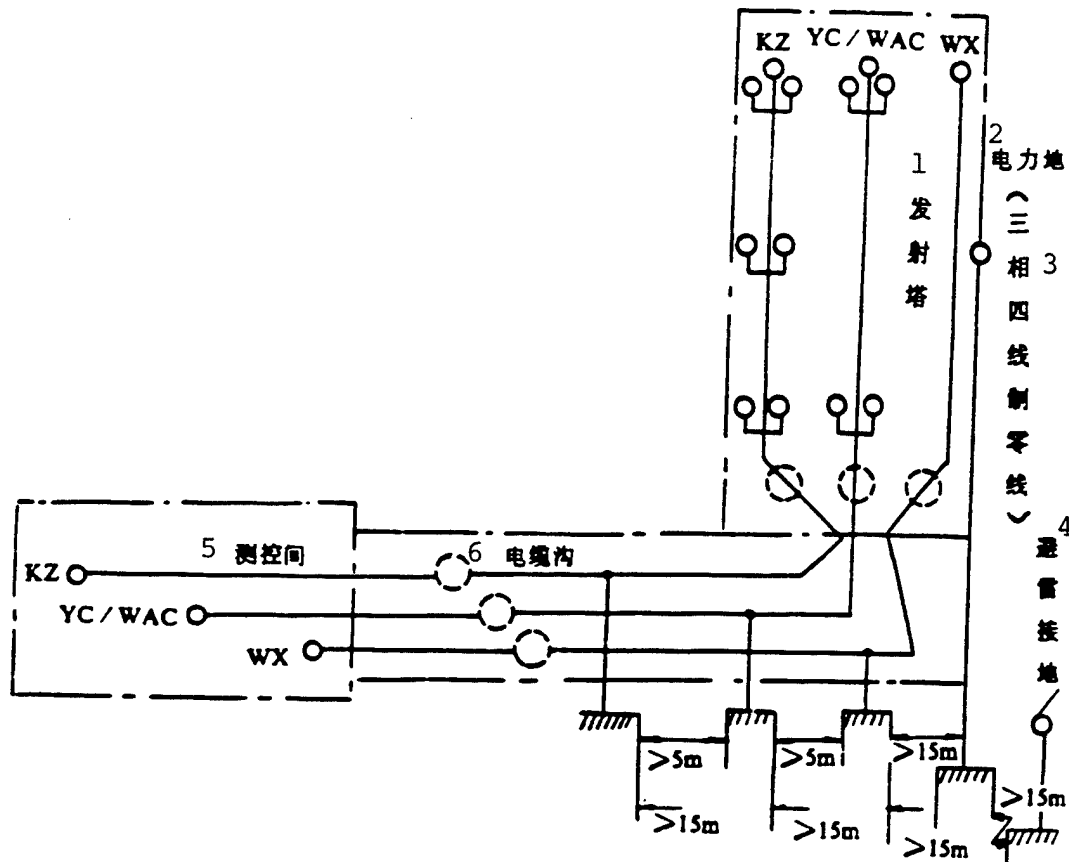


Fig. 3. Special independent grounding wires

KEY:

- (1) Launch tower
- (2) Power ground
- (3) (Neutral wire of 3-phase and 4-wire system)
- (4) Lightning protection grounding
- (5) Measurement and control room
- (6) Cable well

electrification may happen (between cable shield covers and core wires, or between core wires) and bring about serious consequences.

Since the wet ground cables will decrease the insulation resistance, they should be dried by using an electrical air blower. Different moisture-protective measures should be taken

for different rocket sections as follows:

- a. Before the fairing and satellite are mounted, the mobile working platform of the launch tower functions as a closed space, for which air conditioning should be applied to ensure the required moisture, temperature and cleanliness;
- b. After the fairing and satellite are mounted, air conditioning should be used inside the satellite fairing to ensure the required moisture and temperature in the instrument cabin of the rocket and satellite;
- c. Heated nitrogen and helium gases should be blown into the third-stage hydrogen-oxygen engine bay and rear skirt casing to prevent blasting and moisture;
- d. Dry wind should be blown into the first- to the second-stage inter-bay section and the first- to the second-stage engine bay through thick and hard plastic pipes so as to prevent moisture;
- e. Outside the rocket cover, the cable bundles and plugs (sockets) in the low-row cable fairings should be wrapped with waterproof cloth and adhesive tapes;
- f. The connectors should be plugged and wrapped with waterproof adhesive tapes;
- g. Waterproof rubber covers are used for telemetry system, hydrogen-oxygen loading and discharge system, and the joints of the ground cable plugging items;
- h. The first-stage rod system should be closely wrapped with tinfoil cloth to prevent lightning, moisture and rainwater.

## 5. Rainwater Prevention Measures

Since rainwater contains conducting ions, it can affect the performance of insulation and lead to leakage and cross-coupled electricity. When long-soaked in rainwater containing harmful gases, instruments and equipment will be corroded, rusted or damaged, resulting in incalculable consequences to detection and test flights. In this case, the following rainwater prevention measures can be taken:

- a. When rain is forecast, the mobile working platform of the launch tower should be enclosed, and the upper part of the launch rocket should be tightly covered with waterproof canvas;
- b. Waterproof rubber rings were efficiently designed, constructed and matched for the control-oriented dropping plugs and sockets;
- c. The joints of individual sections should be sealed with waterproof adhesive tapes; the overlapping parts of long-row fairings, separating socket fairings and the fairings of speed gyroscopes should be stuck with waterproof adhesive tapes or waterproof films;
- d. The cable bundles inside the long row fairings are covered with nylon waterproof covers;
- e. The doors, windows, and hatches of individual cabin sections of the rocket should be sealed and covered for their upper parts so as to prevent rainwater from coming in;
- f. The upper part of the temporarily open cable fairings, the upper part of separating plugs (sockets), the upper part of the unplugged hatches or the upper part of any openings should be covered with waterproof films to prevent rainwater;

g. All the ground test equipment, instruments and equivalent devices that are placed on the working platform of the launch tower should be covered with canvas or nylon films and well fixed;

h. Ground leaks and hidden wells should be dug for drainage purposes in the cable trench at the bottom of the cable well of the launch tower;

i. During fueling, quilts and towels should be used to wrap up the rocket body at individual bay sections (the third, second, and first stages) to prevent the liquid generated due to air cooling and condensation from flowing into the rocket.

## 6. Conclusions

Despite the fact that effective preventive measures have been worked out to prevent lightning, static electricity, moisture and rainwater, still, a great deal remains to be done in realizing all-weather launches.

a. In-depth study of lightning protection design and effective lightning protection measures for launch vehicles;

b. Study of remote-sensing techniques for detecting electrical fields in cloud layers;

c. Development of small rocket detecting techniques for electrical fields in clouds, which is aimed to find out the relationship between the thickness of cloud layers and intensity of electrical fields;

d. Study and measurement of the charge on the casing of in-flight rockets and satellites, the space charge at the rear of the rocket in flight and the conductive performance of the engine

(both regular and hydrogen-oxygen high-energy engines) flames;

e. Study of the relationship between the speed and size of the high-speed conductor-induced lightning, and the cloud thickness and electrical field intensity. The purpose of this study is to make the conductors carried by small rockets induce lightning prior to the rocket launch so that the potential gradient in the clouds may decrease to below the critical value, which favors a safe launch.

## REFERENCES

1. Li Yiming, "Lightning and rockets," Guidance and Control, 1977.(1).
2. Li Yiming, "Lightning, static electricity, radio frequency electromagnetic radiation and electromagnetic induction protection for rocket-oriented electrical blasting devices," Guidance and Control, 1980.(1)

This paper was received on November 20, 1994.

-----

## A DISASTROUS EXPLOSION IN THE FORMER USSR LUNAR ROCKET TEST

Recently, a Russian TV station disclosed that a disastrous explosion happened on February 21, 1969, during the first test flight of the huge lunar rocket N1 developed in the former Soviet Union, killing 91 test staff members. This accident was made public for the first time, though there have been occasional reports on the development and testing of the rocket N1 in recent years. This disastrous accident is one with the highest recorded death toll in aerospace history in the former Soviet Union. On October 24, 1960, a similar accident took place at the Baikonur Launch Site, resulting in 56 deaths, including Wanzhilin, a Soviet Marshall of Artillery. On March 18, 1980, 51 people died in the explosion of a Vostok rocket at the Prizhisk Launch Site.

The rocket N1 is a lunar rocket developed in the former Soviet Union from the late sixties to early seventies. Originally, it was designed to send two persons to the moon, and one of them was supposed to land on the moon. From February, 1969, to November, 1972, the Soviets carried out four test flights of this rocket but all ended in failure. Then the Soviet department concerned decided to cancel the rocket development program.

## FRANCE IS EXPERIMENTING WITH SUBMARINE-LAUNCHED M45 MISSILE

Recently, the French Navy successfully completed the first underwater ignition test of its M45 submarine-launched strategic ballistic missile. Launched at the western coast of France, the missile flew 23 minutes and eventually landed in the target area near Andres Islands 4500km away. M45 is a modified version of M4 that went into service in 1985. Composed of three stages, the M45 was developed by French Aeronautics and Astronautics Inc., as the prime contractor, with an investment of \$800 million. This missile is scheduled to enter service in March, 1996, on four French new-generation missile submarines with 16 missiles in each submarine.

## ----- BRITAIN IS DEVELOPING HYBRID ENGINE

Britain is conducting a series of tests on a solid-liquid hybrid engine using its royal military equipment test facilities. The aim of the tests is to prepare this engine for launching a small 300kg satellite in 1996. These tests are undertaken by the Satellite Engineering Research and Observation Satellite Technology Center, who are confident in applying this engine in small satellite orbital transfer. This kind of engine possesses a thrust 41kg and adopts a solid incendiary agent and liquid oxygen as its propellant. In addition, this engine can be restarted repeatedly.

PROGRAM DESIGN OF DEFORMATION  
OF BALL BEARINGS UNDER PRELOADS

Zhu Jianghong

Beijing Institute of Control Devices

**ABSTRACT:** Ball bearings, as vital supporting elements, are widely used in inertial instruments (inertial platform and gyroscopes). Deformation and stiffness of radial-thrust ball bearings are analyzed and a FORTRAN program is written with the Powell Optimum Method. The program can be used to calculate the deformation and contact stress of various ball bearing arrangements under conditions of different preloads and combined radial and axial combined working loads. It provides the means for analyzing the influence of the different structural parameters and loads on the stiffness of bearings. The experimental results are coincident with those of the theoretical calculations.

**KEY WORDS:** gyroscope bearing, deformation, computer programming.

## SYMBOLS

$D_w$  - diameter of balls  
 $Z$  - number of balls  
 $\alpha_0$  - nominal contact angle  
 $R_i$  - radius of curvature of inner grooves  
 $R_o$  - radius of curvature of outer grooves  
 $f_i$  - radius of curvature coefficient of inner grooves  
 $f_o$  - radius of curvature coefficient of outer grooves  
 $a$  - major semiaxis of contact ellipse  
 $b$  - minor semiaxis of contact ellipse  
 $E$  - modulus of elasticity of materials  
 $i$  - Poisson ratio  
 $\delta_i$  - elastic approach volume of contact between balls and inner rings  
 $\delta_o$  - elastic approach volume of contact between balls and outer rings  
 $\Sigma\rho$  - curvature sum function  
 $F(\rho)$  - curvature difference function  
 $F_{ao}$  - axial preload  
 $\delta_o$  - axial predeformation  
 $F_a$  - axial operating force  
 $\delta_a$  - axial relative displacement of sleeve gaskets  
 $F_r$  - radial operating force  
 $\delta_r$  - radial relative displacement of sleeve gaskets  
 $Q$  - contact load between balls and sleeve gaskets  
 $\delta_n$  - normal contact deformation between balls and inner and outer races  
 $A_o$  - distance between groove curvature centers of inner and outer races prior to loading  
 $A$  - distance between groove curvature centers of inner and outer races after loading  
 $Q_o$  - maximum load on balls  
 $\sigma$  - contact stress  
 $m$  - number of bearing columns

- $\sigma$  - load on balls at angular location
- $K_n$  - normal elastic coefficient
- $K_a$  - axial elastic coefficient
- $K_r$  - radial elastic coefficient
- $Q_i$  - internal stress of  $j$ -th ball

## 1. Introduction

As vital supporting elements, ball bearings are widely used in inertial instruments and especially in inertially stabilized platforms. Bearings play a part in supporting the total weight of the platform itself as well as the elements of inner and outer rings. When the main machine operates under a heavy overload, shock and vibrations, bearings are required to have a rigidity large enough to ensure the locational accuracy of the instruments on the platform. It is for this reason that preloaded bearing pairs are employed to increase the supporting rigidity. However, there has not been any well developed computational method in our country that can be applied to calculate the deformation and stress of preloaded bearing pairs. These kinds of calculations, affected by many factors, can only be realized through computers instead of a simple computational formula.

Early in the sixties, T. A. Harris, based on the book Ball and Roller Bearing Engineering by A. Palmgren, Analysis of Stresses and Deflections by A. B. Jones, American Society of Mechanical Engineers, and the Hertz contact theory, analyzed the rigidity properties of single-column ball bearings under the combined load of radial and axial forces and moments.

In our country, despite some bearing design documents that provide approximation formulas for calculating bearing deformation, these calculations are limited in accuracy because they ignore the variation of many factors, including contact

angles. Therefore, there is an urgent need to work out a computer program that includes the variation of contact angles and that can compute the deformation and contact stress of differently aligned ball bearings under different loads. With this computer program it will be possible to study the effects of various structural parameters and loads on the rigidity performance of bearings.

## 2. Theoretical Analysis of Deformation of Ball Bearings

Here, we employ the internationally accepted hypothesis: Bearings are stationary and slightly deformed rigid bodies with ideal geometric forms which can tolerate constant loads. In other words,

- a. The deformation is caused by the relative displacement of rigid bodies in the inner and outer rings;
- b. The balls and ball races have correct geometric forms;
- c. The action of inertial force and inertial moment on ball bearings can be omitted and
- d. The acting load remains stationary and unchanged.

For convenience in analysis, we assume that the radial gap  $e_r = 0$ .

### 2.1. Hertz Equations of Deformation

Deformation of ball bearings is computed on the basis of the Hertz theory of point contact. We assume that the contact deformation of balls and inner and outer rings obeys the following formula:

$$\delta_{\text{no}} = K_{\text{no}} Q_{\text{no}}^{1/3} \quad (1)$$

where subscript i stands for inner ring, and subscript o stands for outer ring.

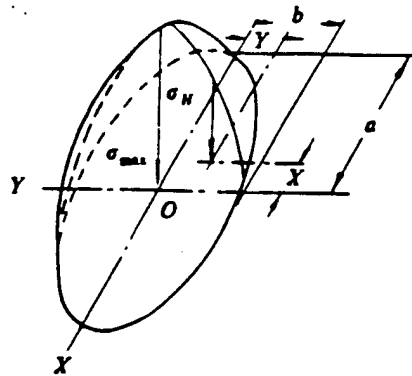


Fig. 1. Distribution of stresses on ellipse contact surface

Upon contact between balls and ball races, a contact ellipse with semimajor axis  $a$  and semiminor axis  $b$  is generated:

$$\begin{cases} a = a \cdot \left[ \frac{3}{2\sum\rho} \left( \frac{1-V_1^2}{E_1} + \frac{1-V_2^2}{E_2} \right) \right]^{1/2} Q^{1/2} \\ b = b \cdot \left[ \frac{3}{2\sum\rho} \left( \frac{1-V_1^2}{E_1} + \frac{1-V_2^2}{E_2} \right) \right]^{1/2} Q^{1/2} \end{cases} \quad (2)$$

where contact area  $A=\pi ab$ ; normal contact stress  $\sigma_H$  is distributed in a semielliptic form in the above-mentioned ellipse contact surface as shown in Fig. 1.

$$\sigma_H = \frac{3Q}{2\pi ab} \sqrt{1 - \frac{X^2}{a^2} - \frac{Y^2}{b^2}} \quad (3)$$

The contact stress reaches its maximum value at the center of the ellipse:

$$\sigma_{\max} = \frac{3Q}{2\pi ab} \quad (4)$$

The contact deformation of balls and ball races is:

$$\delta = \delta \cdot \left[ \frac{3}{2\sum\rho} \left( \frac{1-V_1^2}{E_1} + \frac{1-V_2^2}{E_2} \right) \right]^{2/3} \frac{\sum\rho}{2} Q^{2/3} \quad (5)$$

In Eqs. (2) and (5), coefficients  $a^*$ ,  $b^*$ ,  $\delta^*$  are related to the geometric forms of the contact body alone.

$$a^* = \left(\frac{2c^2 g}{\pi}\right)^{1/3}$$

$$b^* = \left(\frac{2g}{\pi c}\right)^{1/3}$$

$$\delta^* = \frac{2h}{\pi} \left(\frac{\pi}{2c^2 g}\right)^{1/3}$$

The curvature and function:  $\Sigma\rho = \frac{1}{D} (4 - \frac{1}{f} \pm \frac{2\gamma}{1+\gamma})$

where the symbols in the numerator are associated with the inner ring, while those in the denominator--with the outer ring.

The coefficient  $\gamma = D_w \cos \alpha_0 / d_m$

Suppose  $C = a/b$ , then:

$$h = \int_0^{\pi/2} \frac{1}{\sqrt{1 - (1 - 1/c^2) \sin^2 \Phi}} d\Phi \quad \text{is the total elliptic}$$

integration of the first kind.

$$g = \int_0^{\pi/2} \sqrt{1 - (1 - 1/c^2) \sin^2 \Phi} d\Phi \quad \text{is the total elliptic}$$

integration of the second kind.

$c$ ,  $g$ , and  $h$  can be derived from the Hertz theory, which can satisfy the following expressions:

$$\frac{(C^2 + 1)g - 2h}{(C^2 - 1)g} = \frac{-\frac{1}{f} \pm \frac{2\gamma}{1+\gamma}}{4 - \frac{1}{f} \pm \frac{-2\gamma}{1+\gamma}} \quad (6)$$

When balls and sleeve gaskets are made of the same material, the ball bearings can satisfy the following expressions under static load:

$$\begin{cases} E_1 = E_2 = E \\ V_1 = V_2 = V \\ Q_1 = Q_2 = Q \end{cases} \quad (7)$$

From Eqs. (1), (5), and (7), the following can be derived:

$$\begin{cases} K_1 = \delta_1^{[3(1 - V^2)/(E \sum \rho_1)]^{1/3}} \sum \rho_1 / 2 \\ K_2 = \delta_2^{[3(1 - V^2)/(E \sum \rho_2)]^{1/3}} \sum \rho_2 / 2 \end{cases} \quad (8)$$

Since  $\delta_n = \delta_1 + \delta_2$  (9)

then  $Q = K_n \delta_n^{1.5}$  (10)

where  $K_n = [1/(K_1 + K_2)]^{1/3}$  (11)

## 2.2. Geometric Equations of Deformation

In preloaded radial-thrust ball bearings mounted face to face, the inner ring presumably generates a rigid body displacement  $\delta_a$ ,  $\delta_r$  relative to the outer ring (the outer ring is fixed) under the combined action of  $\delta_a$  and  $\delta_r$ , the pre-deformation being  $\delta_0$  as shown in Figs. 2 and 3. For the first column bearings with an increasing axial load ( $m=1$ ), the deformation of balls at the location  $\Phi_1$  is shown in Fig. 4, where  $O_i$  and  $O_o$ , respectively, are the groove curvature centers of the inner and outer sleeve gaskets prior to deformation, while  $O_i'$  is the groove curvature center of the inner sleeve gasket after deformation.

It can be seen from Figs. 2-4 that:

the axial component of deformation is  $\delta_a - (-1)^m \delta_r$ ,  
while its radial component of deformation is

$$\delta_{r,1} = \delta_r \cos \Phi_1$$

Suppose  $\begin{cases} A_0 = O_1 O_0 \\ A = O_1 O_0 \end{cases}$

$$\begin{cases} d_1 = A_0 \sin \alpha_0 - (-1)^J \delta_1 + \delta_0 \\ d_2 = A_0 \cos \alpha_0 + \delta_1 \cos \Phi_0 \end{cases} \quad (12)$$

where  $\Phi_j = \Phi_0 + 2\pi(J-1)/z \quad (J = 1, 2, \dots, Z) \quad (13)$

where  $\Phi_j$  is the location angle of the  $j$ -th ball, the numbering being in the counterclockwise direction;  $\Phi_0$  is defined as the radial displacement angle of the first ball relative to the sleeve gasket.

$$A_0 = (f_r + f_s - 1)D_0 \quad (14)$$

Thus,  $\alpha_0 = \operatorname{tg}^{-1}(d_1 / d_2)$

$$A_0 = \sqrt{d_1^2 + d_2^2}$$

Then, the normal contact deformation between the ball and the inner and outer ball races at location  $\Phi_j$  is

$$\delta_{n\Phi_j} = A_{\Phi_j} - A_0 \quad (15)$$

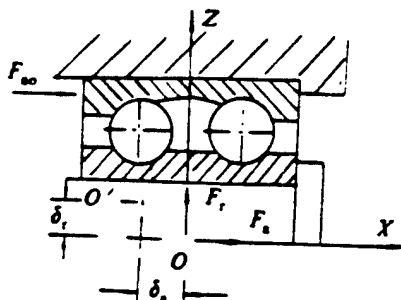


Fig. 2. Schematic map showing force and displacement of preloaded bearing in X0Z plane

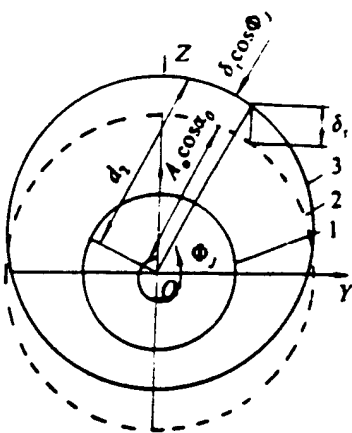


Fig. 3. Schematic map showing location of inner and outer sleeve gaskets in YOZ plane  
 1 - track of groove curvature center of outer ring 2 - track of groove curvature center of inner ring 3 - track of groove curvature center of inner ring with radial displacement  $\delta_r$   
 O - location of supporting axis center prior to deformation O' - location of supporting axis center after deformation

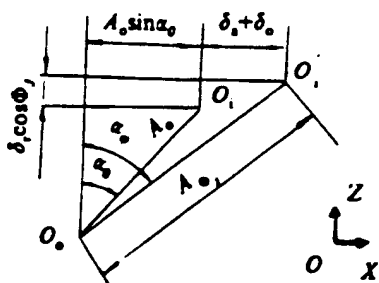


Fig. 4. Relative location of groove curvature center after deformation

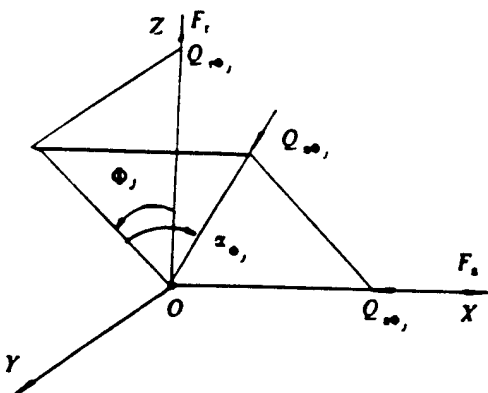


Fig. 5. Schematic map showing the ball at location  $\Phi_j$  under balanced force

### 2.3. Overall Equilibrium Equations of Bearings

From Eqs. (11) and (15), the following can be derived:

$$Q_{n\phi_j} = \begin{cases} K_n \delta_{n\phi_j} & \text{when } \delta_{n\phi_j} > 0 \\ 0 & \text{when } \delta_{n\phi_j} \leq 0 \end{cases} \quad (16)$$

Then its axial and radial components can be calculated from Fig. 5:

$$\begin{aligned} Q_{n\phi_j} &= -(-1)^m Q_{n\phi_j} \sin x_{\phi_j} \\ Q_{n\phi_j} &= Q_{n\phi_j} \cos x_{\phi_j} \cos \phi_j \end{aligned} \quad (17)$$

the overall equilibrium equation of bearings will be:

$$\begin{cases} \sum_{m=1}^2 \sum_{j=1}^2 Q_{n\phi_j} = F_x \\ \sum_{m=1}^2 \sum_{j=1}^2 Q_{n\phi_j} = F_y \end{cases} \quad (18)$$

where  $m=1$  and  $2$ , respectively, are the first column and second column bearings of the bearing pair. Eq. (19) is a nonlinear coupled equation with unknowns  $\delta_a$  and  $\delta_r$ . For the convenience of solution, we assume:

$$\begin{cases} F_x = F_x - \sum_{m=1}^2 \sum_{j=1}^2 Q_{n\phi_j} \\ F_y = F_y - \sum_{m=1}^2 \sum_{j=1}^2 Q_{n\phi_j} \end{cases} \quad (19)$$

$$\text{We define a target function: } F = F_x^2 + F_y^2 \quad (20)$$

It is clear that the minimum point of Eq. (20) is the solution to the coupled equation (18). In this case, the solution to (18) has been converted to the one to the minimum value of function  $F$ . Mathematically, there are quite a number of solutions to the extreme values. Since the target function is a

secondary function that cannot be solved, we employ the Powell optimum method to solve the minimum point of  $F$ .

### 3. Program Design for Deformation of Ball Bearings and Its Calculations

The foregoing analysis of ball bearing deformation theory suggests that generally the deformation and stress of bearings and especially the deformation of preloaded bearings under the action of combined forces cannot be calculated using an explicit function formula. Hence, numerical computation methods based on computers must be applied. We selected the Powell optimum method in consideration of the characteristics of bearing deformation and the established target function.

The process of solving the deformation is as follows:

- a. Given initial values  $\delta_{a0}$  and  $\delta_{r0}$ .
- b. Optimizing these values with the Powell method, i.e., comparing the function values of several randomly selected points and finding out a direction which approaches the optimal point to obtain a new set of  $\delta_{a1}$  and  $\delta_{r1}$ .
- c. Repeating the foregoing process continuously until the target function  $F$  satisfies  $\delta_a$  and  $\delta_r$  with the given precision.

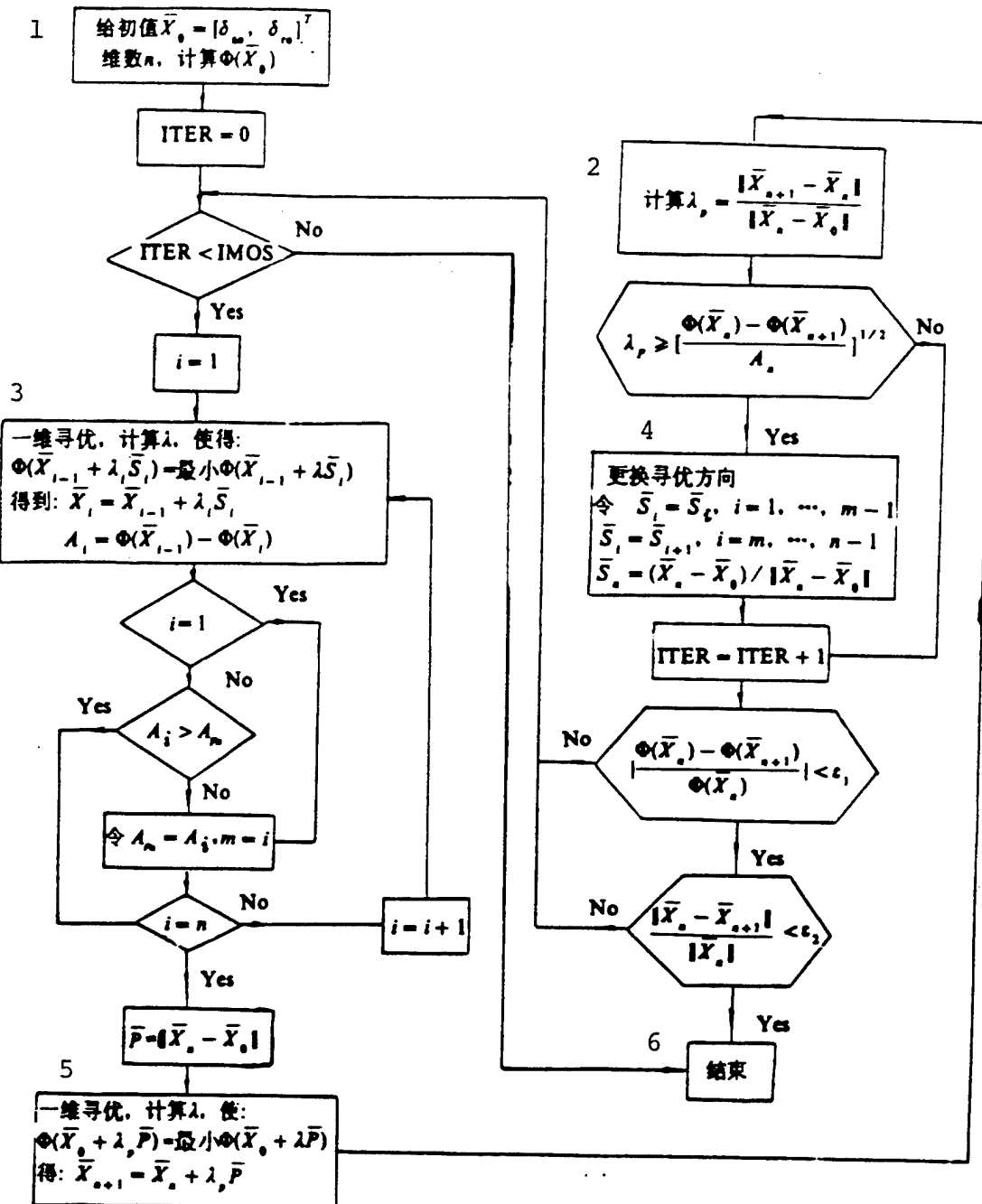


Fig. 6. Block diagram of Powell optimum program  
 $\Phi$  is target function,  $\Phi = F = F^1 + F^2$ , and  $\bar{X}_i$  are the initial values  $\delta_{ao}$  and  $\delta_{ro}$ ; ITER is the control parameter of the iterative function; IMOS is input parameter, the permitted largest number of large cycle inquiries;  $\epsilon_2$  is the input parameter, the computational precision of the variables;  $\epsilon_1$  is the input parameter, the computational precision of the target function.

[KEY to Fig. 6]

1 - Given the initial value [...], number of dimensions n, and computing [...]  
2 - Computing  $\lambda_p = [...]$  3 - One-dimensional optimum inquiry, computing  $\lambda$ , making [...]=minimum [...], obtaining: [...]  
4 - Change inquiry direction [...][...][...]  
5 - One-dimensional optimum inquiry, computing  $\lambda$ , and making: [...], [...]=minimum [...], obtaining [...]  
6 - Terminus

### 3.1. Principle of Powell Optimum Program and Its Block Diagram

Taking the advantage of an approximate conjugation direction for inquiry and judging the approach direction through a direct comparison between function values, the Powell method features rapid convergence, satisfactory reliability, and procedural simplicity.

The basic principle of the Powell method lies in that the isoline of the binary function near the extreme point can be approximately regarded as an ellipse. Two one-dimensional minimum points can be derived along two arbitrary parallel inquiry directions  $\bar{P}_1$  and  $\bar{P}_2$ , through which the straight line connecting  $\bar{x}_1$  and  $\bar{x}_2$  passes. It can be demonstrated mathematically that the inquiry directions  $\bar{P}_1$  (or  $\bar{P}_2$ ) and  $\bar{P}_2$  are relative to the Hanson matrix conjugation, i.e.,  $\bar{P}_1^T A \bar{P}_2 = 0$ . Thus, in optimizing the target function, two different points can be found first, and then one-dimensional inquiry can be made along the same inquiry direction, and the two minimum values derived from the two inquiries can be connected to form the second inquiry direction. Since the function is not an elliptic equation in a strict sense, but an approximate conjugation direction, the inquiry should go on according to this law until convergence.

The block diagram of optimum program is shown in Fig. 6, and its principle is shown in Fig. 7.

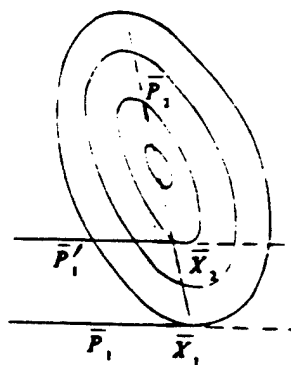


Fig. 7. Schematic map of conjugation direction

### 3.2. Flow Chart of Main Program and Brief Explanations

The flow chart of the main program for calculating deformation and stress is shown in Fig. 8. In the Powell optimum program, the routine used to calculate the quadratic sum and the target function  $F$  has to be fetched repeatedly, its block diagram being shown in Fig. 9.

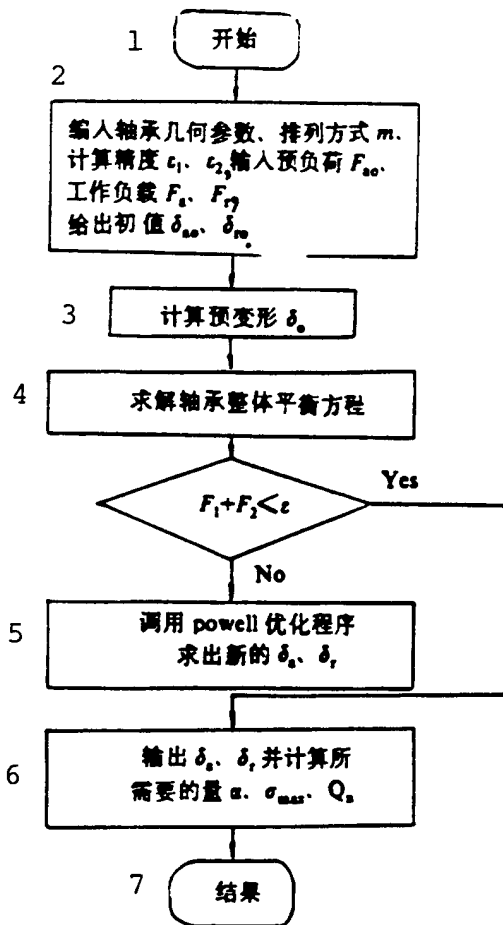


Fig. 8. Schematic flow chart of main program  
 KEY: 1 - Start 2 - Editing geometric parameters  
 of bearings, alignment m, computational  
 precision  $\epsilon_1$  and  $\epsilon_2$ , inputting preload  $F_{ao}$ ,  
 working load  $F_a$  and  $F_r$ , given initial values  
 $\delta_{ao}$  and  $\delta_{ro}$ . 3 - Computing pre-deformation  $\delta_0$ .  
 4 - Solving overall equilibrium equation of  
 bearings 5 - Fetching Powell optimum program  
 to solve for new  $\delta_a$  and  $\delta_r$ . 6 - Outputting  
 $\delta_a$  and  $\delta_r$  and computing desired quantities  
 $\alpha$ ,  $\sigma_{max}$ , and  $Q_n$  7 - Output

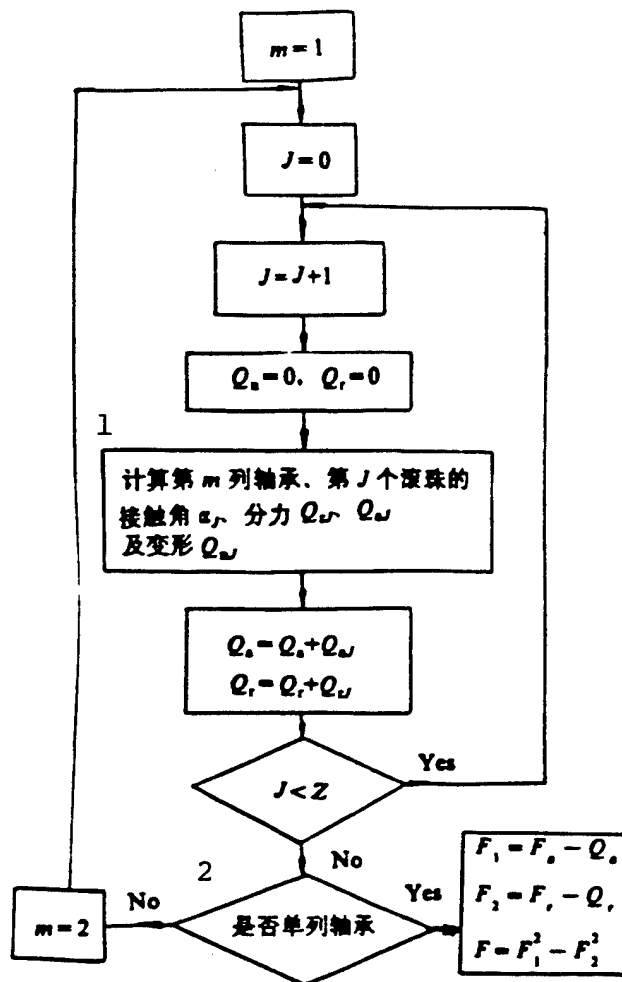


Fig. 9. Block diagram of target function  
 KEY: 1 - Computing contact angle  $\alpha_j$ ,  
 components  $Q_{rj}$  and  $Q_{aj}$  and deformation  
 $Q_{nj}$  of the  $J$ -th ball in the  $m$ -th  
 column bearings 2 - Is it a single-  
 column bearing?

### 3.3. Calculations of Bearings

The calculations of bearings are shown in Tables 1-8.

TABLE 1. Deformation Volume of Single Bearing under Different Preloads Acting in Pure Axial Direction

2 轴向预 载力(N)	1 轴向变形、轴向力 ( $\mu$ m) 3	98	196	294	392	490	588	686	784	882	980
	0	4.2	6.6	8.5	10.2	11.8	13.2	14.5	15.8	16.9	18.0
	98	2.4	4.3	6.0	7.6	9.0	10.3	11.6	12.7	13.8	14.9
	196	1.9	3.6	5.2	6.6	7.9	9.2	10.3	11.4	12.4	13.5

KEY: 1 - axial deformation 2 - axial preload  
3 - axial force

TABLE 2. Relationship between Radial Force and Radial Deformation of Radial-thrust Bearing of the Same Dimension

径向力(N) 1	98	196	294	392	490	588	686	784	882	980	1078	1176	1274	1372	1568
径向变形( $\mu$ m) 2	2.6	4.1	5.3	6.5	7.6	8.5	9.5	10.3	11.2	12.0	12.8	13.5	14.3	15.0	16.4

KEY: 1 - radial force 2 - radial deformation

TABLE 3. Relationship Between Axial Force and Contact Angle  $\alpha$

纯轴向力(N) 1	0	49	92	196	294
接触角(°) 2	24.000	24.867	24.576	24.900	25.162

KEY: 1 - pure axial force 2 - contact angle

TABLE 4. Relationship Between Pure Axial Force  
and Axial Deformation  $\delta_a$  of Single  
Bearing Under Different Contact Angles

轴向变形 2 ( $\mu\text{m}$ ) 接触角(°) 3	98	196	294	392	490	588	686	784	882	980
25	4.4	6.8	8.9	10.6	12.2	13.7	15.1	16.4	17.6	10.8
23	4.9	7.7	10.0	11.9	13.7	15.4	16.9	18.3	19.6	20.9
27	3.9	6.1	7.9	9.6	11.0	12.4	13.6	14.8	15.9	17.0

KEY: 1 - axial deformation 2 - contact angle  
3 - axial force

TABLE 5. Relationship between Radial Force and  
Radial Deformation of a Radial-thrust  
Ball Bearing

纯径向力(N) 1	98	196	294	392	490	588	784	980	1372	1568
径向变形( $\mu\text{m}$ ) 2	2.8	4.5	5.9	7.2	8.3	9.4	11.4	13.2	16.6	18.1

KEY: 1 - pure radial force 2 - radial deformation

TABLE 6. Axial and Radial Deformation of a Single Bearing under Combined Load

径向力 1 $F_r = 196 \text{N}$	轴向力(N) 2	轴向变形 $\delta_a$ ( $\mu\text{m}$ )			
		196	392	490	980
		6.4	10.5	12.1	18.7
		2.2	1.7	1.6	1.3

KEY: 1 - radial force 2 - axial force  
3 - axial deformation 4 - radial deformation

TABLE 7. Relationship Between Pure Axial Force and Axial Deformation of Face-to-Face Mounted ZYS-614 Pair Under Different Preloads

轴向变形( $\mu\text{m}$ ) 径向变形( $\mu\text{m}$ ) 2	轴向力(N) 径向力(N) 5 6	轴向力(N) 径向力(N)			
		1960 / 980	1960 / 1568	2940 / 0	2940 / 1568
轴向 3	0	28.0 / 5.3	27.3 / 8.7	35.9 / 0	35.3 / 7.7
预紧力(N)4	196	21.1 / 5.3	20.7 / 8.5	29.0 / 0	28.5 / 7.7
	294	19.2 / 5.3	19.0 / 8.2	27.0 / 0	26.6 / 7.7
	392	17.5 / 5.2	17.5 / 7.8	25.2 / 0	24.7 / 7.6
	588	15.0 / 4.6	15.2 / 7.0	22.2 / 0	22.0 / 7.2

KEY: 1 - axial deformation 2 - radial deformation  
3 - axial direction 4 - preload 5 - axial force  
6 - radial force

TABLE 8. Deformation of Face-to-Face Mounted Bearing Pairs Under Combined Load

轴向变形 1 ( $\mu\text{m}$ )	纯轴向力 3 (N)	98	196	294	392	490	588	784	882	980	1960	理论拟合曲线与 4 相关系数 $\gamma$
轴向 预紧力(N) 2		4.4	6.8	8.9	10.6	12.2	13.7	16.4	17.6	18.8	28.4	
0												
196		1.1	2.2	3.3	4.4	5.6	6.7	8.9	10.0	11.1	21.5	$\delta_a = 0.166 + 0.011 F_a$ , $\gamma = 0.9997$
294		0.94	1.9	2.8	3.8	4.8	5.7	7.7	8.8	9.8	19.0	$\delta_a = 0.0196 + 9.76 \times 10^{-2} F_a$ , $\gamma = 0.999$

KEY: 1 - axial deformation 2 - axial preload  
3 - pure axial force 4 - theoretical accommodation curves and correlation coefficient

### 3.4. Theoretical Calculations

The foregoing calculations indicate:

- The contact angle is a significant parameter of angular contact ball bearings. The axial rigidity of bearings increases with increase in contact angle, and the contact angle increases with the increase of axial load.
- For radial-thrust ball bearing with  $\alpha_0$  equal to  $25^\circ$ , its radial rigidity is larger than its axial rigidity, and the ratio between the two tends to decrease with the increase of contact angle. While in the ball bearings under a combined load, the ball under the maximum load has a smallest actual contact angle.
- The rigidity of ball bearings is associated with not only the modulus of elasticity of the materials of bearing parts, structural dimension of bearings and geometric accuracy, but the preload as well. Calculations suggest that the rigidity decreases with the increase of the radius of curvature

coefficient of inner and outer grooves, the decrease of the preload and the decrease of the number of balls. Of these factors, the radius of curvature coefficient of grooves has the greatest effect.

#### 4. Deformation Volume Test

To check the reliability of theoretical calculations of ball bearings and to provide technical evidences for ball bearings pair matching, the following points were discussed:

(1) The axial deformation of C46706 and ZYS-614 was tested (the test method is omitted here), the test results being shown in Table 9.

(2) The radial deformation of C706 bearing was tested (the test method is omitted here), the test results being shown in Table 10.

TABLE 9. Axial Deformation Test Results

轴向变形( $\mu\text{m}$ ) 型号 1	纯轴向力(N) 2	98	196	294	392	490	588
c46706-75 <sup>+</sup>		5.0	7.8	11.5	15.2	19.0	21.0
c46706-94 <sup>+</sup>		4.8	7.2	11.0	15.0	19.0	21.0
ZYS-614-48 <sup>+</sup>		6.0	10.3	14.2	17.5	20.5	23.0
ZYS-614-23 <sup>+</sup>		5.8	9.5	14.0	17.0	20.0	22.5

KEY: 1 - axial deformation ( $\mu\text{m}$ ), model  
2 - pure axial force

TABLE 10: Radial Deformation Test Results

径向负荷(N)	1	0	98	196	294	392	490	588	686	784	882	980
径向变形(μm)	2	0	1.8	4.1	6.7	8.1	9.8	11.0	11.8	13.4	14.5	15.5

KEY: 1 - radial load 2 - radial deformation

## 5. Comparative Analysis of Program Calculated Values and Measured Values

A comparative analysis made between Tables 1 and 9, Tables 2 and 10, and Tables 4 and 9 indicates that errors occur in both calculated and measured values of the radial and axial deformation of C46706 as well as the axial deformation of ZYS-614 as shown in Table 10.

### 5.1. Analysis of Theoretical Calculation Errors

The calculations and theoretical accommodation curves show that the relationship between deformation and load of single bearings under the action of one-directional thrust basically conforms to the Hertz theory of point contact and contains accurate physical implications. To simplify calculations, simplifying approaches were taken in the calculating process, which, however, introduced errors in the deformation calculations. The sources of these errors can be summarized as follows:

(1) Calculational assumptions made prior to deformation: such as taking a sleeve gasket as a microscopically rigid body, taking the deformation of balls as a pure result of the displacement of the sleeve gasket line, etc. These assumptions proved to differ from the actual deformation of bearings. In fact, under a large outer load, the sleeve gasket will also deform.

(2) It is also provisional to believe that the contact deformation of balls and sleeve gaskets can satisfy Hertz's theory,  $Q_n = K_n \delta_n^{3/2}$ , such that the materials of tangential objects must be uniform and isotropic; the contact deformation must occur on an extremely small contact surface, the contact stress should not exceed the elastic limitation of materials, etc. In addition, the Hertz theory per se is also an approximate engineering contact theory. When residual deformation is present, the measured values will be larger than the calculated values.

(3) Calculations show that the contact angle has a larger effect on axial deformation. Since the actual contact angle of bearings is smaller than their nominal contact angle, calculating bearing deformation with nominal contact angle ( $25^\circ$ ) is one of the major reasons for the errors in calculated and measured values of axial deformation. According to calculations, if the contact angle decreases by  $2^\circ$  (other conditions being identical), it will produce approximately 15% of the axial deformation error in ZYS-614 bearings.

(4) Since the radial gap of the ball bearings is omitted in calculations, the number of loaded balls in theoretical calculations is larger than the number of actually loaded balls. As a result, the calculated values of radial deformation of the ball bearings will be smaller than its measured values.

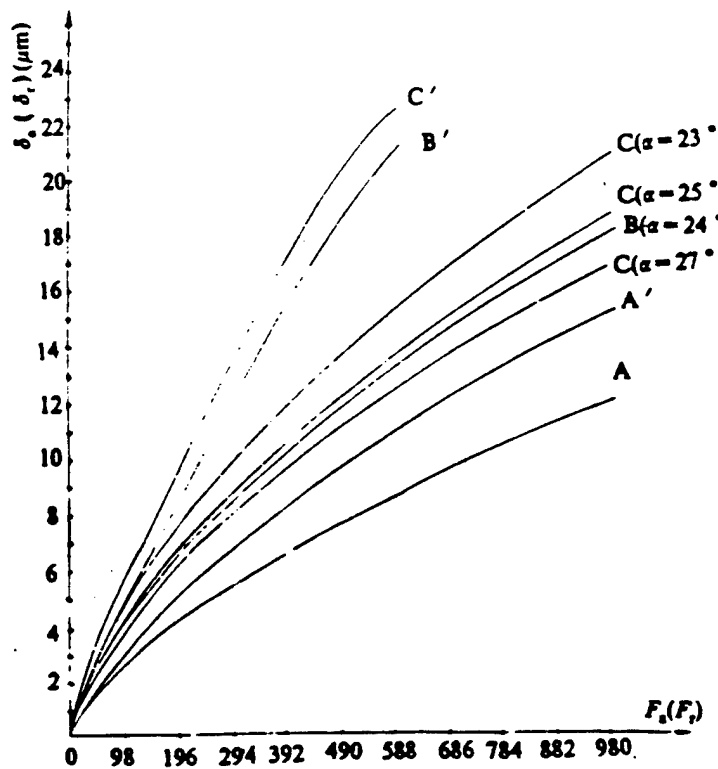


Fig. 10. Comparative curves between calculated values and measured values of axial and radial deformation

A - calculated characteristic curve of C706 radial deformation  
 B - calculated characteristic curve of C46706 axial deformation  
 C - calculated characteristic curve of ZYS-614 axial deformation  
 A' - experimental characteristic curve of C706 radial deformation  
 B' - experimental characteristic curve of C46706 axial deformation  
 C' - experimental characteristic curve of ZYS-614 axial deformation.

## 5.2. Analysis of Test Error Sources

(1) When a force is imposed, the eccentricity of force, the noncoincidence between the induction contact head and the center of the arbor as well as the unevenness of the grounded plane will emerge in combination despite the fact that standard weights have been employed to control the eccentricity, the contact head of the inductance micrometer has been made pointing at the center of

the arbor as much as possible, and the end face of the arbor has been grounded (with an unevenness less than  $3\mu\text{m}$ ). In this case, the measured error is within  $5\mu\text{m}$ .

(2) Prior to the axial deformation test, a preload force should be applied to completely eliminate the effect of the axial play and keep the balls and sleeve gaskets in a desirable contact. However, such a proper force is hard to control accurately. Hence, the measured values of deformation can possibly contain the axial play and become excessively large.

(3) Despite a certain preload imposed prior to the axial deformation test, still, it cannot be confirmed whether or not the contact state of bearings agrees with that during the contact angle test conducted in the Axis Research Institute. Consequently, the errors occurring in the contact angle test will certainly bring errors in the axial deformation test. In addition, the contact angle provided by the Axis Research Institute is also measured using the approximate theory of kinematics and therefore, there will be a difference between its measured values and actual values.

(4) The measured deformation of bearings has a range of  $5\mu\text{m}$ , and the values listed in tables are average values of  $\delta_{\text{lmax}}$  and  $\delta_{\text{lmin}}$ , which will cause a test error no more than  $3\mu\text{m}$ .

### 5.3. Analysis of Errors in Structure Design and Processing Accuracy

(1) Since there is an error between the actual dimension and nominal dimension of various balls (the deviation of ZYS-614 dimension is less than  $15\mu\text{m}$ ), then if  $D_w$ , the actual value, is smaller than its nominal value, the actual deformation will increase. Further, under the action of a certain axial force, not all balls are evenly loaded because their dimensions may not be identical. As a result, the actual number of loaded balls is smaller than the theoretical value, which will make the measured value of deformation larger than its calculated value.

(2) During calculations, the balls and ball races are assumed to have the correct geometric forms in any case, but in fact, the curvature of grooves has a great effect on the rigidity of bearings, and the actual values of  $f_1$  and  $f_0$  are larger than the nominal dimensional values, which will cause the actual value of deformation larger than its calculated value to create a big error. In addition, deviations occurring in the dimension of balls and the geometric forms of grooves, such as undulations, ellipticity, deviation of curvature centers of grooves from geometric centers, etc., will also produce errors in measured values and calculated values.

(3) The comprehensive mechanical performance of materials and particularly, the uneven hardening machining of the contact surface may cause fairly large errors in deformation.

#### 5.4. Demonstration of Feasibility of Program Calculations

Basically, calculations of the FORTRAN program designed to compute the deformation of ball bearings using the Powell optimum method prove to be in agreement with the physical model of bearing deformation. With this program, the calculated values of deformation can be considered to be basically in agreement with its measured values if the following factors could be excluded: measurement errors of contact angle  $\alpha$ , deviation of groove curvatures, deviation of geometric forms and dimensions of balls and radial gaps. Thus, this computing method is believed to be feasible.

By using this program, the deformation and stress of single-column and double-column ball bearings operating under a combined load and maximum overload can be calculated. Beyond this, it can also provide the means for analyzing the effects of different structural parameters and loads on the rigidity of bearings as

well as provide fundamental theoretical evidence for bearing model selection and verification.

#### REFERENCES

1. Harris, T. A., Rolling Bearing Analysis, 1984.
2. "SKF. Preloading pinion bearing," The Ball Bearing Journal, 1964(139).
3. Qing Shoukang, Optimum Theory and Method, Electronic Industry Publishing House, 1986.
4. Theory, Design and Test Techniques of Gyroscopes, Defense Industry Publishing House, 1978.

This paper was received on June 5, 1994.

## PLATFORM GIMBAL DESIGN AND MACHINING TECHNOLOGY

Liu Yiwei and Chen Xiaozhong

Beijing Institute of Control Devices

**Abstract:** The platform gimbal is a key part of a stabilized platform and its machining technology is the key technology of inertial manufacturing technology. Because of the limits on dimensions and weight of the platform structure, the platform gimbal must be a thin shell part. Because of its large size and complicated shape during the flight environment (overload, vibration, impact, etc.), it is necessary to insure high precision, strength and rigidity in order to avoid the effects on the positional accuracy of the stable member. This makes designing and machining very difficult. In view of the difficulties in platform gimbal design, manufacturing, and flight environment testing, the measures of ribs, variable cross-section, and E-shape forging aluminum structure forms of platform gimbal were adopted. In this technology, new fixtures were built to improve the method of adjusting the machine tools and the alignment scheme so that conventional machine tools may produce high-precision and qualified products. It has been shown in routine and flight tests that the measures adopted are correct.

**KEY WORDS:** Inertial platform, aerospace processing, design.

## 1. Introduction

A platform gimbal is designed to support the platform body through the shaft-end components as shown in Fig 1.

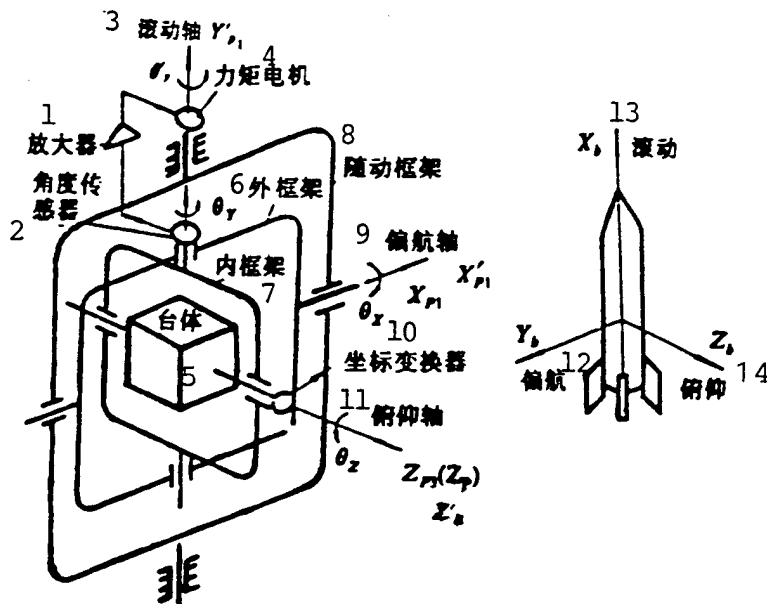


Fig. 1. Schematic map of three-gimbal four-axis gyro-stabilized platform

- 1 - amplifier 2 - angle sensor 3 - roll axis
- 4 - torque motor 5 - platform body 6 - external gimbal
- 7 - internal gimbal 8 - follow-up gimbal
- 9 - off-course axis 10 - coordinate converter
- 11 - pitch axis 12 - off course 13 - roll
- 14 - pitch

The internal gimbal, along with its bearings, is used to support the total weight of the platform, while the external gimbal, along with its bearings, is used to support the total weight of the components of the internal gimbal. Similarly, the bearings are used to support the total weight of the components of the follow-up gimbal on the foundation, i.e., the platform body supported by the platform gimbal system serves as a stable object of the gyro-stabilized platform system.

The gyroscopes installed on the platform body are sensitive to the angular displacement or angular velocity of the platform body relative to inertial space, and they function in stabilizing the platform in inertial space through a stable servo control system. Therefore, the coordinate system set up for the platform body is an inertial coordinate system.

The gimbal system provides three rotational degrees of freedom for the platform so that the platform can be isolated from the angular motion of a missile (rocket) body, and the inertial instruments on the platform can operate under satisfactory conditions. Since this platform is categorized as a small-scale high precision platform whose entire spatial dimensions are limited to a volume of  $0.03m^3$ , on the one hand, and to a weight of 25kg, on the other. Thus, these three gimbal rings are required to be compact in structure.

For normal operation of the gimbal support system in a flight environment (overload, vibration, impact, and the like), i.e., for accurate positioning of the platform and a minimum offset of the platform centroid, the dimensional and configuration allowance of the platform gimbal can directly affect the performance of the shaft-end components and the platform.

As a thin-shell part, the platform gimbal is required to be large in configuration dimensions, complicated in shape, and light in weight; it is also required to have a sufficient rigidity and symmetry, together with requirements for precise matching dimensional and strict configuration allowance, which causes tremendous difficulties in the design and machining of the platform gimbal.

A great deal of experimentation on the rigidity of the

platform gimbal shows that the rigidity of the internal gimbal in the  $Y_k$  direction and that of external gimbal in the  $X_k$  direction is found to be a bit weak and that of the follow-up gimbal in the  $Y'_k$  direction is weaker as well.

During system designing, to satisfy the dimensional requirement of the overall structure of the platform and its support system, to meet the requirements of equal rigidity and good technology based on a bearing analysis, and to overcome the shortcoming in that overly large dimensions of the platform gimbal may cause a weaker rigidity and severe deformation during machining, we adopted the measures of ribs, variable cross-section, and E-shape forging aluminum structure. Also, we took approaches such as increasing the coplanarity of the positioning surfaces and satisfying the requirements of the gimbal machining fixtures. As a result, the overall rigidity was strengthened without affecting the overall spatial dimensions, and eventually, some problems arising during the platform gimbal rigidity experiments and processing were solved, and this technology gained a significant improvement.

Moreover, during the production period, the fixtures are apt to deform because the platform gimbal is a thin-shell, light and complex component. Hence, it is difficult to control the dimensional and configuration allowances during machining. In fact, spare parts of its kind still have to be machined with conventional machine tools, which has proved to be challenging. To cope with this obstacle, we proposed both efficient and applicable solutions such as newly designed fixtures, adjustment methods for improving the machine tools, as well as a machining alignment scheme, etc. With the implementation of the foregoing technological improvements, the stability and reliability of the platform gimbal machining performance were substantially improved, and the high precision and complicated thin shell

components can be produced on conventional machine tools.

With all these approaches, the rationalization of the design was confirmed, and on the other hand, the technical difficulties in technology were overcome, contributing to the manufacturing technology of inertial devices.

## 2. Structural Features and Technological Requirements of Platform Gimbal

### 2.1 Structural Features

(1) There are two pairs of holes on the platform gimbal, of which one pair of large holes on axis I-I are used to mount the stator base of the shaft-end components; the pair of small holes on axis II-II are used to install the rotor base of the shaft-end components; and these two pairs of holes are mutually orthogonal. Also, the three gimbals of the platform are the same in their basic structure except for the difference in their configuration dimensions. The structure of the follow-up gimbal is shown in Fig. 2.

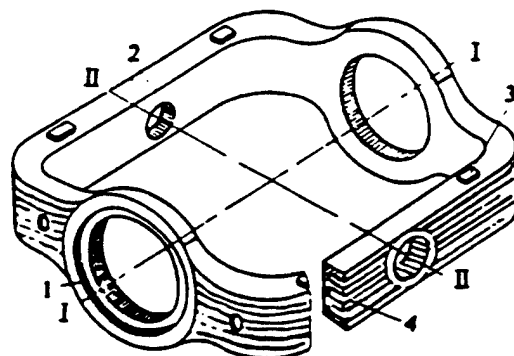


Fig. 2. Structure of follow-up gimbal

(2) The open gimbal structure was adopted, which can be used to achieve instrument interchanges, accuracy adjustment as well as platform maintainability.

(3) The platform is the base of the missile body inertial coordinates. For the platform gimbals to support the platform, the gimbals are required to possess enough rigidity as well as a symmetrical structure to eliminate and reduce unequal elastic interference moments of force.

(4) The shaft-end components are installed at the two ends of the platform gimbal. In this case, there are stringent requirements for matching dimensional and configuration allowances, which otherwise will directly affect the performance of the shaft-end components. Likewise, the normal operation of the shaft-end components must be assured in the platform gimbal system (overload, vibration, impact, etc.) in a flight environment. The strength and rigidity of the platform gimbals must be high enough to reduce the elastic deformation of overload conditions so that the structural line deformation of the platform gimbals under a force of 5g is no greater than 0.15mm.

(5) When in service and when in stowage, the platform must retain stable precision. To be tested in a comprehensive environmental experiment, the precision and stability requirements of the platform gimbals are highly demanding.

## 2.2 Technological Requirement

(1) Rigidity in the  $X_k$ ,  $Y_k$ ,  $Z_k$  directions should not exceed  $0.015\text{mm/g}_0$ ;

(2) Perpendicularity of end face and installation hole should not exceed  $0.005\text{mm}$  with roughness no greater than  $0.4\mu\text{m}$ ;

(3) Coplanarity in the four positioning surfaces should not exceed 0.004mm;

(4) Coaxiality of the axial lines in the installation holes from two sets of shaft-end components should not exceed 0.01mm. And the parallelity of two axial lines relative to the positioning surfaces should not be over 0.012mm;

(5) Perpendicularity of the axial lines in the installation holes from two adjacent shaft-end components should not exceed 0.01mm (the outer ring of the gimbal should not be over 0.015mm);

(6) The allowance of the length dimension should be strictly designed to comply with the IT6 standard. And the allowance of the two pairs of holes is required to reach the IT5 standard.

### 3. Structural Forms of Platform Gimbal and Selection of Materials

The platform gimbal serves as a principal element in the platform. It supports the platform through shaft-end components. The gimbal system can be isolated from the angular motion of a missile body to ultimately make the platform stable in the inertial space.

#### 3.1. Structural Forms of Platform Gimbal

The platform gimbal as a bearing element in supporting the platform can be divided into two categories structurally: frame gimbal and spherical gimbal, of which the latter is believed to have a better bearing capacity. However, the inertial instruments on the platform must be precisely adjusted and interchanged as required. It is cumbersome for the instruments with a closed structure to go through the interchange. Therefore, the four-axis platform gimbal is designed with a thin-shell gimbal structure--a gimbal with ribs, variable cross-section, and E-shape structure.

Fig. 3 compares several different gimbal models applied both domestically and abroad. Gimbal model A adopts forging aluminum alloy LY12 with an open, lightweight and easily routed structure. Models B and C adopt casting aluminum alloy LY111 with a large spatial volume; of these, model C is easy to be routed, but model B is not. Finally, model D is an American II civilian-oriented cross-sectional structure.

1 框架形式	薄壁加筋环形	空心环形3	4 薄壁环形	5 空心环形
横截面形式	2			
	A	B	C	D

Fig. 3. Comparison among different gimbal models  
 KEY: 1 - gimbal forms, cross-sectional form  
 2 - thin shell rib ring 3 - hollow ring  
 4 - thin shell ring 5 - hollow ring

### 3.2. Selection of Material for Platform Gimbal

Generally speaking, the beryllium alloy and the aluminum alloy make a suitable material for platform gimbal; of these the beryllium alloy has a better performance. However, since the beryllium alloy costs more and its technological conditions are limited at present, we tend to select the forging aluminum and casting aluminum alloys as materials for the gimbal structure.

Compared with the casting aluminum alloy, the forging aluminum alloy has a higher rigidity ratio and strength ratio and has good mechanical performance. Thus, we chose the forging aluminum LY12 with higher "elastic module/density ratio and yield strength/density ratio" for our platform gimbal.

Although the casting aluminum platform gimbal needs less machining, we still selected the forging aluminum because its

crystalline structure is stable so that it can avoid some defects, including thermal stress, blowholes, looseness, and sand holes, which may affect the quality of the gimbal and even cause the gimbal to break down, affecting platform stability. In any case, compared with the casting aluminum AL201 chosen for other gimbal models in China, we are proud to say that the forging aluminum we chose has obvious superiority.

#### 4. Problems in Manufacturing and Routine Tests of Platform Gimbal and Improvement Measures

##### 4.1. Problems of Platform Gimbal

With its large configuration dimensions, complex structure, thinness, and easy deformability, the platform gimbal is difficult to machine. If the fixture is machined improperly, the mass-produced items may become useless because of dimensional errors. Obviously, this can lead to great economic losses. Hence, no matter whether the parts are machined on conventional machine tools or in a transfer center, the numerous problems mentioned above should be solved.

(1) The fixture of the platform gimbal was found to be greatly deformed during machining, or the parts were observed to wobble during machining.

(2) The platform gimbal satisfied the allowance requirements while located on the machine tools during machining. But when they were removed from the machine tools, the dimension allowances change greatly, revealing poor stability.

(3) The rigidity of the platform gimbal and the rigidity of the follow-up gimbal in the  $X_p$  direction were found to be weaker during the overload rigidity test.

#### 4.2. Improvements in Platform Gimbal Design

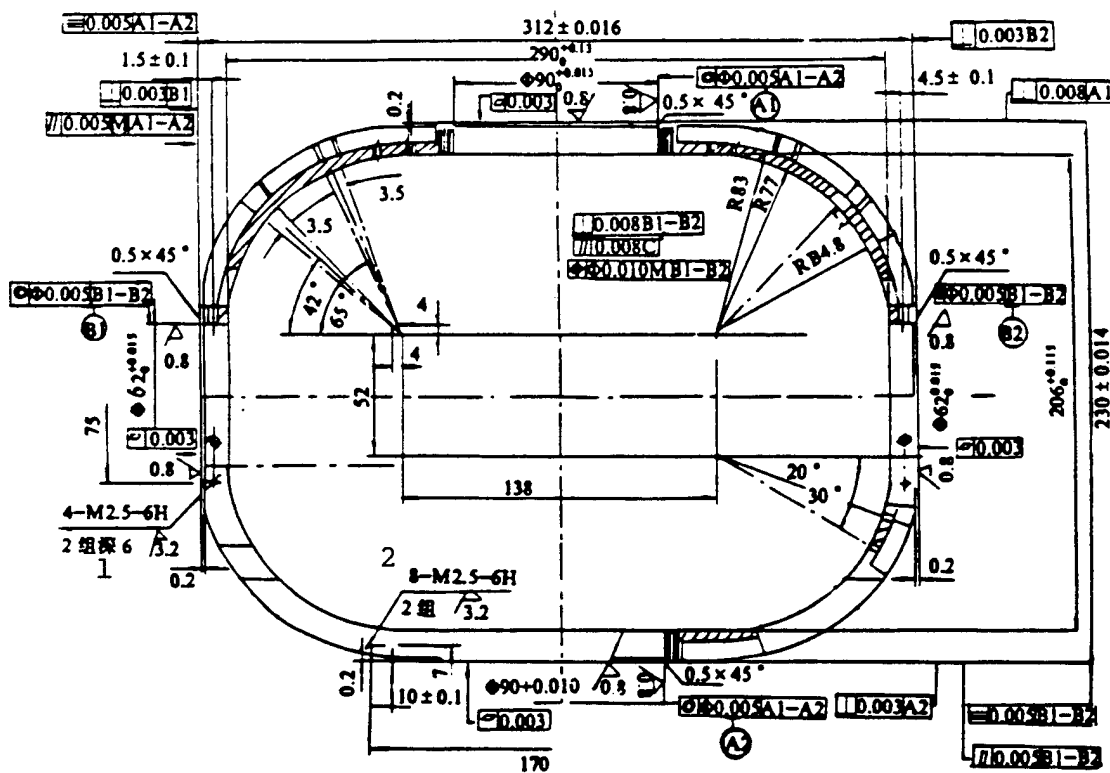


Fig. 4. Follow-up ring diagram  
KEY: 1 - Two sets 2 - Two sets

The above-mentioned problems in designing the platform gimbal are expected to be solved provided that the overall spatial dimensions of the platform and the structural scheme remain unchanged. In addition, the stability and reliability of the platform system should be assured, which is held to be a crucial point in the system design.

To overcome this hurdle, the major point is to ensure the strength and rigidity of the platform gimbal through ribs and variable cross-section form in the radial and axial directions so that the requirement of rigidity under the overload condition could be met, the machining technology could be upgraded and the

requirements of rigidity and strength during the flight could be satisfied. The major improvements should be made in following aspects:

(1) The ribs should be added near the positioning surface (four ribs should be added to the internal and external gimbals, and eight to the follow-up gimbal). As a result, the overall rigidity can be strengthened and the fixture deformation and part wobbling during machining can be solved.

(2) The variable cross-section should be adopted to strengthen the rigidity in the direction where the rigidity is weaker without changing the platform gimbal structure form.

(3) The coplanarity precision in the four positioning surfaces should be enhanced to reduce deformation in the fixture and improve machining stability.

The improvements can be seen in the circle shown in Fig. 4 of the follow-up ring diagram.

Experimental results indicated that the design of platform gimbal can meet the overall precision requirements of the platform, and the design is quite logical. Clearly, the technology proved to be much more efficient after the improvements were made and the problems previously existed in the design were actually literally solved.

#### 4.3. Improvements in Machining Technology Applied in Machining the Platform Gimbal

Application of the platform gimbal machining technology appeared to be very difficult and there were some problems occurring during the machining. We analyzed the causes of the platform gimbal defects in attempting to discover the source of the defects. Eventually, we found the problems to lie in the machining technology. Then we found a practical and reliable

technology solution based on the structural features of the parts.

#### 4.3.1. Improvements in Fixtures

The platform gimbal showed obvious deformation during the mounting of the manufacturer-designed fixtures and the positioning linkage fixtures. Specifically, the axial lines of the two holes showed displacements and strangely, the dimensional and configuration allowances of the platform gimbal met the requirement of machining on the machine tool, but somehow deformed when they were taken off the machine tool.

The newly-designed fixture adopted a point contact form. It was tightly clamped on the ribs of the platform gimbal with a holding board so that the platform was under an even and stable force. During the tightening process, a dial gauge can be used to monitor the process so that the platform gimbal deformation can be reduced to the minimum, and the stability of machining precision can be ensured. The new fixture is not a linkage holding device, and it can isolate the fixity from positioning so as to eliminate fixity error.

#### 4.3.2. Machine Tool Adjustment Method

During the previous operation, the center of the rotary table was made to coincide with the center line of the principal axis, and the graduations were made with the scale of the rotary table. However, since the errors in the rotary table graduations were reflected many times on the configurational shape allowance of coaxiality and symmetry of the pairs of holes, these indexes always overshot the limits.

Through improvements, the center of the rotary table and the center of the principal axis can be adjusted to within 0.001mm,

and these adjustments are repeated during the fine machining. Moreover, a high-precision tetrahedral meter was used as the graduation standard for revolutions, and the photoelectric collimator was employed for alignment to enhance the revolution precision of the rotary table. Eventually, the coaxiality of the two holes and the verticality of two axial lines, as well as the symmetry of the platform gimbal were all able to meet the requirements specified on the blueprints.

#### 4.3.3. Adjustments of Cutting Tool

Originally, the end face on the platform gimbal became either convex or concave from time to time, and the verticality between the end face and holes always exceeded the limits. Additionally, the clamping chuck of the boring cutter was found to be a problem, i.e., the cutting angle of the cutting tool was improper. This was improved after appropriate measures.

#### 4.3.4. Technology Arrangement

Two stable machining procedures were added. As required, one fine forging procedure was added. In particular, liquid nitrogen stable machining was introduced prior to the fine machining, which showed good results and increased the stability of the material.

Beginning with semi-fine machining, a limited amount of cutting was adopted, which prevented deformation caused by excessive cutting.

Arrangements were made for the hole machining order, i.e., the thread hole was machined first, followed by the face-to-face bore hole machining.

The comparison between the platform gimbal precision before

and after the improvements can be seen in Fig. 1.

## 5. Conclusion

Through the above-described measures, the problems of the platform gimbal were solved, as confirmed by manufacturing practice, routine tests, as well as by flight carrier tests. This shows that our improvements were found to be efficient and well organized. Incorporated with the manufacturing practice, an applicable technology scheme was finally developed, to satisfy the overall precision requirements of the platform gimbal.

The parts of the thin-shell platform gimbal attained the 100% standard on conventional machine tools, which ensures the cost-effective operations in the plant. Also, the short supply of wires during production was solved, and the overall progress schedule of the platform manufacture can be guaranteed.

The new technology scheme overcame the technical obstacles and is accredited as a remarkable technological breakthrough, which will stimulate the development of inertial device manufacturing technology and provide a successful example for the development of similar products.

TABLE 1. Comparison of Platform Gimbal Precision  
Before and After Improvements

Detection items	Comparison detection	Before improvements	After improvements
Φ90 hole coaxiality 0.01		0.063	0.005
Verticality of Φ90 hole axial line and Φ62 hole axial line 0.015		0.053	0.0025
Parallelity of Φ90 end face and Φ62 hole axial line 0.01		0.07	0.002
Parallelity of Φ62 end face and Φ90 hole axial line 0.01		0.024	0.004
Verticality of Φ90 end face and C face 0.005		0.005	0.008
Verticality of Φ62 end face and C face 0.005		0.005	0.001
Symmetry of Φ62 end face and Φ90 hole 0.02			0.01
Symmetry of Φ90 end face and Φ62 hole 0.02			0.02
Verticality of Φ62 end face and its axial line 0.005		0.005	0.008
Verticality of Φ90 end face and its axial line 0.005		0.005	0.003
Φ62 hole dimension $\Phi 62^{+0.010}$		Φ62.008	Φ62.003
Φ90 hole dimension $\Phi 90^{+0.022}$		Φ89.973	Φ90.004

<u>Detection items</u>	<u>Comparison detection</u>	<u>Before improvements</u>	<u>After improvements</u>
312 dimension 312 <sub>0.032</sub>		312.1	311.87
230 dimension 230 <sub>-0.029</sub>		229.77	229.085
Coplanarity of four raised faces 0.004		0.004	0.002

Acknowledgement: We would like to hereby acknowledge all designers, technologists, and other related staff members for their dedicated cooperation and support.

#### REFERENCES

1. Editor, W. G., Inertial Component Testing: Philosophy and Methods, printed and published by Technivision Services, Slough, England. 1970, p. 7.
2. Wu Minjin et al., Inertial Device Manufacturing Technology, Astronautics Publishing House, 1989, p. 3.
3. Lu Yunjou et al. Inertial Devices, Astronautics Publishing House, 1993. p. 11.

This paper was received on March 12, 1995.

# DESIGN STUDY OF RADAR ABSORBENT MATERIAL COMPOSITES

Zhang Lizhong

Beijing Institute of Materials & Technology

**ABSTRACT:** Research progress of designing radar-absorbent material composites (RAM composites) over a wide band is introduced. The methods of designing radar-absorbent structure (RAS) and the design results of thin RAM composites and hybrid RAM composites are stressed.

**KEY WORDS:** stealth material, structural materials, broadband.

## 1. Introduction

Structural wave-absorbent material and wave-absorbent coating material combined are referred to as stealth material or radar-absorbent material (RAM). Compared with radar-absorbent coating material, the structural radar-absorbent material not only can effectively absorb radar waves, but also is a sophisticated composite material which can be directly used to make aircraft structural members. Practically speaking, structural radar-absorbent material has already been considered as a leading direction in the development of contemporary stealth material[1].

While applied in constituting structural members, structural radar-absorbent material is not restricted by thickness as is radar-absorbent coating material, and allows a certain flexibility in designing the electrical structure of the material. Theoretically, it can more easily solve the broadband absorption problem[2].

However, to meet the required load-bearing capacity of the structure, designers have to consider the composition of the bearing components in the material structure, yet the load-bearing components usually do not have the wave-absorbing function and thereby can restrict the design of the composition of wave absorbing components. Hence, in designing the structure of structural radar-absorbent material, it is necessary to satisfy both the requirements of wave absorption performance and requirements of mechanical performance, which is extremely difficult and complex.

In terms of the structure of material, structural radar-absorbent material can be roughly divided into two types: thin structural radar-absorbent material and sandwich structural radar-absorbent material[4]. The absorption mechanism of thin structural radar-absorbent material is medium loss, while the absorption of the sandwich material, which is greater in thickness, is based on the harmonic oscillation mechanism. Comparatively speaking, the former possesses a higher strength, while the latter can more easily realize broadband absorption. The design of broadband radar absorbing structure basically focuses on these two structural materials.

The power reflection coefficient  $R$  (measured in dB) is generally accepted as the criterion for the absorption performance of material. Apart from the thickness of material,  $R$  is mainly determined by the electromagnetic parameters (dielectric constant and permeability) of material[5]. In

contrast, the thickness and electromagnetic parameters are just the core elements in the design of broadband radar-absorbent material.

Based on years of design practice, this paper attempts to depict an overall picture of the achievements achieved in designing the broadband radar-absorbent structure of structural radar-absorbent material.

## 2. Methods of Designing Radar-absorbent Structure of Material

Radar-absorbent structure refers to the electromagnetic parameter structure of material, which absorbs radar waves, whereas absorbent material with a lamellar structure refers to the composition of the electromagnetic parameters of each layer and the thickness of material. According to the theory of the transmission lines of electromagnetic waves in media, mathematical models of radar-absorbent structure and radar absorption performance can be built.

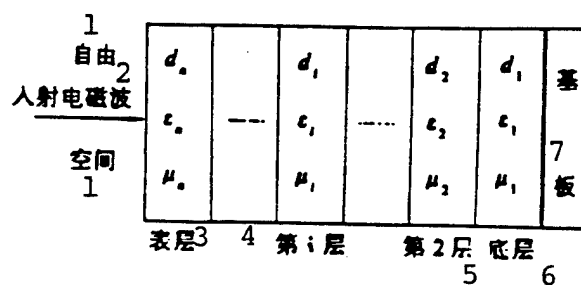


Fig. 1. Schematic map showing incidence of electromagnetic waves in multilayer radar-absorbent material

KEY: 1 - free space 2 - incident electromagnetic wave 3 - surface layer 4 - i-th layer  
5 - second layer 6 - bottom layer  
7 - floor

As shown in Fig. 1, we assume that an electromagnetic beam vertically transmits from free space into an radar-absorbent material with a multilayer structure. On the interface between

the free space and the material, the reflectivity of the electromagnetic wave  $R$  can be expressed as:

$$R = 20 \lg |\Gamma|$$

$$\Gamma = \frac{Z_s - 1}{Z_s + 1} \quad Z_s = \eta_s \frac{Z_{i-1} + \eta_i \operatorname{th}(iK_0 d_i n_i)}{Z_{i-1} \operatorname{th}(iK_0 d_i n_i) + \eta_i}$$

where  $Z_i$  is input impedance of the  $i$ -th layer  $\eta_i = \sqrt{\mu_{ri}/\epsilon_{ri}}$   
 $\eta_i$  is intrinsic impedance,  $(r$  is normalization)  
 $n_i$  is the index of refraction  $n_i = \sqrt{\epsilon_{ri}\mu_{ri}}$ ;  
 $K_0$  is number of waves in free space  
 $\epsilon_0$  is dielectric constant of free space  
 $\mu_0$  is permeability in free space  
 $d_i$  is thickness of material (mm)  
 $f$  is frequency (GHz)  
 $\epsilon_{ri}$  is composite dielectric constant  $\epsilon_{ri} = \epsilon_r - \epsilon_s$ ;  
 $\mu_{ri}$  is composite permeability  $\mu_{ri} = \mu_r - \mu_s$ .

The above formula indicates that the electromagnetic parameters and thickness of each layer of material are related to the radar absorption performance  $R$ . Thus, the optimum parameters of the radar-absorbent structure of the material can be designed based on the requirements of reflectivity  $R$ . Obviously, such kind of optimum design can be realized only with computer software.

The basic design method signifies that the optimized initial conditions and the result of the design are both imaginary parameters. In our country, this method is basically used to design the structural radar-absorbent material[2,5,6]. At present, the related software, with complete functions, can optimize the electromagnetic parameters, thickness, and number of layers of the material simultaneously or individually under different angles of incidence of electromagnetic waves.

A remarkable shortcoming of the basic design method (i.e., the first-generation computer-assisted design) lies in the fact that the design can only be conducted in a presumptive range of electromagnetic parameters, and the designed material parameter schemes can hardly be all realized. Therefore, such a method can only be used for performance pre-estimation and research guidance.

It is to be noted that the design of structural radar-absorbent material must be based on the parameter scheme that can be realized. Here, we introduce the following two approaches which are helpful in achieving this goal.

## 2.2. Fully Automatic Optimum Design Technique

Taking advantage of the tested electromagnetic parameters of the structural radar-absorbent material, the fully automatic optimum design technique is intended for creating various combinations of impedance structure and thickness to achieve an optimum design. This design method relies on the database of the electromagnetic parameters of the existing materials; the greater the volume of data, the more easily the designed material can satisfy the requirements. In addition, the fetching of data and combination of data must proceed automatically with the aid of a computer. There are two reasons for this: first, a large volume of data will produce numerous combinations, too many to be accomplished by manpower; secondly, subjectiveness and blindness in artificial selection of material can be diminished. Fig. 2 is a flow chart of this design method.

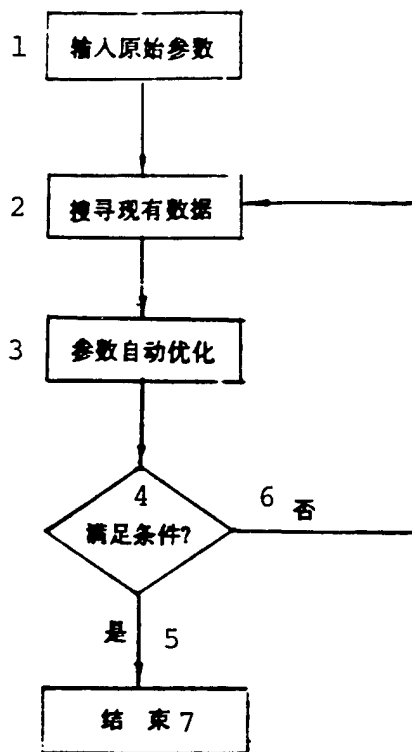


Fig. 2. Schematic flow chart of fully automatic optimum design

KEY: 1 - original parameter input 2 - existing data search 3 - automatic parameter optimization 4 - are conditions satisfied?  
 5 - yes 6 - no 7 - the end

At present, this method has been well developed to exhibit the capabilities of automatically designing all angles and all parameters. It was with this method that the author of this paper designed and successfully developed a structural radar-absorbent material with  $R$  less than  $-20\text{dB}$  in the broadband range. Actual measurements show that this method can effectively guide technological research into broadband structural radar-absorbent material.

### 2.3. Optimum Design of Microscopic Structure and Composition

The second design method based on existing material parameters is often referred to as second-generation computer-assisted design. Electromagnetic parameters are properties of material, which can not only determine the absorption performance of material, but also reflect its microscopic structure and composition. It is with the tested electromagnetic parameters of the existing fundamental components and their combination laws that this method can perform an optimum design of material composition and thickness. Unfortunately, there has been no report on research done in designing the microscopic structure and composition of structural radar-absorbent material in our country.

Generally speaking, the major factors that affect the composition and microscopic structure of the absorption performance of structural radar-absorbent material include the following: types and content of the fundamental components of material (such as fiber, resin, and absorbent), various forms of components (grain size and orientation) and the modes of reinforced fibers, etc. Since the types and orientation of resin and fiber are part of the design of the mechanical structure of structural radar-absorbent material, the design of its microscopic structure and composition is not pure design of the radar-absorbing structure of material, but combined design of both mechanical structure and absorption structure of material, i.e., an integrated optimum design of the structural radar-absorbent material, which is entirely different from and more complex than the design of the radar-absorbent coating material.

### 2.4. Analytical Techniques of Radar-absorbent Material with Multilayer Structure

Radar-absorbent material with a multilayer structure is

superior to the one with single-layer structure in terms of absorption performance. The reason for this is generally believed to be the fact that multilayer material is more easily matched with free-space impedance[7-9]. The radar-absorbing properties of multilayer material can be analyzed and interpreted using a multilayer medium equivalent method. Specifically, multilayer material can be regarded as being equivalent to one layer of a single medium. The electromagnetic parameters of the equivalent medium can be calculated from the electromagnetic parameters and thickness of each layer of material, and based on this, the equivalent impedance and reflectivity of material can further be calculated.

Originally, the multilayer medium equivalent method was used for the slotted-line measurement of the electromagnetic parameters of material[9]. In recent years, however, Xiangyuan Wang from Nanjing University was the first to use this method in analyzing the absorption performance of radar-absorbent coating material, and the calculations proved agree closely with the results of the conventional transmission line iterative method. Yet no report was ever filed on this kind of research on structural radar-absorbent material.

This paper applied the foregoing method in analyzing radar-absorbent material with multilayer structure.

### 3. Design Study of Thin and Hybrid Structural Radar-absorbent Materials

#### 3.1. Design Study of Thin Structural Radar-absorbent Material

It is extremely difficult to widen the radar absorption band of thin structural radar-absorbent material, because this kind of material is required to be thin. To overcome this difficulty, researchers in our country conducted in-depth studies and obtained satisfactory results. Reference 6 introduces a thin

structural radar-absorbent material with  $R$  less than -10dB on a local waveband. This material, only 3.1mm thick, has a single-peak absorption character. Another thin structural radar-absorbent material with  $R$  less than -10dB on two local waveband is presented in reference 10, which, 5-7mm thick, has a two-peak absorption character. Both these materials were designed by using the basic design method.

For the thin structural radar-absorbent material, the best broadband absorption characteristics should involve a broad absorption frequency band, two-peak or multi-peak absorption, low reflectivity and small thickness of material. To achieve this, we studied this material more intensively, with the fully automatic design method and acquired satisfactory results.

The absorption performance of the thin structural radar-absorbent material results from electromagnetic losses. Nevertheless, material with greater losses tends to have its intrinsic impedance closer to that of a metal, which may cause a strong reflection on the front surface and affect its broadband absorption performance. To solve this problem, a better approach is to adopt a gradual impedance structure, which produces less reflection.

It was found out through studies that the thin structural radar-absorbent material should be basically composed of three layers. Since the magnetic loss and electrical loss generate effective absorption, respectively, at the low-frequency end and high-frequency end of the absorption band, there must be two kinds of losses contained in the composition of the selected material parameters. Due to the restriction of thickness, the surface layer of the material is required to provide not only impedance transformation, but also energy absorption, to a certain extent. Hence, a higher-impedance material with a certain loss was selected as the surface layer.

The thin structural radar-absorbent material designed in this paper features a two-peak absorption character, its frequency band with absorption performance  $R$  less than  $-10\text{dB}$  being even broader, while the thickness of the material is only 3.1mm. The typical  $R(\text{dB}) \sim F(\text{GHz})$  curves are shown in Figs. 3-5.

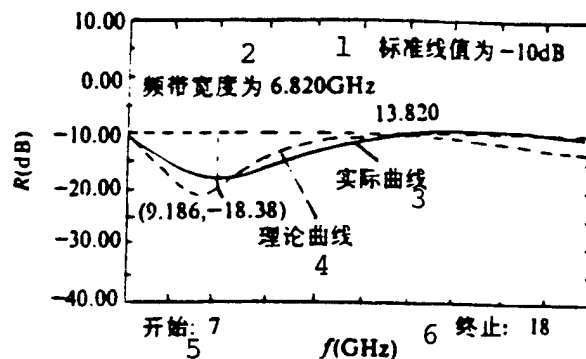


Fig. 3. Absorption performance curve of thin structural radar-absorbent material introduced in reference 6

KEY: 1 - standard linearity figure 2 - width of frequency band 3 - actual curve  
4 - theoretical curve 5 - start 6 - end

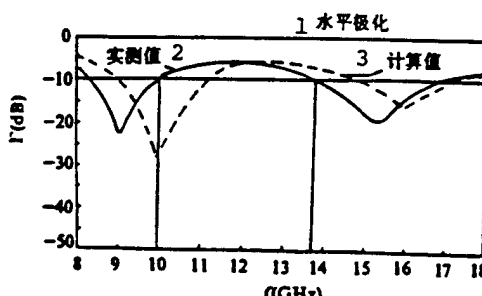


Fig. 4. Absorption performance curve of thin structural radar-absorbent material presented in reference 10

KEY: 1 - horizontal polarization 2 - measured value 3 - calculated value

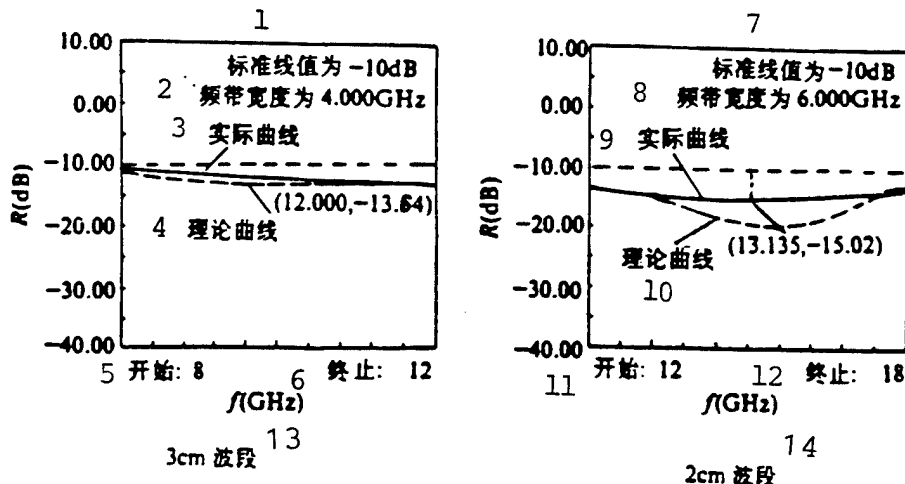


Fig. 5. Absorption performance curve of thin structural radar-absorbent material designed in this paper

KEY: 1 - standard linearity figure 2 - width of frequency band 3 - actual curve 4 - theoretical curve 5 - start 6 - end 7 - standard linearity figure 8 - width of frequency band 9 - actual curve 10 - theoretical curve 11 - start 12 - end 13 - waveband 14 - waveband

### 3.2. Design Study of Hybrid Structural Radar-absorbent Material

There are three actual requirements in designing broadband absorption structures, namely: a. incident radar waves must penetrate the material instead of being reflected directly from the surface of the material; b. an energy-absorbing mechanism must be provided so that the radar waves that penetrate the material can be totally lost; and c. the frequency band for radar wave incidence and loss must be broadened. To satisfy the foregoing mutually contradictory requirements, the following two approaches are generally adopted: one involves using the multilayer structure design method, while the other applies material with higher intrinsic impedance values. Either of them can be chosen depending on the specific type of material.

Nonetheless, further studies show that there is still a large gap between free-space surface impedance and that of the

thin structural radar-absorbent material. In addition, the gradual impedance structure can improve impedance matching between the material and free space but cannot totally eliminate the reflectivity of electromagnetic waves on the front surface due to the material. Also, absorbents available now are not able to ensure a better absorption performance of the thin structural radar-absorbent material. Under such a scenario, material with higher intrinsic impedance proves to be the best choice for the broadband absorption design. It is inevitable, however, that the material with higher impedance can be used only at the cost of increasing the thickness of the material. This is because the present material with higher impedance can only improve impedance matching but cannot feature loss absorption.

Based on the respective unique characteristics of the thin and sandwich structural radar-absorbent materials, a hybrid five-layer structural radar-absorbent material was designed using material with a higher impedance. With high losses in it per se, this material can not only effectively absorb the incident electromagnetic wave energy, but also ensure satisfactory free-space impedance matching (the equivalent impedance of the material is close to 1), resulting in a better broadband absorption performance. Compared with the thin structural radar-absorbent material, this material not only retains a better mechanical performance, but also ensures a lower density of material ( $d=1.5$ ), which is vitally important in reducing the weight of structural members. Fig. 6 shows typical absorption performance curves of the material.

#### 4. Conclusions

(1) The design of broadband structural radar-absorbent material has developed into a macroscopic and fully automatic design and analysis technique instead of a microscopic

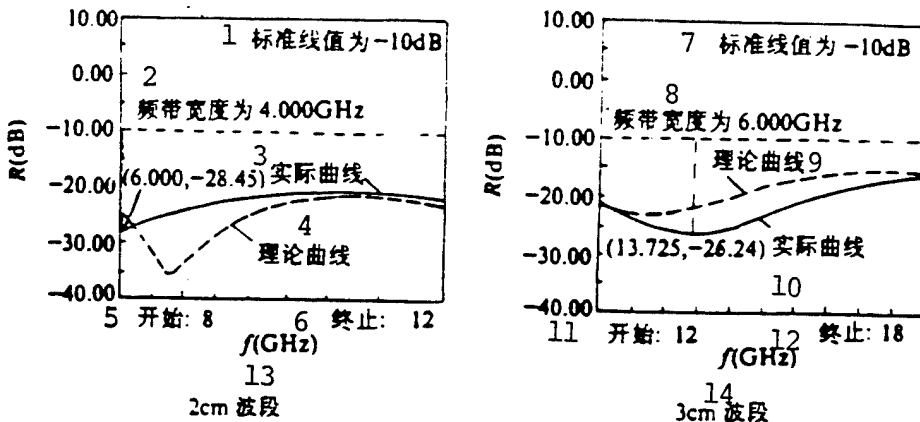


Fig. 6. Absorption performance curves of hybrid structural radar-absorbent material

KEY: 1 - standard linearity figure 2 - width of frequency band 3 - actual curve 4 - theoretical curve 5 - start 6 - end 7 - standard linearity figure 8 - width of frequency band 9 - theoretical curve 10 - actual curve 11 - start 12 - end 13 - waveband 14 - waveband

and manual one. The agreement between our design and the test results suggests that this technique can provide reliable and effective theoretical guidance to the technological study of broadband structural radar-absorbent material.

(2) The thin structural radar-absorbent material designed in this paper with the actual parameter method features a broadband absorption performance. This material, compared with other materials of the same category, shows a remarkable improvement in reflectivity and width of absorption frequency as well as a gradual impedance structure.

(3) The hybrid structural radar-absorbent material designed in this paper using material of higher impedance features a even more satisfactory broadband absorption character and still retains the excellent mechanical functions of the thin structural

radar-absorbent material. This material has a discontinuous impedance structure.

#### REFERENCES

1. Hua Baojia et al., "Research of applications of carbon fiber in structural stealth material," Astronautical Material Technology, 1994(1).
2. Gao Zhengping, "Computer-assisted design of absorbent material with a honeycomb structure," Astronautical Material Technology, 1989(4): 1989(5).
3. Bradshaw, P. S., "Signature management and structural materials," Materials Processing Move into 90'. Proceedings of the 10th International European Chapter Conference of SAMPE. Birmingham, England. 1989.
4. Li Xinhua, "Tentative analysis of development of radar-absorbent materials at home and abroad," Science and Technology Reports, 1989.
5. Wang Xiangyuan et al., "Computer-assisted design of coating radar-absorbent material," Nanjing University Journal (Natural Sciences Edition), 1988(4).
6. Xiao Gaozhi, "Design Study of electrical structure of thin structural radar-absorbent material," Astronautical Material Technology, 1992(3).
7. Perini, Jose, "Design radar absorbing materials (RAM) for wide range of angles of incidence,". International Symposium of EM Compatibility, 1991.
8. Leder, P. G., "An introduction to radar-absorbent materials (RAM)," AD-A169895.
9. Knott, E. F., Radar Cross-section: Its Prediction, Measurement and Reduction, Artech House. Norwood, MA, 1985.
10. Shi Junfang, "Applications of structural radar-absorbent material," Science and Technology Reports, 1992.

#### INDIA IS PLANNING TO CONSTRUCT A SECOND LAUNCH PLATFORM

The Indian government approved a program to construct a second launch platform at the Slihligude Aerospace Launch Center

in the south. The costs of this project are included in the 1995-1996 national space budget. According to this budget scheme, India will carry out three more test launches of a polar-orbiting satellite launch vehicle (PSLV). To date, two test launches have been made of this rocket. On September 20, 1993, the PSLV-D1 failed to send the IRS-1E satellite into the solar geostationary orbit during its first test flight. On October 15, 1994, the second test flight of PSLV-D2 was successful. The first flight of the three planned tests is scheduled later this year.

Also, India increased its budget on the development of geostationary satellite launch vehicles (GSLV). In the new fiscal year budget, \$1.66 million (1.4 billion rupies) will be allocated to the GSLV, bringing its development funding total to as much as 9.8 billion rupies. The first launch of this rocket is scheduled in 1997. India hopes that this rocket will send a 1500-2500kg satellite into a synchronous transfer orbit. In 1993, the United States demanded that Russia stop transferring cryogenic engine technology to India for the reason that the transfer would facilitate the development of ballistic missiles in India. This affected India's development of the GSLV. When Russia stopped the transfer of cryogenic engine technology, India had to increase spending on its own development of engines. In Fiscal Year 1995-1996, the planned engine development funding is 8.91 million rupies, bringing the total increase in the funding of engine development to 3.5 billion rupies.

In addition, in the 1995-1996 budget, a certain amount of spending is allocated to the development of a novel marine remote sensing satellite.

BPSK CARRIER AND BIT SYNCHRONIZATION TECHNOLOGY  
IN PRESENCE OF DYNAMIC DOPPLER

Sun Dongzhi

Beijing Research Institute of Telemetry

**ABSTRACT:** A BPSK carrier and bit synchronization technology in the presence of dynamic doppler is presented in this paper. On the basis of fairly simple digital hardware equipment, the technology is implemented by combining carrier synchronization and bit synchronization flexibly through a programmable digital signal processing software.

**KEY WORDS:** bit synchronization, tracking, digital demodulation, dynamic control.

## 1. Introduction

In aerospace instrumentation systems, measurement and control signals often contain a larger doppler frequency difference and frequency change rate due to the fast-flying instrumentation targets. Especially when data modulation is low, the signal-noise ratio is also low. Therefore, at a low signal-noise ratio, it would be difficult to quickly acquire a larger doppler difference and to track the doppler frequency change rate.

Carrier synchronization and bit synchronization programs very strongly affect the performance of coherent detection. There are a large number of carrier synchronization (including acquisition and tracking) and bit synchronization technologies and corresponding approaches in realizing these technologies. In older references and equipment development[1-4], these two synchronization technologies were occasionally discussed and designed separately. Specifically, carrier synchronization technology was discussed under the premise that bit synchronization had already been realized, while various bit synchronization technologies were analyzed either on the basis of carrier synchronization or by extracting bit synchronization signals from input signals with the help of complex circuits. All these will, particularly in a highly dynamic environment, lead to even greater complexity of circuits so that their performance will be greatly restricted.

To avoid the complexity of equipment structure, this paper, taking advantage of the achievements made in the rapid development of digital circuits, introduces a carrier synchronization and bit synchronization technology in the presence of dynamic doppler. Through a fairly simple digital hardware structure, this technology is mainly used to perform baseband programmable digital processing of doppler signals using a TMS320C25 high-speed digital signal processor. In other words, instead of the hardware method formerly applied in engineering, this technology is realized through software processing[7]. In this case, it can not only improve system performance, but can also increase the reliability of equipment and reduce the debugging load.

Taking BPSK signals as an example, this paper systematically introduces the design concept and fundamental principles of this technology in terms of demodulation.

## 2. Format of Input Signals and Hardware Structure of Demodulator

The dynamic doppler BPSK intermediate-frequency signals (after lower frequency conversion) introduced in this paper have the following specifications:

- a. Carrier center frequency:  $f_{IF}=18.5\text{MHz}$
- b. Data code rate:  $f_b=10\text{kpbs}$
- c. Range of carrier doppler frequency:  $f_d=-39\sim39\text{kHz}$
- d. Change rate of carrier frequency:  $f_d' \leq 2\text{kHz/s}$ .

To realize baseband digital signal processing, this signal is further subjected to lower-frequency conversion, forming two cross routes I and Q, which, after digital sampling, are sent to digital demodulator as shown in Fig. 1.

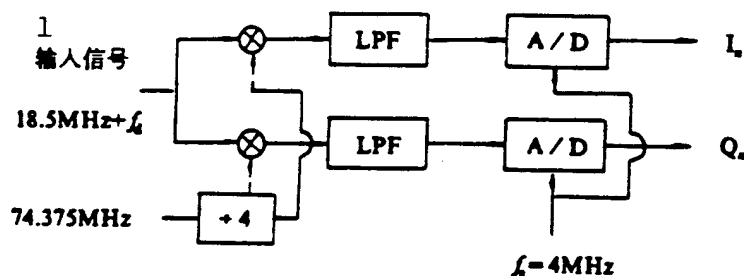


Fig. 1. Baseband conversion of input signal  
KEY: 1 - input signal

Fig. 1 shows that the center frequency of BPSK signal output into the digital demodulator is:

The hardware structure of digital demodulator is shown in Fig. 2. The carrier correlator in Fig. 2 is a complex multiplier, which is used, in the form of an EPROM look-up, to achieve digital correlation of input signal ( $f_c=93.75\text{kHz}$ ) and the estimated carrier frequency. The frequency and phase of the input carrier signal are tracked through adjusting the output frequency of the carrier NCO. The NCO code is employed to

control the accumulation length of digital accumulator and accomplish bit synchronization tracking through changing the output frequency of the NCO code.

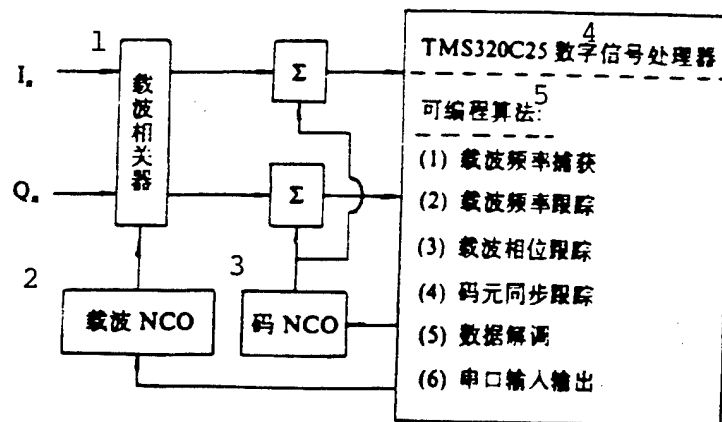


Fig. 2. Hardware structure of digital demodulator  
 KEY: 1 - carrier correlator 2 - carrier 3 - code NCO  
 4 - TMS320C25 digital signal processor  
 5 - programmable algorithm  
 (1) Carrier frequency acquisition (2) Carrier frequency tracking (3) Carrier phase tracking (4) Bit synchronization tracking (5) Data demodulation (6) Series entrance input and output

### 3. Carrier Frequency Acquisition

There are many methods for carrier frequency acquisition. It is well known that the maximum likelihood estimation (MLE)[4] of unchanged but unknown sinusoidal wave frequency is actually equivalent to the discrete Fourier transform (DFT) of the received discrete data. It is a good method when the frequency is relatively stable. However, when the frequency of the input signal varies strongly with time and there is fast data modulation, this method together with the DFT-based automatic frequency tracking loop (ODAFC)[9] is even more difficult to implement.

As for the extended Kalman filtration method (EKF)[9,10,13], the adaptive least-squares method (ALS)[11,12], and the direct

decision combined phase estimation method[8], although they can rapidly discriminate and estimate the parameters of highly dynamic signals, such as phase, frequency, and frequency change rate, they are based on the assumption that bit clocking is known and that data modulation has been eliminated as described in related references. In addition, these methods involve complex calculations, and the related hardware circuits are difficult to implement. To remedy this situation, here we introduce another two methods.

The first method is to divide the range of carrier doppler frequency into several frequency intervals. The frequency interval  $\Delta f$  must ensure that after carrier frequency is acquired, the residual doppler frequency difference will not affect the operation of the bit synchronization loop and is generally designed as approximately  $\Delta f = f_b/20$ . Then these frequency intervals are searched in order, and the signal amplitudes are compared after correlative accumulation. The maximum amplitude is taken as the rough estimate of the carrier frequency. Thus, carrier frequency acquisition can be considered to be accomplished.

When the carrier doppler frequency has an extremely wide range and frequency interval  $\Delta f$  is required to be small, carrier frequency acquisition takes a longer time. To speed up carrier frequency acquisition when bit synchronization has not been established, cross product frequency tracking loop (CPAFC)[10] can be used to discriminate the polarity of carrier doppler frequency, and rapidly approach the carrier frequency of input signal in the step-by-step mode. The second carrier frequency acquisition method can be derived from the angle of time continuity as follows.

The signal model shown in Fig. 3 can be obtained from Fig. 2.

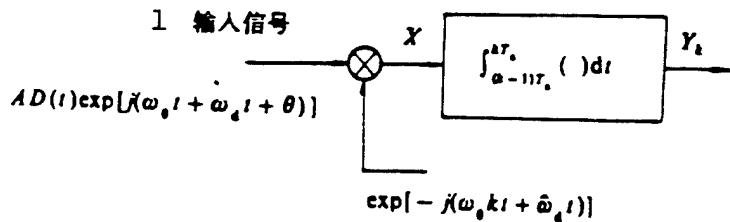


Fig. 3. Input signal model of digital demodulator  
KEY: 1 - input signal

In Fig. 3, A is amplitude of input signal,  $\hat{\omega}_d$  is the estimated value of  $\hat{\omega}_d = 2\pi f_d$ ;  $T_a$  is integration time (accumulative length). The bit width  $T_b$  is required to be an integral multiple of  $T_a$ , i.e.,  $L \cdot T_a \cdot L > 1$ .

After correlative operations of input signal and carrier NCO output signal, the following can be derived:

$$X(t) = AD(t)\exp[j(\omega_{dc}t - \theta)] \quad (1)$$

where  $\omega_{dc} = \omega_d - \hat{\omega}_d$

Following integral sampling, the k-th sampled data value can be obtained as  $Y_k = \int_{n-T_a}^{nT_a} X(t)dt = A \int_{n-T_a}^{nT_a} D(t)\exp[j(\omega_{dc}t - \theta)]dt$  (2)

It might be as well to assume that bit clocking takes place in the k-th integral sampling interval with two adjacent bit symbols D0 and D1 as shown in Fig. 4.

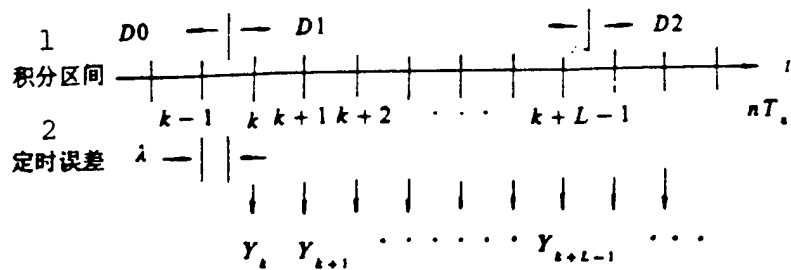


Fig. 4. Integral sampling ( $0 < \lambda < 1$ )

KEY: 1 - integration interval  
2 - clocking error

When these sampled data  $Y_k, Y_{k+1}, \dots$  are treated with  $Z_k = Y_{k+1} Y_k^*$ , the L values of bit length can be derived as

$$\begin{aligned}
 Z_i &= Y_{i+1} Y_i^* = A \cdot D1 \int_{iT_s}^{(i+1)T_s} \exp[j(\omega_{dc} t + \theta)] dt \\
 &\times \left\{ A(D0 - D1) \int_{(i-1)T_s}^{(i-1+1)T_s} \exp[-j(\omega_{dc} t + \theta)] dt + A \cdot D1 \int_{(i-1)T_s}^{iT_s} \exp[-j(\omega_{dc} t + \theta)] dt \right\} \\
 &= \frac{4A^2 \cdot (D0D1 - 1) \cdot \sin(\omega_{dc} T_s / 2) \cdot \sin(\omega_{dc} \lambda T_s / 2)}{\omega_{dc}^2} \exp[j(3 - \lambda) \omega_{dc} T_s / 2] \\
 &+ \frac{4A^2 \cdot \sin^2(\omega_{dc} T_s / 2)}{\omega_{dc}^2} \exp[j(\omega_{dc} T_s)]
 \end{aligned} \tag{3}$$

$$Z_{i+1} = Y_{i+1+1} Y_{i+1}^* = \frac{4A^2 \cdot \sin^2(\omega_{dc} T_s / 2)}{\omega_{dc}^2} \exp[j(\omega_{dc} T_s)] \tag{4}$$

$i = 1, 2, \dots, L-2$

$$\begin{aligned}
Z_{k+L-1} &= Y_{k+1} Y_{k+L-1}^* = A + D1 \int_{k+L-1}^{k+L-1} \exp[-j(\omega_{dc} t - \theta)] dt \\
&\times \left\{ (A(D2 - D1)) \int_{k+L-1}^{k+L-1} \exp[j(\omega_{dc} t - \theta)] dt + A + D1 \int_{k+L-1}^{k+L-1} \exp[j(\omega_{dc} t - \theta)] dt \right\} \\
&= \frac{4A^2 \cdot (D2D1 - 1) \cdot \sin(\omega_{dc} T_a / 2) \cdot \sin(\omega_{dc} (1 - \lambda) T_a / 2)}{\omega_{dc}^2} \exp[j(2 + \lambda) \omega_{dc} T_a / 2] \\
&+ \frac{4A^2 \cdot \sin^2(\omega_{dc} T_a / 2)}{\omega_{dc}^2} \exp[j(\omega_{dc} T_a)]
\end{aligned} \tag{5}$$

The above equations (3)-(5) show that when  $|\omega_{dc} T_a| < \pi$ , the imaginary part  $\text{Im}(Z_{k+1})$ ,  $i=1, 2, \dots, L-2$  can be selected for  $Z_{k+1}$ , which can reflect the polarity change of carrier doppler frequency. For instance, for the integral sampling frequency  $f_a = 1/T_a = 89\text{kHz}$ , the polarity of  $\pm 39\text{kHz}$  carrier doppler frequency can be discriminated; at this moment,  $L = f_a/f_b = 8$ .

Thus, if  $L$  values of  $Z_{k+1}$ ,  $i=0, 1, \dots, L-1$  of bit length are treated with the following formula, the polarity of frequency discrimination  $e_f$  can be calculated as

$$e_f = \sum_i^L \text{SGN}[\text{Im}(Z_{k+1})] = \text{SGN}[\omega_{dc} T_a] \cdot A_f \tag{6}$$

where  $\text{SGN}[\cdot]$  is symbolization, while  $A_f$  can be expressed in the following formulas: \* - or

$$A_f = \begin{cases} L \cdot D0 = D1 = D2 & * \\ L - 1, D0 \neq D1, D1 = D2 \text{ 或 } D0 = D1, D1 \neq D2 \\ L - 2, D0 = D2, D1 \neq D2 \end{cases}$$

Thus, the second method for initial acquisition of carrier frequency is derived.

The second method is applied in the examples illustrated in

this paper. Fig. 5 shows the realization of initial acquisition of carrier frequency. The integral sampling frequency is designed as 80kHz, and the carrier frequency of input signal can be searched through step-by-step frequency adjustment at the step  $\Delta f=500\text{Hz}$ .

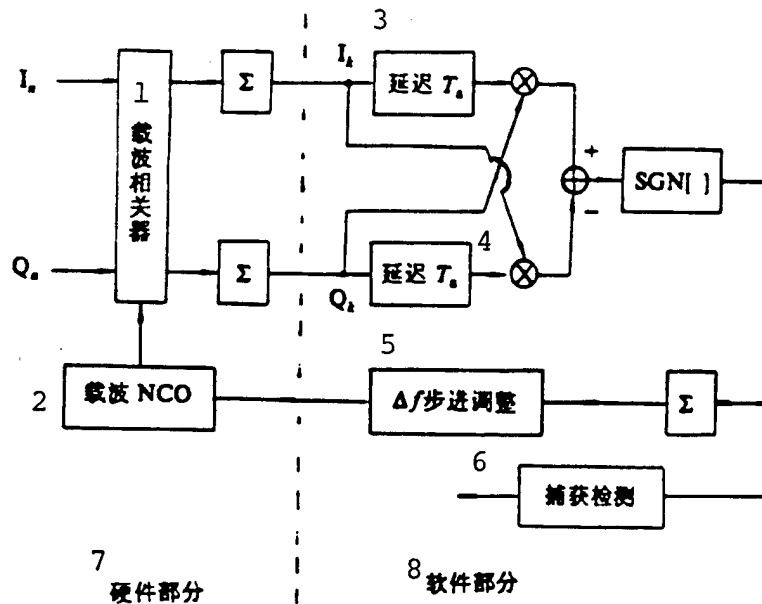


Fig. 5. Initial acquisition of carrier frequency  
 KEY: 1 - carrier correlator 2 - carrier  
 3 - delay 4 - delay 5 - step-by-step  
 adjustment 6 - acquisition detection  
 7 - hardware 8 - software

Since the carrier NCO rapidly approaches the carrier frequency of the input signal at the step  $\Delta f=500\text{Hz}$ , when the carrier frequency has been acquired, the difference between the two frequencies is less than  $\Delta f$ . The frequency discrimination error polarity of the carrier frequency acquisition loop changes alternatively, which allows the detection of the carrier frequency acquisition.

#### 4. Carrier Frequency Tracking

Once carrier frequency acquisition is achieved, the frequency difference between the carrier NCO and input signal is

smaller than  $\Delta f$ . The next step is to establish bit synchronization. The bit synchronization loop described in the following section will show that in the process of establishing bit synchronization, the input signal carries a certain frequency change rate (acceleration) due to the high-speed flight of the measurement and control target. For normal operation of the bit synchronization loop and decrease the effect of carrier doppler on the loop route, carrier frequency acquisition has to be transformed to the frequency tracking mode at the same time when bit synchronization is being established. The frequency tracking loop adopts the route as shown in Fig. 6. To ensure that the software has a sufficient time to accomplish bit synchronization and carrier frequency tracking, the integral sampling frequency has to be decreased from 80kHz to 30kHz (three times the bit velocity) in consideration of the early and late integration bit synchronization loop.

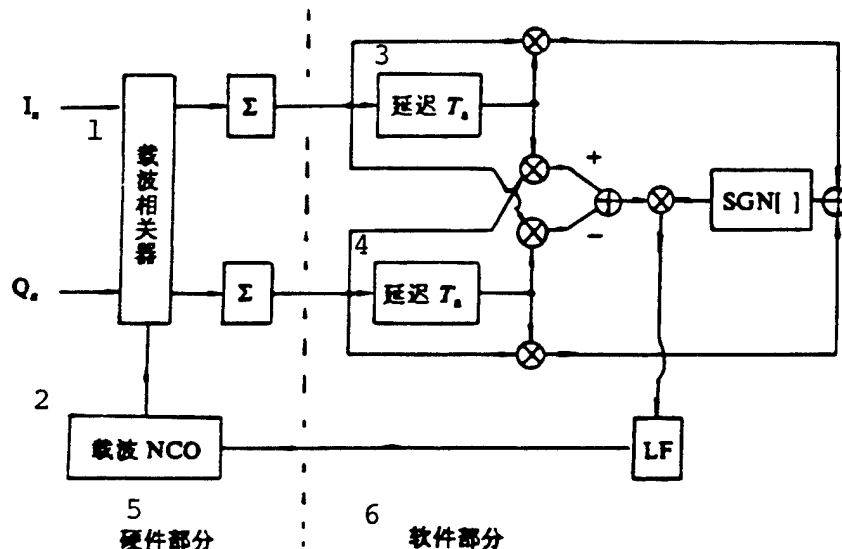


Fig. 6. Carrier frequency tracking loop  
 KEY: 1 - carrier correlator 2 - carrier  
 3 - delay 4 - delay 5 - hardware  
 6 - software

Let us briefly analyze the frequency discrimination characteristics of the carrier frequency tracking loop during the

time when the integral sampling frequency has decreased to 30kHz and bit synchronization has yet to be established. Still, we assume that data transformation takes place in the time interval  $(t_{k-1}, t_k)$  as shown in Fig. 4. Since the integral sampling frequency  $T_a = 30\text{kHz} = 3T_b$ , i.e.,  $L=3$ , our discussion is limited to the four adjacent integral sampled values.

In the carrier frequency tracking loop,  $\omega_{de}T_a \ll 1$  and  $0 < \lambda < 1$ . Hence, Eqs. (3)-(5) can be simplified as:

$$Z_d = A^2 T_s^2 [1 + (D0D1 - 1)\lambda] \quad (7)$$

$$Z_u = A^2 T_s^2 \cdot \omega_{de} T_s [1 + (D0D1 - 1)\lambda(3 - \lambda)/2] \quad (8)$$

$$Z_{e(k-1)} = A^2 T_s^2 \quad (9)$$

$$Z_{e(k+1)} = A^2 T_s^2 \cdot \omega_{de} T_s \quad (10)$$

$$Z_{e(k+2)} = A^2 T_s^2 [1 + (D1D2 - 1)(1 - \lambda)] \quad (11)$$

$$Z_{e(k+3)} = A^2 T_s^2 \cdot \omega_{de} T_s [1 + (D1D2 - 1)(1 - \lambda)(2 + \lambda)/2] \quad (12)$$

For bit length, the frequency discrimination error  $Z_{el}$  is

$$\begin{aligned} Z_{el} &= Z_u \cdot \text{SGN}[Z_d] + Z_{e(k+1)} \cdot \text{SGN}[Z_{e(k+2)}] + Z_{e(k+3)} \cdot \text{SGN}[Z_{e(k+2)}] \\ &= A^2 T_s^2 \cdot \omega_{de} T_s \{1 + [1 + (D0D1 - 1)\lambda(3 - \lambda)/2] \cdot \text{SGN}[1 + (D0D1 - 1)\lambda] \\ &\quad + [1 + (D1D2 - 1)(1 - \lambda)(2 + \lambda)/2] \cdot \text{SGN}[1 + (D1D2 - 1)(1 - \lambda)]\} \\ &= A^2 T_s^2 \cdot \omega_{de} T_s \cdot G_{el} \end{aligned} \quad (13)$$

Obviously, if bit data transformation does not happen, i.e.,  $D0=D1=D2$ ,

$$G_{el} = 3 \quad (14)$$

When bit data transformation happens:

a. When  $D0D1=-1, D1D2=1$ ,

$$G_{\text{el}} = \begin{cases} 3(1-\lambda) + \lambda^2, & 0 \leq \lambda < 1/2 \\ 2, & \lambda = 1/2 \\ 1 + \lambda(3 - \lambda), & 1/2 < \lambda \leq 1 \end{cases} \quad (15)$$

b. When  $D0D1=-1, D1D2=-1$ ,

$$G_{\text{el}} = 1 + 2(1 - 2\lambda) \quad (16)$$

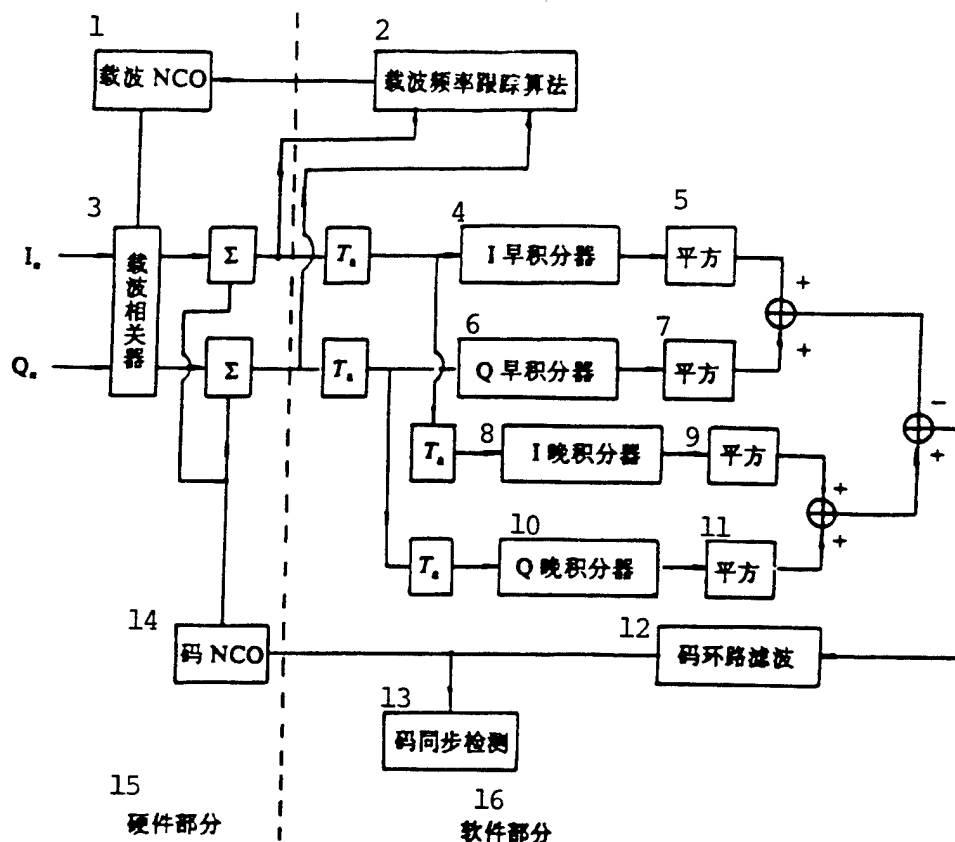


Fig. 7. Improved early and late integration bit synchronization tracking loop

KEY:  
 1 - carrier 2 - carrier frequency tracking algorithm  
 3 - carrier correlator 4 - early integrator 5 - square  
 6 - early integrator 7 - square 8 - late integrator  
 9 - square 10 - late integrator 11 - square 12 - bit  
 loop route filtration 13 - bit synchronization detection  
 14 - bit 15 - hardware 16 - software

Eqs. (13)-(16) indicate that the frequency discrimination error  $Z_{el}$  of the carrier frequency tracking loop route as shown in Fig. 6 can reflect the variation of carrier frequency.

## 5. Bit Synchronization

The foregoing carrier frequency acquisition and tracking can greatly reduce the frequency difference between carrier NCO and input signal, yet they cannot solve the problem of phase agreement between the two. It is for this reason that various bit synchronization loops based on conventional one-route data flow turn out to be ineffective, such as the absolute value early and late integration bit synchronization loop (AVTS), and data transformation tracking loop (DTTL). To compensate for this situation, this paper presents a software-based early and late integration bit synchronization loop as shown in Fig. 7. It is designed to eliminate, through a square adding method, the effect of disagreement in carrier phase tracking on the bit synchronization loop. The precondition of normal operation of the bit loop shown in Fig. 7 is that the frequency of input composite signals does not change very much. But this is not the case here, because the carrier frequency acquisition loop as well as the carrier frequency tracking loop that operates at the same time as the bit synchronization loop can already satisfy this condition.

When bit synchronization detection decides that the bit has been synchronized, to demodulate data, the carrier frequency tracking loop converts to carrier phase tracking mode so as to track the carrier frequency and phase. In the meantime, the bit synchronization loop continues tracking the bit phase.

## 6. Carrier Phase Tracking and Data Demodulation

The carrier phase tracking loop adopts the binary DPLL mode[1-4,7] as shown in Fig. 8.

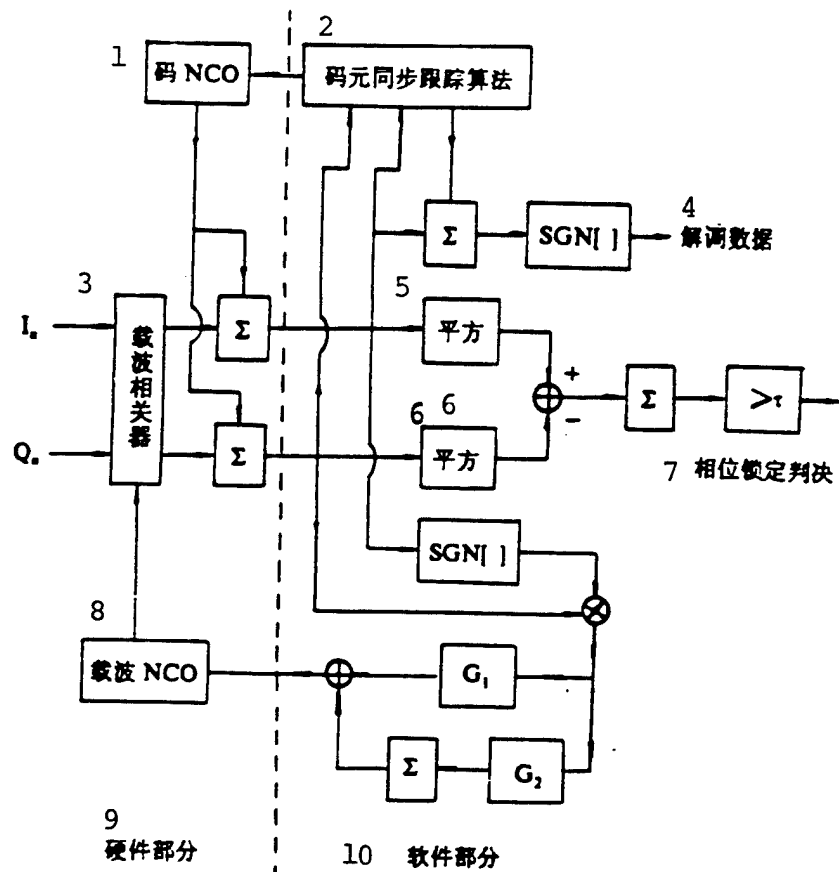


Fig. 8. Carrier phase tracking loop and data demodulation

KEY: 1 - bit NCO 2 - bit synchronization tracking algorithm 3 - carrier correlator 4 - demodulated data 5 - square 6 - square 7 - phase locking decision 8 - carrier 9 - hardware 10 - software

When the carrier phase locking decides the phase locking[4], data bit demodulation can start.

The early and late integration bit synchronization tracking loop as shown in Fig. 7 is suitable for input data with a higher signal-noise ratio. If the effect of the noise performance of

this bit synchronization tracking loop on data demodulation is to be further decreased, it is possible to convert, based on need, the bit synchronization tracking loop as shown in Fig. 7 to the one-route data flow-based absolute value early and late integration bit synchronization loop (AVTS) mode [2,5] after the carrier phase is locked. This will not be detailed here.

## 7. Conclusions

The foregoing BPSK carrier and bit synchronization technology in the presence of dynamic doppler features the simple structure of digital hardware, the novel and flexible programmable software algorithm, and the extremely convenient debugging and modification. The technical simulation confirmed that this technology is reasonable and feasible, and its performance test result is only 1dB different from the theoretical value.

**Acknowledgements:** Our sincere thanks go to Zhen Tienan and Wang Xinyu for their assistance in simulation tests and equipment debugging.

This paper was received in September, 1994.

## REFERENCES

- 1 Franks L E. Carrier and bit synchronization in data communication—tutorial review. *IEEE transaction on Commun.*, 1980, COM-28(8).
- 2 Lindsay W C, Simon M K. *Telecommunication system engineering*. Prentice-Hall, Englewood Cliffs, New Jersey, 1973.
- 3 Lindsey W C, et al. A survey of digital phase-locked loops. *Proc., IEEE*, 1981, 69(4).
- 4 Mileant A, Hinedi S. Lock detection in costas loops. *IEEE transaction on Commun.*, 1992, 40(3).
- 5 Payzin A E. Analysis of a digital bit synchronizer. *IEEE transaction on Commun.*, 1983, COM-31(3).
- 6 Hinedi S, Stateman J I. Digital accumulators in phase and frequency tracking loops. *IEEE transaction on AES* 1990, Jan. 169—180
- 7 Aguirre S, Hurd W. Design and performance of sampled data loops for subcarrier and carrier tracking. *TDA progress report 42-79*, JPL pasadena, CA, Nov.15, 1984; 81—95
- 8 Fitz M P, Lindsey W C. Decision-directed burst-mode carrier synchronization techniques. *IEEE transaction on Commun.*, 1992, 40(10).
- 9 Aguirre S, Hinedi S. Two novel automatic frequency tracking loops. *IEEE transaction on AES*, 1989, 25(5).
- 10 Vilnrotter V A, Hinedi S, Kumar R. Frequency estimation techniques for high dynamic trajectories. *IEEE transaction on AES*, 1989, 25(4).
- 11 Kumar R. Fast frequency acquisition via adaptive least squares algorithm. *ITC '86*; 91—101
- 12 Kumar R. Differential sampling for fast frequency acquisition via adaptive extended least squares algorithm. *ITC '87*; 191—201
- 13 Kumar R. A novel multistage estimation of the signal parameters of a possibly data-modulated sinusoid under very high dynamics. *JPL 89-11*, Jet propulsion laboratory, California Institute of Technology, Pasadena, CA, 1989.5
- 14 Kam P Y. Maximum likelihood carrier phase recovery for linear suppressed-carrier digital data modulations. *IEEE transaction on Commun.*, Vol.COM-34, 1986.6

NEWS BRIEF: PROTON M ROCKET WILL BE  
BROUGHT INTO COMMERCIAL LAUNCH MARKET

Russia and Germany will team up to bring the Proton M rocket into the commercial launch market in an attempt to attract small- and medium-scale satellite users. The launch activities will kick off in 1997 starting from the Baikonur Cosmodrome in Kazakhstan.

The Proton M rocket is designed as a three-stage rocket, which, so far, has been launched three times. In fact, it is a modified version of the SS-19 nuclear missile developed in the former Soviet Union and can be used to launch satellites weighing 800-1500kg. After entering the market, this rocket is expected to launch three satellites a year and become profitable by century's end.

The Proton M rocket was developed at the Russian Khrunichev National Research and Production Space Center. This center has joined hands with the Daimler-Mercedes Space Orbit System Branch Cooperation in Bremen, Germany, to promote their rockets throughout the world and is planning to set up a company called Eurokot in Bremen in the spring of 1995. This strategy was worked out based on the approach made by the Khrunichev Center to set up a joint venture with the American Lockheed Corporation and the Russian Energia Corporation, the manufacturers of the four-

stage rocket Proton, in an effort to enter their rocket Proton in global markets. This company is called Lockheed-Khrunichev-Energia International (LKEI), with headquarters in San Jose, California, United States.

The Proton M rocket is exclusively manufactured by Khrunichev, with its first and second stages being a new version of the SS-19, and its third stage being a newly-designed product, called Breeze, which can be restarted. It is reported that the upper rocket stage is designed mainly for launching multiple-reentry-warhead missiles, or as a upper stage replacing the new one developed by Energia Company for the Proton rocket. Breeze, the third-stage rocket has undergone through three tests at the Baikonur Cosmodrome. On December 26, 1994, the first non-professional radio satellite was carried to an orbit 2000km in height with this third-stage rocket. Among other activities, Khrunichev is planning to develop a new fairing for the Proton M rocket.

The Daimler-Mercedes Company embraces a vision that the launches of small-scale scientific and earth observation satellites will find growing markets. Many satellites of this kind will be sent into low polar earth orbits. In this way, the rocket launch site can be moved from the present-day Baikonur Cosmodrome to the local Plesetsk Cosmodrome in Russia. The second market, on which the two companies keep a close eye, is the future market of global wireless phone satellite networks.

Khrunichev is a stockholder connected with the Iridium Satellite Telecommunication Networks, consisting of 66 satellites. Daimler-Mercedes has already purchased the stock of the Globalstar satellite network, which consists of 48 operating satellites and eight standby satellites. Both the iridium satellite network and the satellites associated with Globestar are near-earth orbit satellites.

As Werner Inden, the assistant manager at the Daimler-Mercedes Company, pointed out that they formerly planned to collaborate with some companies in Europe in developing small launch vehicles, but this plan ended up without any result. However, Klaus Iserland, formerly director at the International Affairs Department of ArianeSpace, Inc., and currently a consultant at the Daimler-Mercedes Company, said that he is fully confident in his company's ability to overcome various difficulties and ultimately entering Proton M into the commercial launch market. (This report was filed by Xi Yin.)

#### AN AMERICAN RESEARCH GROUP EXPRESSING AMERICAN ROCKET TECHNOLOGY IS LAGGING

A research group affiliated with the United States Department of Defense has concluded, based on their comparison of medium- and large-scale launch vehicles between the United States and other countries, that the rocket technology in other countries is more efficient and advanced than that in the United States.

According to research by this research group, since the late seventies, America focused its attention on research of space shuttles and their flights, but many research and development programs in regard with launch vehicle systems became stagnant, and few new launch vehicle systems were developed, while it was during this period that the carrier technology developed by other countries had blossomed. As a U.S. Air Force official suggested, the space industry in the United States is in the leading edge in the aspect of development of small-scale satellite market, whereas it lags behind in the medium-and large-scale satellite launch market. Still, according to this group, assimilating the fundamentals of foreign carrier rocket systems is vitally important to the American carrier system.

Despite many advantages in foreign launch systems as indicated, this research group has yet to come up with any suggestion of launching American military loads with foreign rockets.

According to a document issued in August 1994 by the White House on launch policy, no foreign rocket is allowed to launch effective loads associated with the American government. As an official from Air Force claimed, the application of foreign launch system components was restricted for the sake of national security. But the foreign parts manufactured in the United States through transfer of technology was adoptable.

The Lockheed Corporation and two companies in Moscow have been incorporated into a joint venture called Lockheed Khrunichev-Energia International, aiming at joining efforts to promote the commercial launches of the Russian rocket Proton in the global market.

For the research result reached with this group from the Department of Defense, the spokesmen from both the Lockheed Corporation and Martin-Marietta Corporation refused to give any comments. According to a director from ArianeSpace Corporation, this research was too simple, and the estimates made by the group were not convincing enough. Whereas a responsible person from American Institute of Astronautics and Aeronautics gave a positive reaction toward the general idea of the research. But He pointed out that we should not simply take all foreign rockets for granted: some of them are better, some of them are not that advanced. Additionally, he said that foreign rockets generally are more or less modernized, while those made in the United States are a bit out of date; but these rockets have been gradually improved.

The research report made by this group affiliated with Department of Defense is as follows:

Countries such as Japan, China, and the former Soviet Union are all conscious of providing support and funding to the aerospace development programs for the national concern, while the United States lacks such consciousness encouraged by these countries.

Ariane in Europe and H-2 in Japan both have fully adopted modern technologies, while the new technologies applied in the American launch systems are very limited.

The Sky Top from Russia and Ariane-5 rocket systems from Europe are simple, but highly efficient and well automated, with an excellent coordination between the launch platform and rocket structures.

What is more, the production of rocket systems in China, Europe and former Soviet Union is generally fast and highly efficient.

Launch preparations of American's largest rocket Atlas take 198 days, while preparations for Proton rocket launches require only 21 days. (Xi Yin filed this report)

#### AUSTRALIA RESTORES ITS EXPLORATION OF SPACE LAUNCH BUSINESS

The Australian government has asked its Space Program Office to make a proposal on commercial launch services in this country. According to the head of the federal department in charge of the space program, Womera in the south, and Darwin in the north of Australia are expected to be chosen as the launch sites. If so, Womera will be designated to launch polar satellites, while the Darwin in the north can be utilized to launch equator-orbiting

satellites. An administrator in the Australian Space Program Office indicated that they had started to contact some of the potential launch clients, including the American firm Pac-Astro, Inc.

The proposal to launching small satellites into near-earth orbit from Australia was initiated as early as six years ago by two researchers from the Australian Defence and Science Technology Research Organization. It was at that time that these two researchers were aware that with the launching of various near-earth orbit mobile communication satellites, many alternative satellites would be required to be launched. Thus far, setting up launch sites in Australia has been mainly concentrated in Cape York on the northeast coast, which would cost as much as \$760 million. The fundamental part of the proposal supported by the Australian Space Program Office was to utilize Sky Top made by Yuzhnoye, Inc., in Ukraine to launch large geosynchronous communication satellites.

Following a proposal made by the Kennett International Technologies Inc. (KIT) on establishing a remote sensing system, most Australian government officials favored the plan of setting up a launch site for small satellites. The KITcomm system, with a total expenditure of \$15 million, was designed to apply a constellation, which is made up of eight satellites. These satellites were to be fixed in equatorial orbits with a height of 1200km, which can cover areas between 35° N. Lat. and 35° S. Lat., and these satellites will be provided by the American firm Aero-Astro, Inc.

KIT has signed an official contract with Aero-Astro, Inc., on supplying the first four satellites, and the contract for the remaining satellites is to be signed later. This system is expected to be brought into use in early 1997; by that time, the

initial stage will focus on the observation of reservoirs, the routing of enclosure fences and other relevant facilities located in remote pasturages across Australia. As an integral part of the foregoing contract, Pac-Astro, a subsidiary of Aero-Astro, Inc., is to provide KIT with two low-cost PA2 liquid-fueled rockets. Also, according to the manager of Aero-Astro, Inc., they will participate in the operations conducted at the Darwin launch site. Once the remote sensing system proposed by KIT has been put into use in Australia, the observation services will be extended to other countries.

Since the cost of launching the PA2 rocket was only approximately \$6 million, and the cost of the applications small satellites was under \$2 million, this kind of small-scale launch market is likely to be expanded. Hence, KIT hopes to be able to conduct business operations in launching small satellites from Australian launch sites.

According to a five-year space development program proposed by the Australian Space Program Office, the government will soon invest \$30 million on the design and production of two small satellites and related rockets to support the feasibility of designating Australia as a launch site.

The proposals such as the establishment of a remote sensing system by KIT suggested that through the application of small rockets, cost-effective launch operations will become possible in Australia. With the growing demand for small satellites and reduced costs of entering commercial markets (which fell below \$76 million), the environment of commercial satellite launches from Australia has seen some improvements. (Xi Yin filed this report.)

#### FIRST SUCCESSFUL LAUNCHING OF PEGASUS XL ROCKET

The Pegasus XL air-launched rocket designed by American firm Orbital Science, Inc., was successfully launched for the first time on April 3, achieving the mission of carrying this company's first two Orbcomm communication satellites onto a circular orbit 728km in height. The first launch of this remodeled rocket failed owing to the use of a defective aerodynamic model.

An L-1011 Lockheed aircraft carrying this rocket took off from Vandenberg Air Force Base. The rocket flew off the aircraft when the aircraft was 80km west of the California coast and at a height of 12,200m. By the time the third-stage rocket reached the given orbital height, it released the first Orbcomm satellite southward. Then after positioning itself, the rocket released the second one northward. Following its powered flight, the rocket sent the carried small scientific experimental satellite Microlab1 into orbit.

As Orbital Science, Inc., expressed, the launching of Orbcomm satellites will mark a new era of satellite data communications. This company is scheduled to launch a total of 26 satellites of its kind by the end of 1997 for the cost-effective personal communication around the world. The rest of 24 satellites will be launched on a three-each-time basis.

Before being modified, a total of six Pegasus rockets were launched since 1990, of which, four launches were successful, while the other two was partly successful. Thus far, Orbital Sciences, Inc., has signed twelve launching contracts with some clients such as NASA, the Air Force and Ballistic Missile Defense Organization, etc.

Soon after the Pegasus rocket sent a satellite into orbit on April 3, an error occurred in the exit and entrance of the communication sub-system of Orbcomm 2, which caused a reaction failure from the ground station with respect to data transmission

from satellite. On April 15, another error occurred in the Orbcomm1 client communication subsystem, which made it impossible to send data to the clients. (Yu Tian filed this report.)

INKE (HONG KONG), LIMITED

Inke (Hong Kong), Limited, is a high-tech company based in Hong Kong, and it is DEC's first value-added agent in China/Hong Kong/Taiwan. With a broad business scope, including computer system integrity and software development, this company provides overall solutions in fields ranging from the analysis committed to the clients in regard with demand and supply, strategy design, and system installation integrity to after-sales services, which earned it a high popularity in regions such as China/Hong Kong/Taiwan.

In recent years, Inke rapidly developed its business operations in China. To better serve its clients there, Inke has invested \$500,000 in setting up a sole proprietorship in Beijing: Beijing Donghua and Inke Computer, Limited.

With the business philosophy of "the customer is king," Inke always wholeheartedly provides its clients from all walks of life with the best services and has won a excellent creditability in the business circle. Inke focuses its efforts on three major fields, defense, electromechanical engineering, and petrochemistry.

Since the export of ALPHA computers made by the American company DEC to China became possible, Inke, as DEC's first-level agent, signed contracts with dozens of businesses in China, to supply more than 200 (sets of) ALPHA workstations (including microcomputers), with annual business revenues reaching \$15 million, which brought Inke to the leading edge among DEC's 49 agencies.

These clients include a number of research institutes under the Space Industry Headquarter Company, National Defense and Science Committee, Qinghua University CAD Center, Harbin Engineering University, Shenyang Pump Plant, Dalian Crane Factory, Beijing Integrity Circuit Design Center, National Marine Meteorology Forecast Center, Xidan Department Store, Beijing Petrochemical Engineering Company, Luoyang Petrochemical Engineering Company, Shanghai Jinshan Petrochemical Company, Daqing Petrochemical Company, Yanshan Petrochemical Company, Huaneng international Power Company, Henan Xinfei Electric Appliances Group, Tianjing Ordis Elevator Company, Air Force Automation Division, Nanjing Automation Institute, and so on.

With the accomplishments after years of business operations, Inke has not only built up remarkable creditability among the clients, but also accumulated a wealth of experience in the import-export business and DEC system integrity. At the same time, Inke established good business relations with organizations such as the Electromechanical Equipment Import and Export Office affiliated with the State Council, Electromechanical Equipment Import and Export Office under the Ministry of Electronics, National Planning Committee, Economic and Trade Committee, Ministry of Economic and Trade, Customs Office.

Inke always adheres to its set principle of putting service and equipment quality as its first priority, making certain that the products supplied are all bona fide, i.e., the latest original products manufactured by DEC, and there has never been a case in which mixed products were provided solely for the sake of profits.

With respect to any technical concern from clients, DEC bears the responsibility of providing the best technical services through DEC maintenance stations, and ensures hot-line service within 8 hours, and on site service within 48 hours. Inke can

provide an integrity of services as follows:

1. Assisting clients in handling import procedures and applications for import licenses.
2. Providing preferential prices in the exchange of foreign currency.
3. Assisting clients in handling tax exemption procedures.
4. Cooperating with DEC maintenance stations to provide clients with best technical support, including on-site installation and after sale service.
5. Offering the service in foreign and domestic transportation, custom declarations, as well as goods pick-up and direct on-site delivery service.
6. Taking the responsibility of multi-level training for clients both at home and abroad and inviting the clients to go overseas for inspection, handling visa applications for trainees and making arrangements for the reception of visitors. (Xue Xiangdong filed this report.)

#### BRIEF INTRODUCTION TO CHINA HUADI COMPUTER, LIMITED

Registered in the China National Industrial and Commerce Bureau, China Huadi Computer, Limited, is a Sino-US joint venture, invested in jointly by China Space Industry Headquarter Company and the American firm DEC, and approved by the China Ministry of Electronic Industry and China Foreign Economic and Trade Cooperation. Its headquarters is in Beijing.

Since the implementation of reform and open-door policy, China Space Industry Headquarters, as a backbone of China's high-tech industry, has taken full advantage of its cutting-edge technology in the space industry to develop the computer industry as a pillar industry in an attempt to meet the needs of the current high speed development of market economy. What is more, it has made efforts in all aspects to strengthen its cooperation with foreign businesses, support technology transfer in the field

of the development of the space-oriented computer industry, and motivate enormous potential energy from dozen of professional computer and application research institutes in the space industry to vigorously serve the needs of building China's computer and application technology industry.

The DEC in America is one of the largest computer system manufacturers and suppliers in the world, with annual business revenues nearing \$14 billion. It stands at the leading edge across the world in aspects such as the open-environment computer systems, network communications, computer chip technology, software systems and other comprehensive services. Especially in 1992, it developed the Alpha AXP 64-bit reduced instruction computer set system structure and products which, with its high performance, high speed and powerful addressing capability, was listed in the 1992 Guinness Book of World Records.

The Huadi company was established on the basis of a long-term thorough demonstration made by the American firm of DEC and the China Space Industry Headquarters Company. Having been engaging in China business operations for decades, this is the first and only time that the American firm of DEC has invested in setting up a joint venture in China. Undoubtedly, the birth of Huadi has had a significant impact on both sides.

Since it was founded, the Huadi company has displayed its remarkable supremacy in aspects such as profession, technology, management, service and sales indicating by both sides. Collaborating with various professional institutes and universities related to China's space industry, Huadi has extended its business scope to a variety of fields, including the DEC complete series of workstations, sales of service facilities, maintenance services, system integrity, CAD/CAM, development of office automation products, development and promotion of OEM and CSS (Computer Specialist System) products, and so on. At

present, Huadi has successfully accomplished the task of localizing DEC's famous office automation platform products (Link Works) in China, from which, a complete set of office automation network integrity system was developed to provide a set of ideal solutions for the OA system applied in large and medium enterprises, as well as service sectors.

Today, Huadi has hundreds of clients throughout the country covering all kinds of businesses such as governmental electronics, aviation, aerospace, machinery, education, railway, communications, weaponry, transportation, military force, automobiles, utility, banking, etc., and keep close business ties with them. Huadi teams up with all its partners---especially world-class software manufacturers--to provide clients with a integrity of software and hardware services.

Constantly pursuing the idea of perfection and putting customers first is Huadi's utmost business ritual. To achieve this goal, Huadi set up a complete set of customer service system. With its well-trained and experienced marketing, sales and technical support staffs, Huadi, along with various institutes and universities from the space industry and DEC China Corporation, has built up extensive sales, maintenance network stations, and demonstration centers, training centers in major regions all over the China in an effort to provide its clients with a series of services including before-sales training, after-sales installation, maintenance, secondary product development, and system integrity.

Huadi pays close attention to supporting agency business. Thus far, Huadi developed more than 10 agencies located throughout major cities in China. Along the road of Huadi development, the agencies have become Huadi's close partners.

Collaboration-conscious, with a strong sense of

responsibility, fulfillment of customer's requirement, pursuit of perfection and persistence, and dedication in achieving goals are Huadi's fixed principles. Huadi always acts as a friend of costumers and will be happy to provide support to all costumers every step of the way in their business growth. (Zhang Xiang Jun filed this report.)

AMERICAN DEC COMPANY ANNOUNCED ITS SUCCESS  
IN THE DEVELOPMENT OF WORLD'S FASTEST COMPUTER--ALPHA

Seeing an Alpha computer for the first time, Steven Cadner, the president of the American company, AEON System, Inc., could not help exclaiming: " I've been working in the computer business for 20 years, but the birth of the Alpha series computer is the most exciting invention I ever experienced in the last 20 years"

Indeed, the Alpha microprocessor suddenly carries people into the 21st century. Many technologies formerly thought impossible--a global network, multimedia applications, real-time image processing, artificial intelligence and virtual reality, etc., are now just around the corner.

The Alpha microprocessor is the fastest microprocessor in the world.

The Alpha microprocessor is the most advanced chip with a 64-bit reduced instruction set.

The Alpha computer is the fastest, most advanced series computer in the world.

The American firm of DEC Corporation is one of the largest computer manufacturers in the United States, with business revenues reaching \$13.7 billion in Fiscal Year 1994.

As early as in the seventies and eighties, DEC had already been well known for its outstanding PDP, VAX series computers, among which, the VAX computer came to be seen as a priority model among users in China and made phenomenal contributions in the development of China's computer industry.

In the nineties, Robert Parmer, DEC president, foresaw the growing market demand as well as the striking trend of technology development and pointed out: "We should concentrate our efforts in the service, network, software, chips and memory technology". With outlays of 1 \$billion and five years of effort, DEC finally invented the Alpha microprocessor in February 1992. Even at that time, its chip speed had already reached 200 Mhz, which is equivalent to the computing capability of the Cray-1 Supercomputer.

In 1992, this microprocessor was recorded in the Guinness Book of World Records as world's fastest microprocessor.

Today, the top speed of Alpha chips made by DEC has reached 300 Mhz, while the speed of chips produced by most of today's manufacturers stays only at around 100MHz.

Speed is by no means all that the Alpha computer is about. More importantly, it has a 64-bit design. It is well understood that computer relies on the two status, "0" and "1", to represent data and storage address. The larger the number of bits is, the more combinations of "0" and "1" can be constituted and then the larger the storage address that represent data and addressing can be. As a result, its computing and storing capabilities can become stronger. 386 and 486 computers that people always talk about are designed to be 32-bit computers, and the most present-day computers have a 32-bit design, as well. And the addressed memory units account only for  $2^{32}$ , which is equal to 4 billion,

while a computer with 64 bits can have as many as  $2^{64}$  addressable memory units, i.e 4 billion times as many as in 32-bit computers. Obviously the advances of this computer are indisputable.

"Open Environment" is today's hot topic in the computer industry. As far as hardware is concerned, the basic requirement of the "open environment" is the capability of running the software developed by different manufacturers, not only its own software. The Alpha computer can be considered as a multi-functional hardware platform with a real "open environment". It can support and reach today's all-key standards, and it can also provide clients with all options for the operating system, on which users can run some general operating systems such as OpenVMS, Windows NT, and UNIX. In particular, DEC provides the first, and also the only 64-bit UNIX operating system (Digital UNIX) in the world, which allows users to make full use of the strong capability of the 64-bit Alpha computer and this complete open UNIX environment as well.

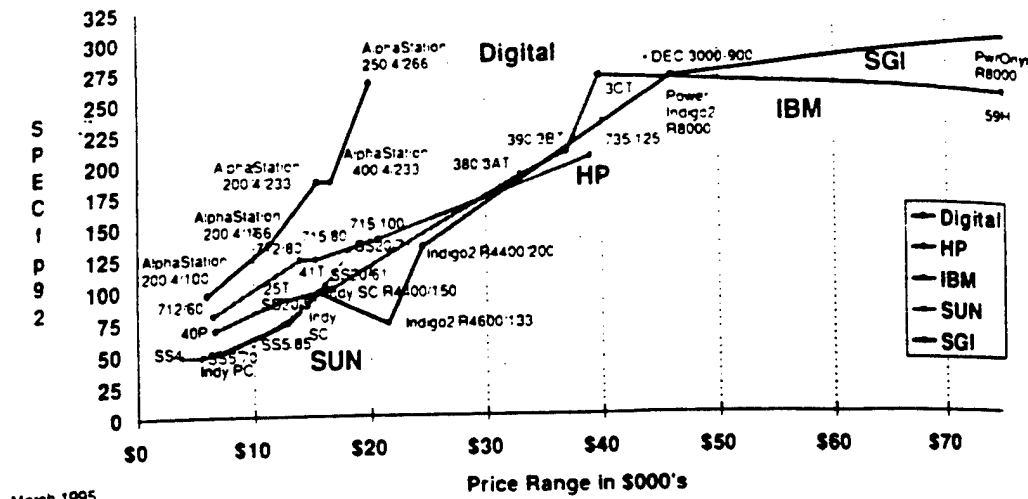
To better serve the client's investment needs, the compatibility of the Alpha system structure was designed based on the last 25 years' experience in designing. As a result, the clients can confidently make their investments in a variety of aspects such as the applications, network, user interfaces, peripheral devices as well as technical training, etc.

If the hardware can be compared to a human body, then the software can be considered as the human mind. As long as the human mind is full of various knowledge, this person can be thought to be proactive. From the above comparison, it can be said that the number of software programs run on the hardware become a key factor in testing whether or not the hardware can perform well. So far, the number of software programs that can be run on the Alpha platform has surpassed 6,400, and the number

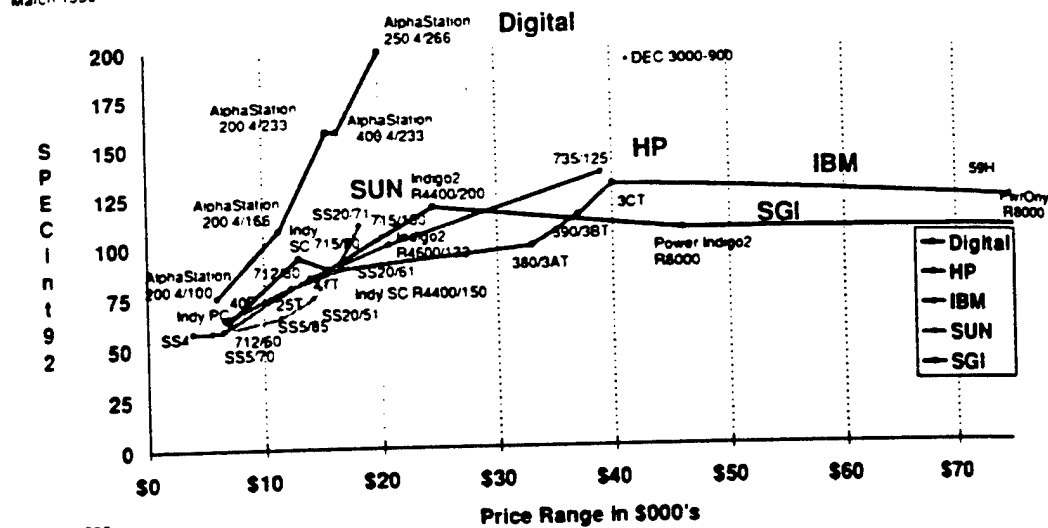
is still growing. This number and speed are amazing, and they make people have a strong confidence toward this cutting edge technology.

Today, Alpha computers are sweeping all over the global markets. Certainly, if we can afford to buy a 386 computer now, why we should bother to pick a 286 computer first, and then buy a 386 computer anyway? Since the application of the first Alpha computer at China Academy of Power Scientific Research Institute in January 1994, the purchase orders received by DEC have been constantly increasing, and this purchase growth has just been unprecedented. Thus, the application of Alpha computer is not only to keep up with latest advanced technology trend, but also, an inevitable tendency of market development. (Wang Lian filed this report.)

Performance/Price Comparison Chart for DEC  
Workstation Products



March 1995



March 1995